3-2023

Concept of Operations of Cislunar Mirror Satellites to Provide Augmented Lighting of Dim Space-Based Objects

Alec E. Cook

CONCEPT OF OPERATIONS OF CISLUNAR MIRROR SATELLITES TO PROVIDE AUGMENTED LIGHTING OF DIM SPACE-BASED OBJECTS

THESIS

Alec E. Cook, Captain, USSF

AFIT-ENY-MS-23-M-264

DEPARTMENT OF THE AIR FORCE
AIR UNIVERSITY

AIR FORCE INSTITUTE OF TECHNOLOGY

Wright-Patterson Air Force Base, Ohio

AFIT-ENY-MS-23-M-264

CONCEPT OF OPERATIONS OF CISLUNAR MIRROR SATELLITES TO PROVIDE AUGMENTED LIGHTING OF DIM SPACE-BASED OBJECTS

THESIS

Presented to the Faculty

Department of Aeronautical and Astronautical Engineering

Graduate School of Engineering and Management

Air Force Institute of Technology

Air University

Air Education and Training Command

in Partial Fulfillment of the Requirements for the

Degree of Master of Science in Astronautical Engineering

Alec E. Cook, B.S.M.E.

Captain, USSF

March 23, 2023

AFIT-ENY-MS-23-M-264

CONCEPT OF OPERATIONS OF CISLUNAR MIRROR SATELLITES TO PROVIDE AUGMENTED LIGHTING OF DIM SPACE-BASED OBJECTS

THESIS

Alec E. Cook, B.S.M.E.
Captain, USSF

Committee Membership:

Lt Col Robert A. Bettinger, Ph.D
Chair

Lt Col Bryan D. Little, Ph.D
Member

Maj John H. Hansen, Ph.D
Member

Abstract

The imaging and inspection of Resident Space Objects (RSOs) is an increasingly important mission as space-faring nations and commercial enterprises alike seek to develop means to repair and refuel spacecraft, as well as de-orbit RSOs to reduce orbital debris. Lighting conditions are not always advantageous for an imaging/inspection or repair/refuel spacecraft; therefore, the use of mirror spacecraft to reflect solar energy is proposed to illuminate dimly lit RSOs. The present research investigates the efficacy of space-based reflectors at examining spacecraft in the cislunar environment. Specific assessments include target spacecraft in geosynchronous Earth orbit and periodic orbits around selected Lagrange points, and reflectors in periodic orbits around selected Lagrange points. Additionally, survivability of ultra-thin Silver, Gold, and Aluminum coatings on flexible substrate materials is tested and examined.

Table of Contents

Page

List of Figures

List of Tables

CONCEPT OF OPERATIONS OF CISLUNAR MIRROR SATELLITES TO PROVIDE AUGMENTED LIGHTING OF DIM SPACE-BASED OBJECTS

I. Introduction

1.1 Background and Motivation

In the 1980's and 1990's, the U.S. and Russia were conducting research into the use of mirror satellites for reflecting solar energy back onto Earth. This energy would be used for illumination of large urban areas, emergency operations, or farming and enhancing photosynthesis. In the 1982 NASA Technical Paper "Illumination from Space with Orbiting Solar-Reflector Spacecraft," the authors describe several areas of technological development that would make space mirror systems more feasible. These include development of durable lightweight structures, structure deployment techniques, ultra-thin membranes, and reflective coatings. The Russian Znamya project began to test these ideas with two large satellites placed in orbit in the mid to late 1990's, though only one was successful. These mirror designs used extremely sparse apertures, yet still are reported to have reached luminosities equivalent to several full moons and serve as an early proof of concepts for space-based mirrors. In this new century, many advances have come about in the manufacture of membrane optics that were unavailable at the time when space-based mirrors were being aggressively researched. Extensive advances in these very technologies have taken place over the last decade and could render mirror satellites far more feasible. Space-based mirror application research has largely remained dormant for the past two decades. It has recently come to the forefront due to technological limits being reached for large,

monolithic space-based telescopes and the proliferation of cheaper, more accessible spacecraft production and launch vehicle services.

This research has endeavored to further space-based mirror research in two phases: numerical simulation and physical experimentation. For the numerical simulation phase, the effectiveness of mirror satellites reflecting solar energy to augment illumination of dimly-lit resident space objects (RSOs) will be examined for a variety of orbital conditions for both the mirror satellites and RSOs in the cislunar domain. Cislunar space, or the toroidal volume of space extending from approximately geosynchronous Earth orbit (GEO) out to and including the Moon's orbit, represents a critical region for U.S. space control initiatives as peer/near-peer competitors embark on robust cislunar/lunar missions. The research will advance the ongoing development of Space Situational Awareness (SSA) missions within the Earth-Moon system. The analytical focus on using dedicated mirror satellites to provide sources of augmented illumination is novel and could enable unique lighting opportunities to improve the current characterization of both natural and man-made objects in the near-Earth and cislunar space environments.

1.2 Thesis Prospectus

This research will advance ongoing research into Space Situational Awareness missions within the near-Earth and cislunar orbital domains. Research into mirror satellite orbit design is sought to improve the current characterization of both natural and man-made objects in the near-Earth and cislunar space environment. Previous research focused on applications of dedicated mirror satellites in sun-synchronous orbits and mirror inspector satellites in proximity operations. This effort seeks to expand the research to encompass the use of mirror satellites in the cislunar domain, and to investigate the survivability of mirrors to natural debris risks. Specifically, the

research will analyze various satellite constellation designs utilizing cislunar orbits to provide a baseline assessment of augmented lighting functionality in cislunar space. The research will use the Circular Restricted Three-Body Problem (CR3BP) as the primary dynamical models for cislunar trajectory generation, study, and analysis.

For the numerical simulation phase, the effectiveness of mirror satellites in reflecting solar energy to target RSOs will be examined for a variety of orbital conditions for both the mirror satellites and RSOs in the cislunar domain. Cislunar space, or the toroidal volume of space extending from approximately GEO out to and including the Moon's orbit, represents a critical region for U.S. space control initiatives as peer/near-peer competitors embark on robust cislunar/lunar missions. This research will build on FY21 analysis that investigated a concept of operations for mirror satellites in both low Earth orbit (LEO) and GEO. Factors that will be considered are the mirror satellite's effective range, magnitude and consistency of target illumination, appropriate orbital geometries, and engagement procedures. For the physical experimentation phase, the survivability of mirror samples will be tested with simulated debris fragments using a cold gas gun operated by Air Force Research Laboratory at Wright-Patterson AFB. Following impact testing, the mirror samples – each comprising different reflective materials – will be evaluated for reflectivity to discern residual reflective capabilities after incurring damage. The analytical focus on using dedicated mirror satellites to provide sources of augmented illumination is novel and could enable unique opportunities for both imaging and inspection missions.

1.3 Research Objectives

This research will investigate, within a simulation environment, the concept of operations for mirror satellites in cislunar space. The first phase of simulation will separate the imager and reflector to analyze the effectiveness of placing a large mirror

satellite in GEO or elsewhere in cislunar space to reflect light on a cislunar-based RSO for imaging by an inspector satellite. The second phase will feature the mirror affixed to an inspector satellite, thus creating a singular satellite system with imager and reflector.

This research will test the survivability of ultra-thin Silver, Gold, and Aluminum coatings on flexible substrate materials with simulated debris fragments using a cold gas gun. Due to pressure limitations of the cold gas gun apparatus, the debris impacts will be simulated for mirrors orbiting in GEO and higher within the cislunar domain. Following impact testing, the ultra-thin Silver, Gold, and Aluminum mirrors will be analyzed.

The output of this research will be a quantification of the benefits of a space-based mirror satellite constellation for SSA missions. Testing the current technological readiness of mirror satellite technology would provide quantifiable data as to the current state of membrane mirror technology. This scientific data could benefit its intended novel SSA missions as well as provide extremely useful data for astronomy and remote sensing applications that are reaching the technological mass and size limitations of monolithic mirrors structures. The results of the research will provide units within the USSF, such as the 1st Space Operations Squadron (1SOPS), with actionable information to pursue the active systems-level development of mirror satellites for future SSA operations. With space becoming increasingly competitive, congested, and contested, the ability to provide targeted illumination will greatly enhance a variety of missions that enable the characterization of RSOs throughout the Earth-Moon system.

1.4 Document Overview

This document is organized as follows. Chapter II provides an overview of relevant background information and literature review. Chapter III details the process of designing periodic orbits in the circular restricted three-body problem, augmenting and evaluating illumination of resident space objects, and material survivability testing of thin-film membrane mirrors. Chapter IV presents the results of simulation and experimental testing. Analysis of the space-based mirrors operational effectiveness and survivability characteristics are presented. Chapter V describes the methodology and results of two distinct experimental efforts with thin-film membrane mirrors: material survivability and reflectance testing. Finally, Chapter VI summarizes and provides conclusions for the total body of research, provides recommendations for future research, and discusses the relevance of the present research.

II. Background and Literature Review

The information contained in this chapter details the review of published information pertinent to research, development, and employment of space-based mirrors, basics of membrane mirror technology, and the dynamics and characteristics of the Circular Restricted Three-Body Problem.

2.1 Space-Based Mirrors

Early research efforts into orbiting solar reflectors consider the technology for military use, but not SSA or STM applications. The renowned German rocket scientist Hermann Oberth supported the Aggregat rocket program during World War II and proposed a large mirror orbiting the Earth that could concentrate the sun's energy into a single beam. The mirror, over a kilometer in diameter, could set fire to areas of enemy territory, burn cities, or even boil part of an ocean [9]. Oberth additionally describes what he calls "observer stations" that are placed in orbit around the earth and "could pin-point every detail on Earth and, with suitable reflectors, could send light signals to Earth." Oberth expands on potential capabilities of these orbiting stations, including telegraphic communication with places cut off from normal contact, observing and photographing unexplored countries and peoples, warning ships of icebergs, and even selling information reports to other nations at a high price [10].

United States military use of space-based mirrors for the purposes of ballistic missile defense was hypothesized in the 1985 Ballistic Missile Defense Technologies report by the U.S. Congress Office of Technological Assessment. This assessment followed President Reagan's Strategic Defense Initiative (Star Wars) and reported on the opportunities and risks involved in an accelerated program of research on new ballistic missile defense technologies, including those that might lead to deployment

of weapons in space [1]. In this hypothetical, multi-layered ballistic missile defense system the third layer would consist of a high-power, ground-based laser and orbiting reflectors to relay and aim the laser beam. The redirected laser beam would target a ballistic missile in the boost- or post-boost-phase of its flight to destroy it while the missile's rocket engine is burning or shortly after burnout. See Figure 1 below. No weaponized applications of space-based mirrors came to fruition; however, they are important in noting the attention drawn to reflected sunlight for tactical or strategic purposes.

Most early literature describes orbiting solar reflectors as an artificial source of sunlight in the terrestrial environment with varied applications. Buckingham and Watson [11], and Billman et al. [12] proposed configurations of solar reflectors for photovoltaic power generation in 1968 and 1977, respectively. The authors describe constellations of mirror satellites operating in orbital planes defined by elevation and required mirror diameter. Both provide deployment and structural concepts yet note

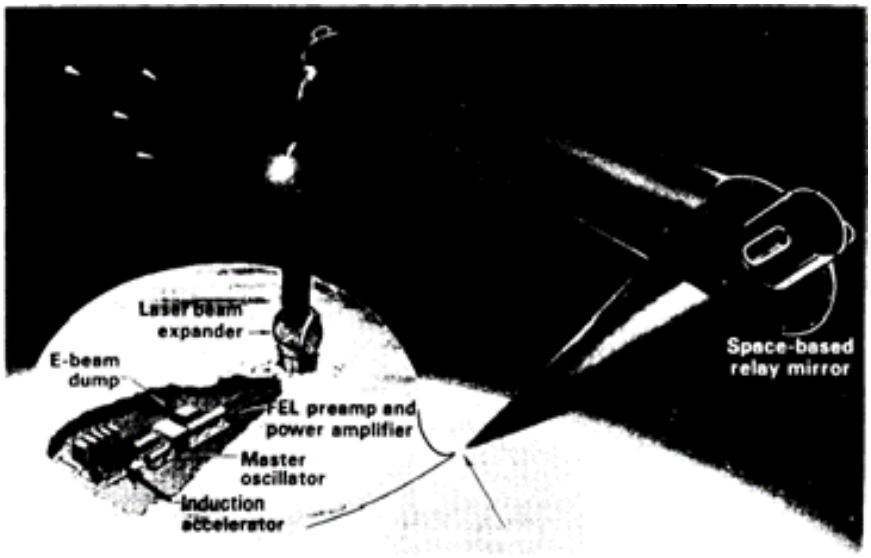

Figure 1: Space-based relay mirror reflecting a laser weapon towards an enemy ballistic missile [1].

drawbacks such as the large area required for solar farming and the significant cost of space launch hardware. Ehricke [13] produced a large body of research on orbiting solar reflectors starting in the 1970s. Ideas proposed include agricultural, power, illumination, and climate applications.

Canady and Allen's "Illumination from Space with Orbiting Solar-Reflector Spacecraft" for the NASA Langley Research Center in 1982 [2] is the most notable of the early literature on the topic of orbiting reflectors as it pertains to this research. A large portion is dedicated to the mission design of an augmented terrestrial lighting constellation, but it is the illumination metric derivation and the hypothesized augmented illumination of the Space Shuttle that most closely align with the objectives of this research.

Canady and Allen derive expressions for mirror optics that include reflectivity, surface, and path losses in detailed form with associated schematics; one of which is adapted for this research. See Figure 2 below. Natural sunlight travels through the cosmos and reaches a reflective surface. This surface reflects sunlight, creating a spot beam with varying characteristics depending on reflector size, orientation, and distance from target. The lower half of Figure 2 demonstrates the inverse relationship between spot beam distance and size.

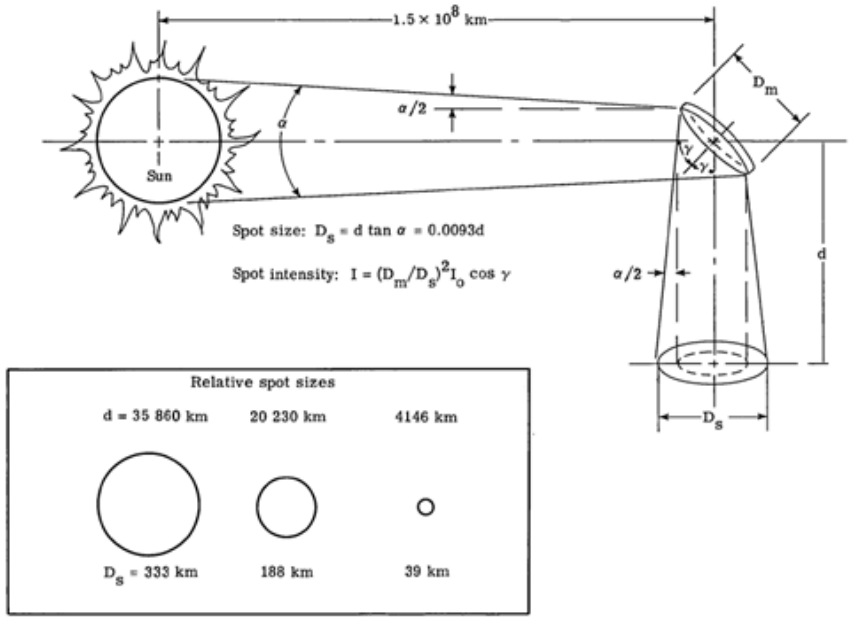

Figure 2: Schematic of orbiting reflector geometry and spot beam size [2].

The research of Canady and Allen is unique because it is the only documented literature reviewed for this research that conceptualizes the use of orbiting reflectors to illuminate other space objects. The case described by the authors is the illumination of the Space Shuttle during on-orbit nighttime operations. Although the Space Shuttle was equipped with lighting systems to illuminate operations near the Shuttle payload bay, this lighting system may not be sufficient for missions involving rendezvous, recovery, rescue, and assembly/servicing of large space systems when in Earth's penumbra or umbra [2]. The Shuttle is supported by space-based reflectors in a harmonic, synchronized orbit. Figure 3 depicts the Shuttle illumination operations, a concept that directly aligns with this research.

Government interest and funding for placing reflectors into orbit dried up through the 1970-80s, and projects were never realized in any physical sense. Znamya is the outlier in this case—it is the only hardware delivered into orbit to illuminate a distant region using a large orbiting reflector. Intended as a steppingstone to interplanetary

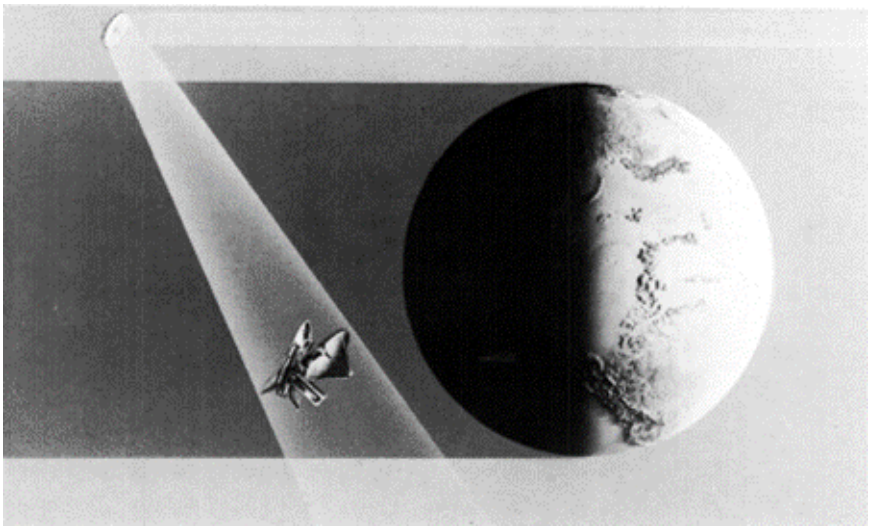

Figure 3: Artist rendering of an orbiting reflector illuminating a dimly lit Space Shuttle during operations [2].

solar sail technology, Znamya ("Banner" in Russian) was conceived by the brilliant Soviet engineer Vladimir Sergeevich Syromyatnikov. Syromyatnikov designed and developed the first manned spacecraft (Vostok) that carried Yuri Gagarin and the docking mechanism still used on the International Space Station today [3]. He dreamed of using solar sails, made from the same materials as a thin membrane mirror, to sail through the cosmos using stars' radiation pressure. Syromyatnikov convinced Soviet leaders that these solar sails would be capable of redirecting sunlight back towards earth, extending work hours and maximizing productivity. Academic literature on the Znamya projects is sparse. Semi-detailed accounts of mission planning and operations have been retained by Syromyatnikov himself [14].

In 1993, Syromyatnikov's illuminating solar sail idea was finally tested. Znamya-2 was built by Space Regatta Consortium, a partnership involving seven Russian aerospace management and engineering organizations. On 4 February 1993, Cosmonauts aboard the Mir space station commanding the Progress M-15 cargo spacecraft deployed the 20-m diameter thin film structure using centrifugal force. The reflector consisted of eight segments of metallic deposit on 5-micron thick Mylar film [14]. The

Znamya-2 space experiment created a sunlight spot beam about 2-3 times as luminous as the Moon and approximately 5-km in diameter that traveled from southern France to modern-day Belarus. Mass media outlets including the New York Times [15] reported on the Znamya experiments illuminating the night sky. Syromyatnikov had finally demonstrated his solar sail technology to the world.

The slightly larger Znamya-2.5 (25-m) test was carried out on 4 February 1999, aboard the Progress M-40 spacecraft from the Mir space station. The intent was to further demonstrate the effectiveness of thin film mirror technology and test a new manual attitude control mode [14]. A spacecraft control program issue left an antenna improperly positioned while the mirror deployed, destroying the mirror. After successfully stowing the antenna, the ground and space operators were unable to salvage the mirror structure and deploy it properly. The decision was made to send Znamya-2.5 into Earth's atmosphere and accept mission failure.

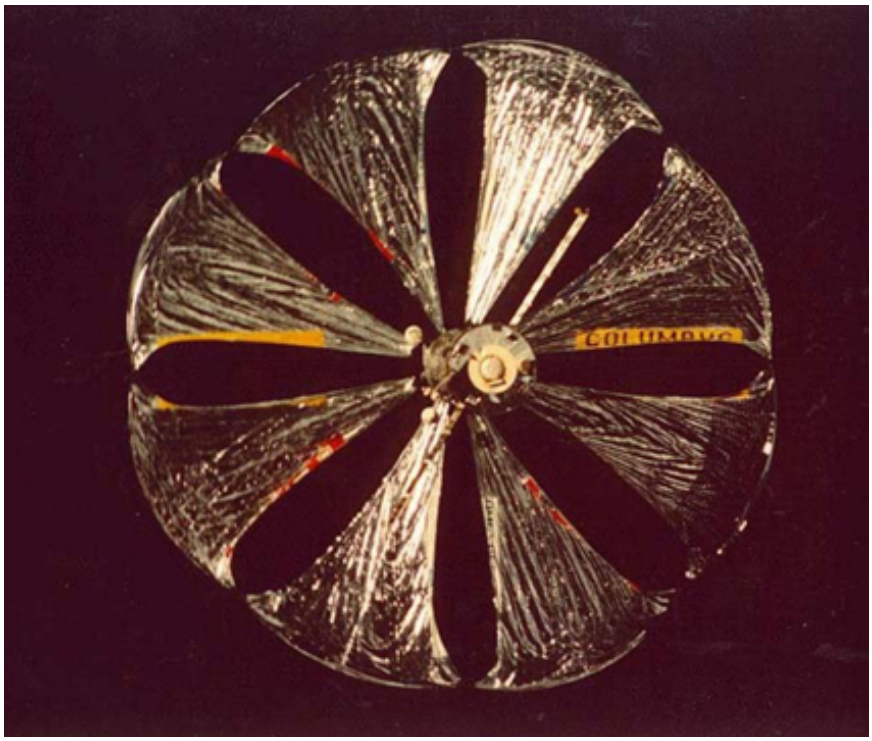

Figure 4: Znamya-2 deployed from the Progress cargo spacecraft [3].

Syromyatnikov and his Space Regatta Consortium had grand plans for orbiting reflectors and solar sailing spacecraft. The failure of Znamya-2.5 put an end to these plans—SRC never received funding to produce Znamya-3, the planned 70-m mirror. Through the years, Syromyatnikov addressed concerns raised by the environmental and astronomy communities regarding Znamya. Before the test of Znamya-2.5 the International Astronautical Union (IAU) of the Smithsonian Astrophysical Observatory at Harvard issued a circular citing a resolution from the 1997 IAU General Assembly in Kyoto: "large, luminous objects in orbit around the Earth is likely to 'have deleterious effects on astronomical observations, [and as] the night sky is the heritage of all humanity, which should therefore be preserved untouched, . . . the appropriate authorities [should] ensure that the night sky receives no less protection than has been given to the world heritage sites on Earth.' " [16]. Dr. David Crawford of the International Dark-Sky Organization stated of the Znamya project: "Indeed we are against these things. The night is a right, not just for astronomers, but for all." [17]. The President of the Royal Astronomical Society (RAS), Professor David Williams of University College, London, wrote on behalf of the RAS to Syromyatnikov and the SRC. The letter points out that the future development of astronomy could be seriously impeded by the light pollution of the night sky. In addition, radar studies of Earth's atmosphere could be seriously impacted [17]. Syromyatnikov addressed these concerns through open letters [14] but was never able to build Znamya-3.

Expensive, expendable launch systems and the high cost of spacecraft manufacturing throughout the 20th Century made constellations of orbiting reflectors unattainable. With recent advances in the commercial space industry and interest in renewable energy sources, academic research into solar reflectors has renewed. The research of Fraas et al. is focused on power generation with constellations of Sun-synchronous orbit spacecraft [18]. Large mirror arrays beam sunlight down to conventional ter-

restrial solar farms. Celik and McInnes developed an improved analytical method to model reflected solar energy [19]. This method incorporates more detailed geometry of illumination scenarios such as atmospheric transmission losses and solar panel orientation on the Earth's surface.

2.2 Membrane Mirrors

Advancements in the fields of materials science and structures have driven modern spacecraft to extremes. CubeSat development has created components and designs ever smaller and cheaper, with parts available for purchase by even the garage hobbyist. Military, civil, and commercial missions are often accomplished with boundary-pushing monolithic structures and systems. Gossamer spacecraft/structures have a future in both cases; they can be low cost, lightweight, packable, foldable, and can be deployed through nontraditional means once on orbit.

A membrane mirror is a reflector with a large diameter-to-thickness ratio. In this case, a membrane structure denotes that its primary mechanical loading is in tension; the structure is incapable of any bending or compressive loads [20]. The use of a membrane mirror to provide augmented illumination with reflected sunlight is a realistic application of gossamer structures. Solar sails may be the least technically demanding application of a reflective membrane structure, whereas a large primary telescope mirror is the most demanding. The complexity required for a non-imaging membrane mirror is achievable and considered a next step towards realizing gossamer structures for imaging and remote sensing.

When light is incident on a surface it must be transmitted, absorbed, or reflected. The fraction of incident light associated with each of these phenomena is specified by the three dimensionless ratios transmittance, absorptivity, and reflectance, respectively. This research is most concerned with the reflectance. When light is reflected

on a surface it can exhibit specular reflection, diffuse reflection, or both. A surface exhibits specular reflection when light reflects in such a manner that the angle of incidence is equal to the angle of reflection; the light can be described by Snell's Law. If the light is scattered at every angle, it exhibits diffuse reflection. A diffuse reflecting surface that scatters incident light equally in every direction is described as Lambertian [21].

Membrane mirrors used in space must provide the highest reflectance possible while having a low payload weight and volume. They are typically manufactured through chemical vapor deposition onto a thin film substrate such as Mylar or Kapton. Various metallic coatings have been explored throughout the literature [22] [2]; Aluminum is by far the most common metal due to its high reflectance and resistance to the space environment. Aluminum is also inexpensive (relative to other coatings), lightweight, and durable. The reflectance of aluminum remains relatively constant across the spectrum of visible and near-infrared light; see Figure 5 below. Although sodium has the highest reflectance (upper limit of about 0.99), it is unstable in the atmosphere and must be applied on orbit. Gold exhibits dynamic reflectance properties with respect to wavelength and is expensive; it is rarely used. Silver approaches the reflectance of sodium but does not stand up well to the space environment and requires a coating, which can be expensive, heavy, and inflexible.

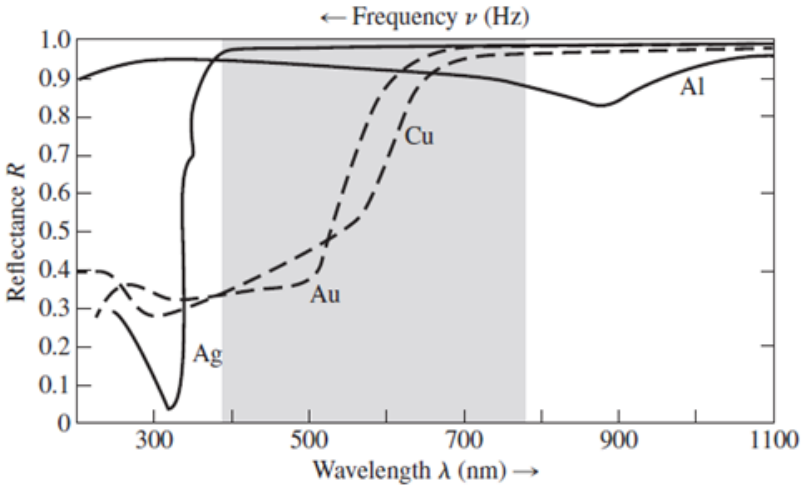

Figure 5: Reflectance versus wavelength for silver, gold, copper, and aluminum [4].

Overall performance of a reflective surface depends not only on the reflectance discussed above, but also on surface properties or flatness. Mirror flatness is generally desired within a small fraction of the sun's angular diameter or fraction of a wavelength. For instance, Lior [22] states that to solar incidence intensity on the earth spot within 5 percent of the maximal, all parts of a membrane mirror's surface must point in the same direction to within up to 2-mrad. This metric is also referred to as surface flatness coefficient. Canady and Allen [2] derive expressions to justify the use of a 0.90 surface flatness coefficient and point to membrane configuration tests conducted in 1980 and 1981 that achieved a root-mean-square (rms) edge gradient over the membrane surface estimated to be approximately 0.0002 rad.

2.3 Space-Based Mirrors Operating in Near-Earth Orbits

Preceding this research, Dombrowski modeled orbiting reflectors for SSA using rendezvous and proximity operations in near-Earth orbits [23]. Dombrowski's research demonstrated the ability of an inspector spacecraft with a single reflector to successfully illuminate all six sides of a target spacecraft in under one orbital period

using natural motion circumnavigation paired with a specific set of initial conditions. This relative orbit was designed with the Hill-Clohessy-Wiltshire equations such that it required zero fuel consumption, aside from combating perturbative forces on the reflector spacecraft, once the natural motion circumnavigation was initiated. Dombrowski determined that independent (non-collocated) reflector spacecraft separate from the inspector-target (deputy-chief) system were not necessary in the LEO and GEO regions. The comparison of non-collocated versus collocated systems is explored further in the present research. This research also draws heavily on the literature review performed by Dombrowski, namely his efforts on research and development of space-based mirror systems and how reflectivity is calculated and modeled in an orbital environment.

2.4 Summary

This chapter provided a background and summarized the literature review performed for the space-based mirror CONOPs and material survivability investigations. The reviewed research demonstrated that there is a significant opportunity to apply space-based mirrors for the purposes of Space Situational Awareness and Space Traffic Management in the cislunar region. Technological advancements have made large diameter, thin-film membrane mirrors a realizable capability. Due to the material sensitivity inherent in their design, these structures are much more susceptible to space-borne hazards like orbital debris.

III. CONOPs Investigation Methodology

The following chapter details the simulation and experimental test methodology used in this investigation. The simulation methodology is used to investigate the effectiveness of space-based mirrors when placed in various repeating orbits through the near-Earth and cislunar environments. The experimental test methodology is used to investigate material survivability of membrane mirrors when subjected to projectiles simulating man-made space object debris.

3.1 The Circular Restricted Three-Body Problem

The Circular Restricted Three-Body Problem (CR3BP) is used to model the dynamics of spaceflight at large distances from the Earth, where the Moon's gravity must also be accounted for. In the CR3BP, the Moon and Earth are orbiting their center of mass in circular orbits. The third body in this problem is the spacecraft, which orbits with respect to a frame placed at the barycenter of the Earth-Moon system. The spacecraft is assumed to have negligible mass compared to both the Earth and the Moon. The reference frame at the barycenter rotates with the system and is shown in Figure 6:

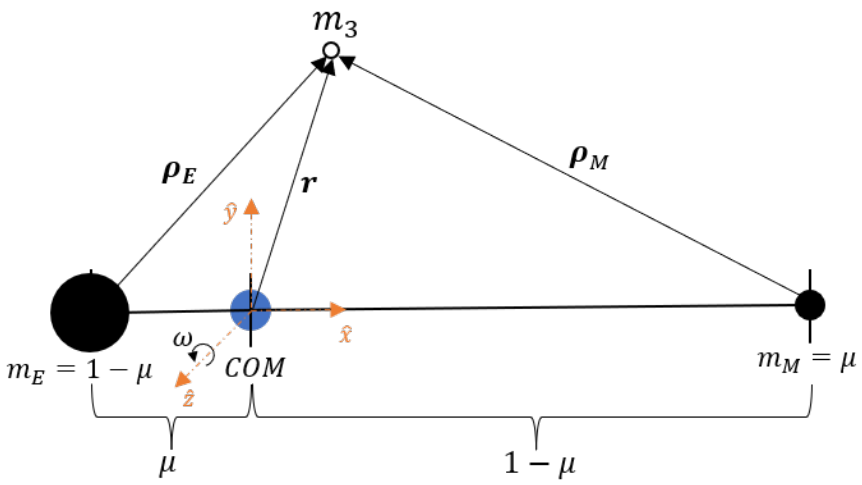

Figure 6: The Rotating Earth-Moon Reference Frame

In the CR3BP reference frame, the Earth and Moon are both located on a shared x-axis with non-dimensional distances from the origin of (-μ, 0, 0) and ($1 - \mu$, 0, 0), respectively. The three-body parameter μ is unique to each three-body system of study (i.e. Earth-Moon, Sun-Earth) and can provide insights into the behavior of specific three-body systems, such as stability [24]. The three-body parameter quantifies relationships between masses and physical locations of the two primary celestial bodies in a three-body problem. The CR3BP is non-dimensionalized for ease-of-use and display purposes. Distances and velocities can be different by orders of magnitude, and non-dimensionalizing translates the problem into a presentable format that is suited for numerical computations. The non-dimensional equations of motion for the CR3BP are shown in Equations (1-3):

$$\ddot{x} = x + 2\dot{y} - \frac{(1-\mu)(x+\mu)}{\rho_E^3} - \frac{\mu(x-1+\mu)}{\rho_M^3} \tag{1}$$

$$\ddot{y} = y - 2\dot{x} - \frac{(1-\mu)y}{\rho_E^3} - \frac{\mu y}{\rho_M^3} \tag{2}$$

$$\ddot{z} = -\frac{(1-\mu)z}{\rho_E^3} - \frac{\mu z}{\rho_M^3} \tag{3}$$

where the scalar distance of the spacecraft with respect to the Earth and Moon in the rotating reference frame is written as Equations (4) and (5), respectively:

$$\rho_E = \sqrt{(x+\mu)^2 + y^2 + z^2} \tag{4}$$

$$\rho_M = \sqrt{(x-1+\mu)^2 + y^2 + z^2} \tag{5}$$

The non-dimensional values DU, TU, and μ, as well as constants used in this analysis are provided in Table 1 below. The non-dimensional units are used in the dynamics of the CR3BP and have dimensional equivalents.

Table 1: CR3BP Characteristic Quantities and Constants

Parameter	Value
Distance Unit (DU)	384,400 km
Time Unit (TU)	4.3425 days
μ	0.0121505
G	$6.674 \times 10^{-20} \frac{Nkm^3}{kg^2}$
m_{Earth}	5.9722×10^{24} kg
m_{Moon}	7.347×10^{22} kg

Setting the relative velocities and accelerations in Equations (1-3) equal to zero, five equilibrium points of the Earth-Moon system are found. These five Lagrange points, L_i, while stationary in the rotating CR3BP frame, are in constant motion when viewed inertially. Two of the Lagrange points take the form of an equilateral triangle solution, in which L_4 or L_5 are located at one vertex and the Earth and Moon are located at the others. The location of these points can be solved simply through geometry. The other three Lagrange points take the form of a collinear solution, in which the Earth and Moon separate the three points along a line. The location of

these points must be solved for with the application of a root finding algorithm like the Newton-Raphson method. The locations of the five Lagrange points are presented in Table 2 with a visual depiction in Figure 7.

Table 2: CR3BP Lagrange Points

Lagrange Point	x Position (DU)	y Position (DU)
L_1	0.837	0
L_2	1.156	0
L_3	-1.005	0
L_4	0.488	0.866
L_5	0.488	-0.866

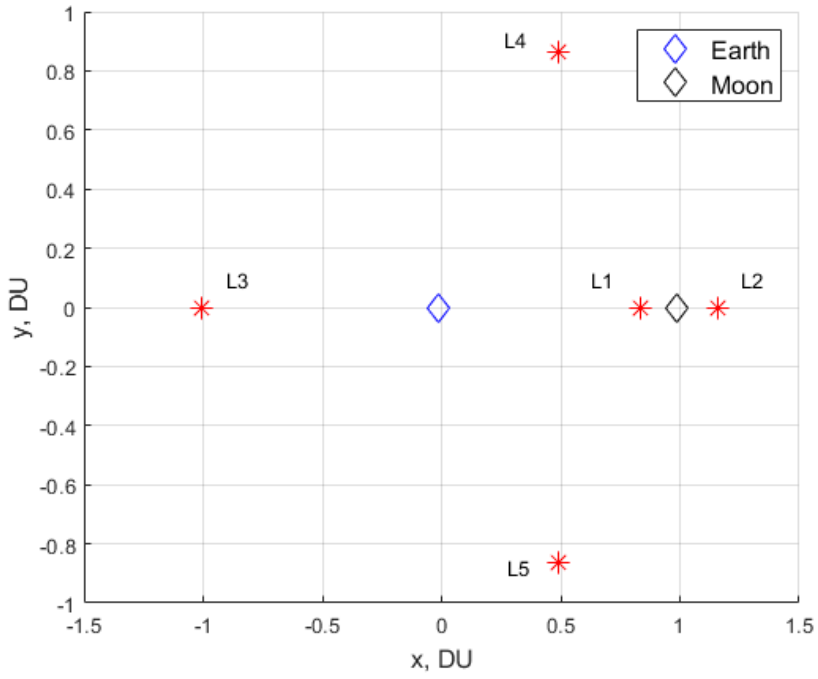

Figure 7: The Earth-Moon Lagrange Points

Through inspection of Equations (1-3) above, a pseudopotential function U can be defined such that [25]:

$$U(x,y,z) = \frac{1}{2}(x^2+y^2) + \frac{1-\mu}{\rho_E} + \frac{\mu}{\rho_M} \tag{6}$$

and Equations (1-3) become:

$$\ddot{x} - 2\dot{y} = \frac{\partial U}{\partial x} \tag{7}$$

$$\ddot{y} + 2\dot{x} = \frac{\partial U}{\partial y} \tag{8}$$

$$\ddot{z} = \frac{\partial U}{\partial z} \tag{9}$$

Performing a vector dot product of Equation (8) with $[\dot{x}\ \dot{y}\ \dot{z}]^T$ and integrating with respect to time yields a perfect integral of the relative equations of motion known as Jacobi's integral:

$$C = (x^2+y^2) + 2\frac{1-\mu}{\rho_E} + 2\frac{\mu}{\rho_M} - v^2 \tag{10}$$

Jacobi's constant, C, is an energy-like constant that exists in the CR3BP determined through initial conditions. It is the classical energy integral ($T + V = Constant$) expressed in rotating coordinates [25]. This constant is important in the study of the CR3BP due to the lack of fixed-path limit cycles. A Jacobi constant associated with specific initial conditions exhibits a zero velocity curve, a region to which the unforced trajectory is bound. Without external forces (thrust), a trajectory will remain inside its zero velocity curve forever. The path it travels inside this curve is highly chaotic and dependent on initial states. See Figure 8 for the zero velocity curves associated with the Lagrange points.

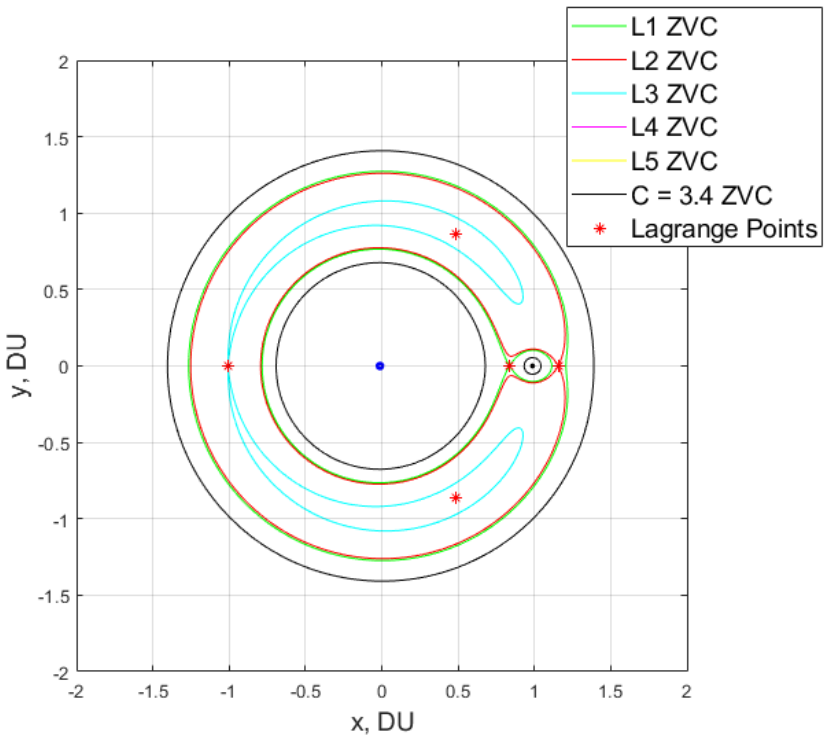

Figure 8: The Zero Velocity Curves Associated with the Lagrange Points

Stability in the CR3BP is analyzed via Lyapunov's Indirect Method: the Jacobian matrix is evaluated at each of the five Lagrange points. Since this research focuses on orbits in the vicinity of L_1, the stability around this Lagrange point is detailed below. The CR3BP Jacobian matrix is:

$$A = \begin{bmatrix} 0 & 0 & 0 & 1 & 0 & 0 \\ 0 & 0 & 0 & 0 & 1 & 0 \\ 0 & 0 & 0 & 0 & 0 & 1 \\ U_{xx} & U_{xy} & U_{xz} & 0 & 2 & 0 \\ U_{yx} & U_{yy} & U_{yz} & -2 & 0 & 0 \\ U_{zx} & U_{zy} & U_{zz} & 0 & 0 & 0 \end{bmatrix} \tag{11}$$

where:

$$U_{ij} = \frac{\partial^2 U}{\partial i \partial j} \tag{12}$$

Evaluating this Jacobian at L_1 results in one stable eigenvalue, one unstable eigenvalue, and two complex conjugate pair of marginally stable eigenvalues. The L_1 point is actually a saddle point. It has stable and unstable manifolds defined by the eigenvectors paired with their respective stable and unstable eigenvalues. There are no fully stable points in the CR3BP.

3.2 Periodic Orbit Development

This section describes the process of designing and simulating the dynamics of an orbital scenario in the CR3BP. Topics covered include the iterative simple corrector method, the parameter continuation method, selection of target, reflector, and observer orbits, proximity operations used in near-Earth orbits, and Earth-frame to CR3BP-frame coordinate transformations used with Earth orbits or Sun vectors.

3.2.1 Simple Corrector Method

Due to the chaotic nature of multi-body dynamics, locating periodic orbits poses a unique challenge. The methodology used in the present research is to linearize the motion around the Lagrange points to find an initial guess for the periodic orbit. This initial guess is then used in a simple corrector, where a single shooter method adjusts the initial conditions until a periodic orbit is found for the full nonlinear dynamics. Linearizing motion about the L_1 Lagrange point produces the following equations:

$$\xi = -A_\xi \cos(s\tau + \phi) + L_{1,x} \tag{13}$$

$$\eta = \beta_3 A_\xi \sin(s\tau + \phi) \tag{14}$$

$$\dot{\xi} = sA_\xi \sin(s\tau + \phi) \tag{15}$$

$$\dot{\eta} = s\beta_3 A_\xi \cos(s\tau + \phi) \tag{16}$$

where:

$$\beta_1 = 2 - \frac{U_{xx} + U_{yy}}{2} \tag{17}$$

$$\beta_2^2 = -U_{xx}U_{yy} > 0 \tag{18}$$

$$\beta_3 = \frac{s^2 + U_{xx}}{2s} \tag{19}$$

$$s = \sqrt{\beta_1 + (\beta_1^2 + \beta_2^2)^{1/2}} \tag{20}$$

and U_{xx} and U_{yy} are the second partial derivatives of the potential function U:

$$U_{xx} = \frac{\partial^2 U}{\partial x \partial x} = 1 + \frac{3(x+\mu)^2(1-\mu)}{\rho_E^5} - \frac{1-\mu}{\rho_E^3} + \frac{3\mu(x+\mu-1)^2}{\rho_M^5} - \frac{\mu}{\rho_M^3} \tag{21}$$

$$U_{yy} = \frac{\partial^2 U}{\partial y \partial y} = 1 + \frac{3y^2(1-\mu)}{\rho_E^5} - \frac{1-\mu}{\rho_E^3} + \frac{3\mu y^2}{\rho_M^5} - \frac{\mu}{\rho_M^3} \tag{22}$$

Motion about the other Lagrange points can be linearized in a similar fashion, and follows the detailed development in Szebehely [24]. In the present research, elements of the linearized equations were selected such that initial guesses for orbits with periodic motion about the L_1, L_2, and L_4 were obtained. These Lagrange points' relative proximity to both the Moon and Earth-Moon corridor make them promising candidates for potentially effective SSA and illumination.

Following the methodologies presented by Grebow [26], these linearized initial guesses were used in simple targeting algorithms to correct for the actual nonlinear dynamics and find repeating trajectories. The first targeting scheme exploits symmetry about the x-z plane of the synodic frame to determine periodic solutions in the vicinity of the collinear Lagrange points. This method was used for the generation of L_1 and L_2 orbits. Starting with an initial state vector of the form:

$$\bar{q}_0 = \begin{bmatrix} x_0 & 0 & 0 & 0 & \dot{y}_0 & 0 \end{bmatrix}^T$$

the nonzero components of the initial state vector are adjusted to achieve a perpendicular crossing at the endpoint, thereby completing one half-period of a periodic orbit. The initial state vector is adjusted with the following z_0 and $\dot{y}_0$ corrections:

$$\begin{bmatrix} \delta z_0 \\ \delta \dot{y}_0 \end{bmatrix} \approx \begin{bmatrix} \Phi_{43} - \Phi_{23}\frac{\ddot{x}_{T/2}}{\dot{y}_{T/2}} & \Phi_{45} - \Phi_{25}\frac{\ddot{x}_{T/2}}{\dot{y}_{T/2}} \\ \Phi_{63} - \Phi_{23}\frac{\ddot{z}_{T/2}}{\dot{y}_{T/2}} & \Phi_{65} - \Phi_{25}\frac{\ddot{z}_{T/2}}{\dot{y}_{T/2}} \end{bmatrix}^{-1} \begin{bmatrix} -\dot{x}_{T/2} \\ -\dot{z}_{T/2} \end{bmatrix} \tag{23}$$

where Φ_{ij} are elements of the integrated state transition matrix from a single shooting targeting algorithm. Iterating with Equation 23 while keeping $x_0 = x_C$, where x_C is a constant near the area of interest, and $y_0 = 0$ will provide an adjusted initial state vector that can then be used to propagate the periodic orbit with Equations (1-3) using a numerical integrator.

The second targeting scheme solves for asymmetric periodic orbits and takes a slightly different form. Because there is no natural symmetry to exploit, the initial position must be targeted through one full orbital period. The planar form of this method was used for the generation of L_4 orbits. Starting with an initial state vector of the form:

$$\bar{q}_0 = \begin{bmatrix} x_0 & y_0 & 0 & \dot{x}_0 & \dot{y}_0 & 0 \end{bmatrix}^T$$

The initial state vector is adjusted with the following x_0 and $\dot{x}_0$ corrections:

$$\begin{bmatrix} \delta x_0 \\ \delta \dot{x}_0 \end{bmatrix} \approx \begin{bmatrix} \Phi_{11} - \Phi_{21}\frac{\dot{x}}{\dot{y}} - 1 & \Phi_{14} - \Phi_{24}\frac{\dot{x}}{\dot{y}} \\ \Phi_{41} - \Phi_{21}\frac{\ddot{x}}{\dot{y}} & \Phi_{44} - \Phi_{24}\frac{\ddot{x}}{\dot{y}} - 1 \end{bmatrix}^{-1} \begin{bmatrix} \delta x \\ \delta \dot{x} \end{bmatrix} \tag{24}$$

where Φ_{ij} are elements of the integrated state transition matrix from a single shooting targeting algorithm. Iterating with Equation (24) while keeping $y_0 = y_C$ and $\dot{y}_0 = y_V$, where y_C and y_V are constant values near the area of interest, will provide an adjusted initial state vector that can then be used to propagate the periodic orbit with Equations (1-3) using a numerical integrator.

3.2.2 Parameter Continuation Methods

Once a periodic orbit is found in the nonlinear dynamics, a family of orbits can be developed using a parameter continuation scheme. A family of orbits is a set of orbits that are characterized in terms of a designated parameter [27]. As the parameter evolves continuously, properties of the family (period and stability) vary continuously [28]. In natural parameter continuation a physical parameter is selected, such as starting location of an orbit along the x-axis. The natural parameter continuation scheme used in the present study involves the predictor-corrector process described by Markellos and Halioulias and Grebow [28, 26]. In the predictor step, a selected parameter Δq is varied by a small step size δs. In Equation (25) steps are taken along the x-axis, so Δq only has an x-component. Using targeting algorithms, this predicted location is corrected to find the next member of the family. This process is repeated until the desired number of family members is found or the family terminates.

$$q_0^n = q_0^{n-1} + \delta s \cdot \Delta q \tag{25}$$

$$\Delta q = \begin{bmatrix} 1 & 0 & 0 & 0 & 0 & 0 \end{bmatrix}^T$$

The natural parameter continuation method described above and in Equation (25) is used for producing orbit families at the collinear Lagrange points (L_1, L_2, and L_3) because it requires modification of only one state variable (x-position, for example). Forming periodic orbit families at the equilateral Lagrange points (L_4 and L_5) is considerably more involved mathematically. Dahlke [29] provided the pseudo-arclength parameter continuation method used to form a Planar family around L_4. The natural parameter continuation method exploits the symmetry of periodic orbits and the parameter used to modify initial states typically has physical meaning to the problem. In the pseudo-arclength method, parameters do not necessarily carry physical meaning and can be employed with asymmetric orbit families.

3.2.3 Target, Observer, and Reflector Orbits

Scenarios in this research consist of three main systems: the target, the observer, and the reflector. The target is the RSO requiring illumination to be detected. The observer is the system responsible for performing detection. The reflector, which is either isolated as a standalone system or collocated with the observer, is the space-based mirror responsible for reflecting light onto the target. Figure 9 depicts the orbits designed and implemented for this research. For scenarios in this research, target and observer spacecraft were placed in GEO, periodic L_1 orbits, and periodic L_2 orbits. The previously described method of designing NMC orbits was implemented to place the observer nearby the target in GEO. The previously described parameter

continuation scheme was implemented to place the observer nearby the target and inside the same orbital family (Lyapunov, Halo) when in periodic orbits about L_1 and L_2. The reflector spacecraft can be placed in a different family of orbits from the target/observer, such as: L_1 Lyapunov/Halo, L_2 Lyapunov/Halo, or L_4 Planar. The reflector spacecraft can also be collocated with the observer spacecraft to comprise an integrated system where all portions are performed inside the same orbital family. Both forms are investigated at present.

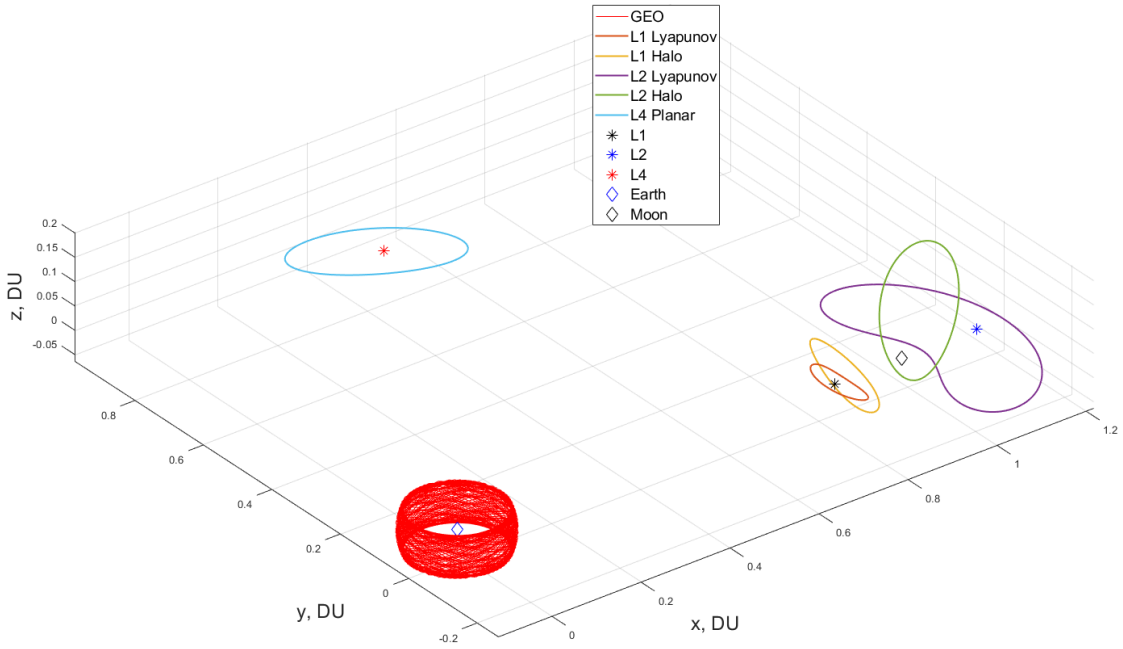

Figure 9: Periodic Orbits Developed for preliminary CONOPs investigation

3.2.4 Proximity Operations in GEO

GEO is a highly valuable orbit because the altitude is such that the orbital period perfectly matches the period of the Earth's rotation. This makes a satellite in GEO appear stationary above a fixed point on the Earth, allowing for continual viewing of a single region [30]. The altitude of these orbits is $35,786$ km with a period of 23 hours 56 minutes and 4 seconds. To calculate a geostationary orbit an initial condition must

be selected with the position at the altitude of $35,786$ km and the velocity needs to be completely perpendicular to the position vector with a magnitude determined by:

$$v = \frac{2\pi r}{T},$$

where r is the altitude ($35,786$ km) and T is the period (23 hours 56 minutes and 4 seconds).

This initial condition can then be propagated using the two-body problem equations of motion given in Equation (26), which gives the satellites orbit in the Earth-Centered Inertial (ECI) reference frame [31].

$$\ddot{\vec{r}} = -\frac{\mu \vec{r}}{r^3} \tag{26}$$

A spacecraft in GEO can be effectively observed by another spacecraft that is placed in a simple natural motion circumnavigation (NMC) orbit. The linearized equations of relative motion, or Hill-Clohessy-Wiltshire (HCW) equations, can be employed to accomplish this by selecting appropriate initial conditions relative to the chief's (target's) orbit in the radial and in-track directions [32]:

$$\dot{y}(0) = 2nx(0) \tag{27}$$

The effectiveness of these initial conditions to produce an NMC is predicated upon assumptions inherent in the HCW equations, namely a circular chief orbit and a small relative distance compared to orbital radius. Both assumptions hold in the case of a GEO chief/target satellite.

3.2.5 Converting from Earth-Centered Inertial (ECI) to Barycenteric Synodic (CR3BP) Reference Frame

Transferring between reference frames can be useful for numerous reasons including visualization of the orbit. In the present study, conversion from ECI to the CR3BP reference frame is needed for two primary reasons: (i) calculation of the position of the Sun, and (ii) converting GEO into the synodic reference frame. The model to find illumination of the target requires the phase angle of the Sun as seen in Equation (72), which requires knowledge of the position of the Sun. Vallado [33] provides code that calculates the position of the Sun given a Julian Date in ECI. The sun's position needs to be converted into the CR3BP reference frame. The GEO orbit is calculated in the ECI frame by using the two-body equations of motion as seen in Equation (26), which then need to be converted into the synodic reference frame to perform analysis.

To complete the transfer of reference frames we need start with some simplifying assumptions. First, for the sake of simplicity, the inclination of the moon's orbit with respect to the Earth's ecliptic plane is a constant $\psi = 23.5$ deg. Second, we assume the inertial frame and the synodic reference frame are initially aligned. Figure 10 depicts how these reference frames are related with the stated assumptions. There are three simple steps required to change between these reference frames [34]:

- Convert to nondimensional units
- Rotate about the common $\hat{y}$ and $\hat{z}$-axes using the following rotating matrix for the full state (position and velocity):

$$R^{IS} = \begin{bmatrix} R_2(-\psi)R_3(\theta) & [0] \\ R_2(-\psi)\frac{d}{dt}R_3(\theta) & R_2(-\psi)R_3(\theta) \end{bmatrix}$$

where R_2 and R_3 are 2-axis and 3-axis rotation matrices, respectively

- Translate from Earth-center to barycentric by subtracting μ from the x-position

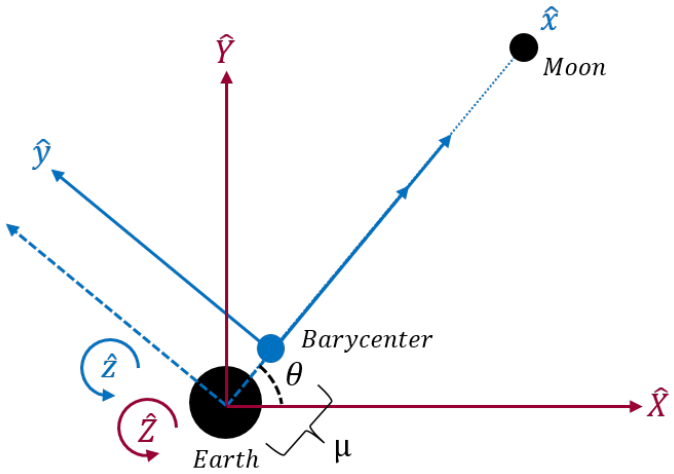

Figure 10: Conversion from ECI to Barycentric Synodic (CR3BP) Reference Frame

3.3 Controlling Motion in the Circular Restricted Three-Body Problem

This section describes two different control schemes used in this research to track a desired orbit in the vicinity of L_1, L_2, or L_4. The two methods presented are Linear Quadratic Regulator and Sliding Mode Control. Sets of linearized equations of motion for L_1, L_2, or L_4 are also presented, as they are required in the employment of Linear Quadratic Regulator control.

3.3.1 Linear Motion Near L_1 and L_2

The desired orbit is an analytical solution to the linearized equations of motion detailed in Szebehely [24] that closely represents in size the periodic orbits developed in Section 3.2. The orbit at L_1 is a Lyapunov orbit, meaning it is planar and exhibits symmetry about the x-z plane of the synodic frame. The L_1 orbit is described by

equations of motion in ξ, η, and ζ corresponding to x, y, and z coordinates with respect to L_1:

$$\xi = -Acos(st + \phi) \tag{28}$$

$$\eta = A\beta_3 sin(st + \phi) \tag{29}$$

$$\zeta = 0 \tag{30}$$

$$\dot{\xi} = sAsin(st + \phi) \tag{31}$$

$$\dot{\eta} = sA\beta_3 cos(st + \phi) \tag{32}$$

$$\dot{\zeta} = 0 \tag{33}$$

and the following parameters are used:

$$T = 2\pi s \tag{34}$$

$$A = 0.02 \text{ DU} \tag{35}$$

$$\phi = 0 \tag{36}$$

With control applied, the CR3BP EOMs take the form of Equations (37-39) below:

$$\ddot{x} = x + 2\dot{y} - \frac{(1-\mu)(x+\mu)}{\rho_E^3} - \frac{\mu(x-1+\mu)}{\rho_M^3} + u_x \tag{37}$$

$$\ddot{y} = y - 2\dot{x} - \frac{(1-\mu)y}{\rho_E^3} - \frac{\mu y}{\rho_M^3} + u_y \tag{38}$$

$$\ddot{z} = -\frac{(1-\mu)z}{\rho_E^3} - \frac{\mu z}{\rho_M^3} + u_z \tag{39}$$

The same method is applied to develop linear orbits around L_2 with ξ, η, and ζ corresponding to the x, y, and z coordinates relative to L_2. The left half of Figures 11 and 12 depict linear orbits around L_1 and L_2, respectively. The right half of each figure demonstrate the need for some sort of control action to follow the desired

trajectory. When subjected to the nonlinear dynamics of the CR3BP, a lack of control allows the trajectories to quickly diverge from their linear solutions. The response around L_1 in Figure 11 stays inside the zero velocity curve associated with the Jacobi constant at L_1, while the response around L_2 in Figure 12 appears to "tour" around the Earth-Moon system. The initial conditions at L_2 are energetic enough to remain outside the L_1 zero velocity curve, at least for a finite period of time.

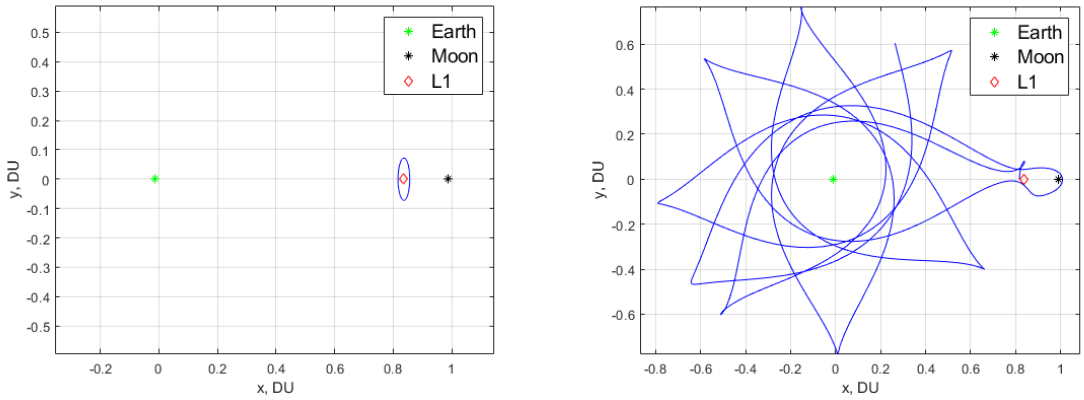

Figure 11: Left: Linear orbit at L_1, Right: Attempted orbit without control actions

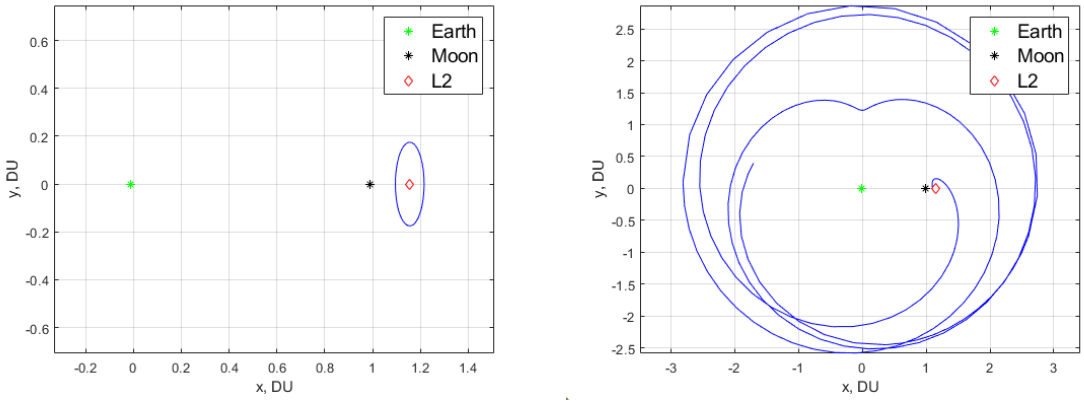

Figure 12: Left: Linear orbit at L_2, Right: Attempted orbit without control actions

3.3.2 Linear Motion Near L_4

The linear equations of motion around L_4 are more complex than L_1 and L_2, but are also given a detailed treatment in Szebehely [24]. An abbreviated derivation begins with the following solution, noting that it includes two angular frequenices, or mean motions (s_1 and s_2):

$$\xi = C_1 cos(s_1 t) + S_1 sin(s_1 t) + C_2 cos(s_2 t) + S_2 cos(s_2 t) \tag{40}$$

$$\eta = \bar{C_1} cos(s_1 t) + \bar{S_1} sin(s_1 t) + \bar{C_2} cos(s_2 t) + \bar{S_2} cos(s_2 t) \tag{41}$$

where:

$$\bar{C_i} = \Gamma_i (2 s_i S_i - \Omega_{xy} C_i) \tag{42}$$

$$\bar{S_i} = -\Gamma_i (2 s_i C_i + \Omega_{xy} S_i) \tag{43}$$

$$\Gamma_i = \frac{1}{s_i^2 + \Omega_{yy}} > 0 \tag{44}$$

$$s_1 = \sqrt{6.75\mu} \quad \text{and} \quad s_2 = 1 - 3.375\mu \tag{45}$$

$$\Omega_{xx} = \tfrac{3}{4}, \quad \Omega_{xy} = \tfrac{3\sqrt{3}}{2}(\mu - \tfrac{1}{2}), \quad \Omega_{yy} = \tfrac{9}{4} \tag{46}$$

The short- or long-term periods can be eliminated from Equations (40) and (41) by selecting appropriate initial conditions. Eliminating the short-period terms from the solution yields:

$$\xi_0 = C_1, \quad \eta_0 = \bar{C_1} \tag{47}$$

$$\dot{\xi}_0 = S_1 s_1, \quad \dot{\eta}_0 = \bar{S_1} s_1 \tag{48}$$

The initial conditions ξ_0 and η_0 are selected from Section 3.2, while $\dot{\xi}_0$ and $\dot{\eta}_0$ are computed using the relationships above. The following initial states are used:

$$\bar{X}_0 = \begin{bmatrix} 0.0520 \\ -0.0520 \\ 0.0 \\ -0.0148 \\ -0.0180 \\ 0.0 \end{bmatrix} \tag{49}$$

The left half of Figure 13 shows the linear orbit around L_4 used in this research. The right half is a similar representation to Figures 11 and 12, depicting the attempted linear orbit with control actions. The trajectory remains near the semi-stable L_4 point, but propagates in a chaotic path.

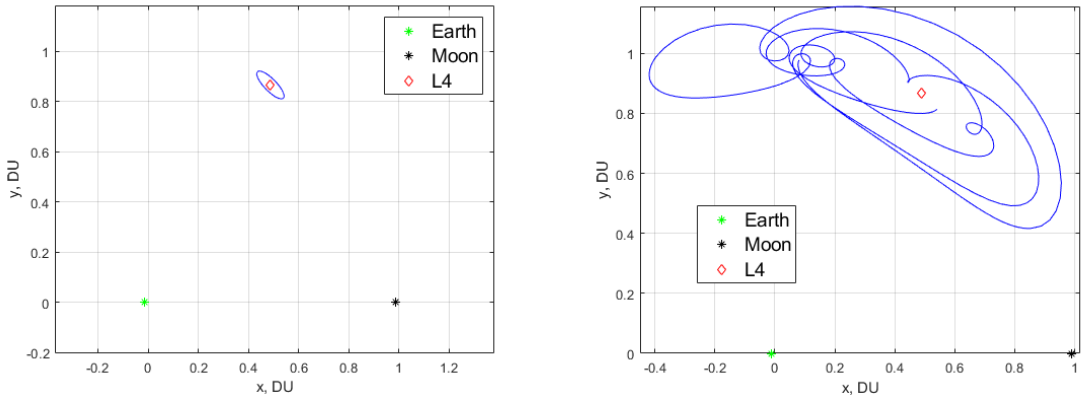

Figure 13: Left: Linear orbit at L_4, Right: Attempted orbit without control actions

3.3.3 Linear Quadratic Regulator

The linear quadratic regulator (LQR) is one of the most widely used controllers. It is designed with linear system concepts but can be applied to nonlinear systems sufficiently close to equilibrium points, like orbits in the CR3BP near Lagrange points. The LQR controller defines an optimal constant K such that a cost function, subject to system dynamics, is minimized. The LQR problem is solved by the Algebraic Ri-

catti Equation, a quadratic matrix equation [35]. In this research, the LQR feedback-state controller was designed and implemented based on a linearization around the L_1, L_2, and L_4 Lagrange points utilizing the MATLAB 'lqr' command:

$$\text{K} = \text{lqr(A, B, Q, R)}$$

The A matrix is the Jacobian from Equation (11) and the B matrix is the system input matrix:

$$B = \begin{bmatrix} 0 & 0 & 0 \\ 0 & 0 & 0 \\ 0 & 0 & 0 \\ 1 & 0 & 0 \\ 0 & 1 & 0 \\ 0 & 0 & 1 \end{bmatrix} \tag{50}$$

Q and R are user-defined weighting matrices and must be positive semi-definite and positive definite, respectively. They are used as tuning parameters to achieve desired performance. The weighting on the states (Q) and the control effort (R) are determined by following the methodology in [36], where e is the maximum allowable error(s) on the state(s) and u is the maximum allowable value(s) of the control variable(s).

$$\alpha = 1 \tag{51}$$

$$\beta = 1 \tag{52}$$

$$e = 1 \text{ x } 10^{-5} \tag{53}$$

$$u = 0.5 \tag{54}$$

The value e was set based off of an estimated allowable error in trajectory relative to the linear solution. An e value of 1 x 10^{-5} corresponds to a trajectory error of approximately 3.8 km, and was set based off of estimated spacecraft propulsion system capability and total mass [37]. The α and β parameters are tunable controller values.

$$Q = \begin{bmatrix} \frac{\alpha^2}{e^2} & 0 & 0 \\ 0 & \frac{\alpha^2}{e^2} & 0 \\ 0 & 0 & \frac{\alpha^2}{e^2} \end{bmatrix} \tag{55}$$

$$R = \begin{bmatrix} \frac{\beta^2}{u^2} & 0 & 0 \\ 0 & \frac{\beta^2}{u^2} & 0 \\ 0 & 0 & \frac{\beta^2}{u^2} \end{bmatrix} \tag{56}$$

In this research, a constant e and u are applied to every state and control variable, respectively. Once the gain matrix K has been produced, the simple linear state-feedback control law in Equation (57) is applied to the system.

$$\bar{u} = -K(\bar{q} - \bar{q}_{des}) \tag{57}$$

3.3.4 Sliding Mode Control

Sliding mode control is a robust control method and an approach used to handle model imprecisions. Imprecise models can come from actual uncertainties or intentional simplifications. The uncertainty modeled in this research is the ability of the x- and y-axis spacecraft thrusters to impart the proper amount of force necessary to track a linear orbit. The thrusters are modeled for simulation as under-performing, with randomly generated actual thrust values between 90% to 100% of requested thrust. This is summarized in Table 3 and represented in the modified equations of motion in Equations (58) and (59):

Table 3: Simulated Thruster Performance Uncertainties

Thruster	Range of Operation	Actual Value
x-axis	$0.90 \leq b_x(t) \leq 1.00$	$0.90 \leq$ Randomly generated value ≤ 1.00
y-axis	$0.90 \leq b_y(t) \leq 1.00$	$0.90 \leq$ Randomly generated value ≤ 1.00

$$\ddot{x} = x + 2\dot{y} - \frac{(1-\mu)(x+\mu)}{\rho_E^3} - \frac{\mu(x-1+\mu)}{\rho_M^3} + b_x(t)u_x \tag{58}$$

$$\ddot{y} = y - 2\dot{x} - \frac{(1-\mu)y}{\rho_E^3} - \frac{\mu y}{\rho_M^3} + b_y(t)u_y \tag{59}$$

The following details implementation of a sliding mode controller for the x-axis. The y-axis controller was designed in the same manner and is not reproduced here. Sliding mode control is implemented in this research as outlined in Slotine and Li [38], where the tracking error vector is defined as the difference in state vector and desired state:

$$\tilde{x} = x - x_d \tag{60}$$

and further:

$$\dot{\tilde{x}} = \dot{x} - \dot{x_d} \tag{61}$$

For a second order system, a time-varying 'sliding' surface in the state-space is defined by the scalar equation:

$$s(x,t) = \left(\frac{d}{dt} + \lambda\right)^{n-1} \tilde{x} = 0 \tag{62}$$

where λ is a strictly positive constant. The sliding condition is referred to as keeping the scalar s at zero, and choosing a control law u such that when s is not zero:

$$\frac{1}{2}\frac{d}{dt}s^2 \leq -\eta\,|s| \tag{63}$$

The sliding condition means that the distance to the surface must decrease along system trajectories, implying that all system trajectories are constrained to point towards the sliding surface. The discontinuous control law is defined in Equations (64-66):

$$\hat{u}_x = -\ddot{x} + \ddot{x}_d - \lambda\dot{\tilde{x}} \tag{64}$$

$$k_x = \beta_x\eta + (\beta_x - 1)\,|\hat{u}| \tag{65}$$

$$u_x = \hat{b}_x^{-1}(\hat{u}_x - k_x sgn(s)) \tag{66}$$

where:

$$\hat{b}_x = \sqrt{b_{x,min}b_{x,max}} \tag{67}$$

$$\beta_x = \sqrt{\frac{b_{x,max}}{b_{x,min}}} \tag{68}$$

3.4 Simulating and Evaluating Illumination of Resident Space Objects

This section describes the methodology used to simulate a space-based mirror illuminating a resident space object (RSO) with reflected sunlight, along with the methodology used to evaluate how well a space-based sensor can image said object. Once scenarios are designed with specific orbits, the illumination of the RSO is simulated at each timestep. The visual magnitude metric is used to 'score' each scenario.

3.4.1 Augmenting Lighting Conditions On Orbit

The methodology for simulating augmented lighting conditions is modified from Canady and Allen's [2] method, in which a reflector spacecraft points sunlight towards low Earth orbits or onto the Earth surface. In this scenario, the reflector spacecraft is instead pointing sunlight towards another region of cislunar space. Scenarios were simulated utilizing MATLAB to generate propagated reflector, observer, and target orbits, associated relative position vectors, and the Sun position vector. A notional scenario is depicted in Figure 14, with the Sun, reflector spacecraft, observer spacecraft, and target shown. Radiant energy from the sun is reflected by a mirror spacecraft at an incident angle of γ towards a target of distance d.

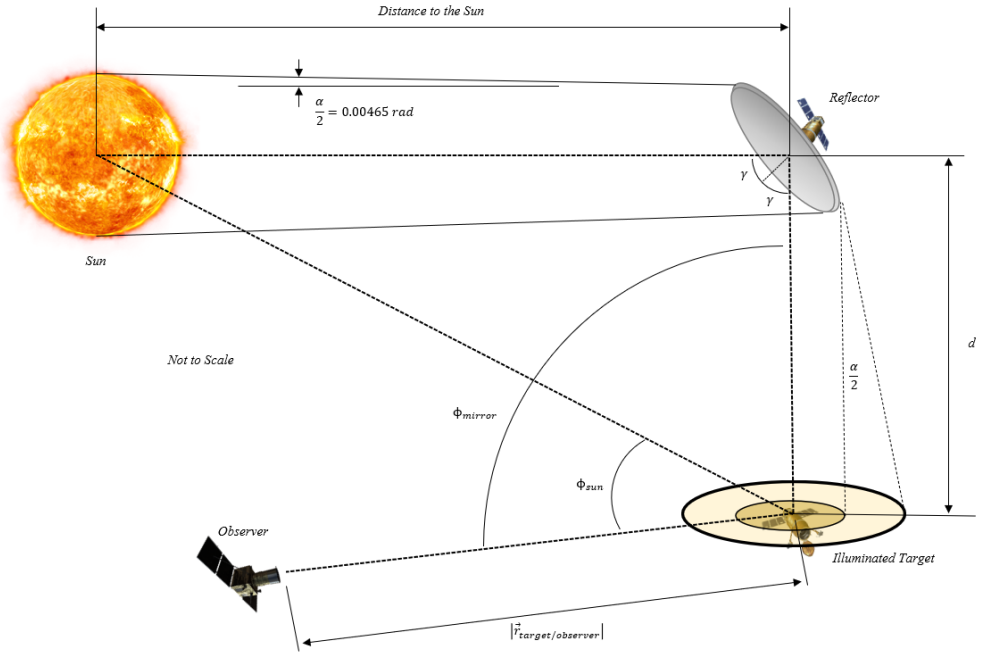

Figure 14: Sun, Reflector, Observer, and Target Geometry

Accounting for losses through reflector material, surface properties, and sunlight angle of incidence, the total energy reflected by the mirror is defined by Equation (69):

$$E = \eta\psi I_0 A_m \cos\gamma \tag{69}$$

where η is the mirror-surface coefficient of reflectivity, ψ is the mirror-surface flatness coefficient, I_0 is the solar constant (radiative flux), and A_m is the mirror area. Surface figure and reflectivity coefficients of 0.9 will be used for all scenarios, representative of aluminum membrane mirrors, a logical choice for these reflectors [2]. The radiative flux intensity is assumed to be 1358 W/m^2, representative of the Earth-Moon region [21].

The Sun is not a point source; light is not collimated as it arrives at the reflector surface. Therefore, ideal specular reflection is not possible. A radiative flux over a given area will not maintain its concentration when travelling over large distances following reflection. This divergence half-angle $\alpha/2$ creates an inverse square relationship between distance travelled d and radiative flux I. This is accounted for by:

$$I = \frac{\eta\psi I_0 A_m \cos\gamma}{\pi\left(d \cdot \tan\frac{\alpha}{2} + r_m\right)^2} \tag{70}$$

Equation (70) represents the irradiance at a desired target for a single mirror with a non-collimated light source. Further simplifying, the Sun-to-Target irradiance relationship can be represented as Equation (71), a dimensionless ratio that will be useful later on while calculating visual magnitude. Optical properties of the mirror used in this scenario are listed below in Table 4.

$$\frac{I}{I_0} = \frac{0.81 r_m^2 \cos\gamma}{\left(d \cdot \tan\frac{\alpha}{2} + r_m\right)^2} \tag{71}$$

Table 4: Mirror Optical Properties

Parameter	Value
η	0.9
ψ	0.9
I_0	1358 $\frac{W}{m^2}$
r_m	100 m
$\frac{\alpha}{2}$	0.00465 rad

3.4.2 Evaluating Illumination

Evaluation of an augmented illumination scenario will make use of the visual magnitude metric to quantify performance. Visual magnitude is a dimensionless quantity that describes the brightness of an object. It is adopted from Astronomy where it has been used in the study of stars. Krag developed a method to describe the visible magnitude of satellites in synchronous orbits [39] that has been used by Shell [40], Vendl [41], Thompson [42], and Wilmer [43][44]. The following is an adaption from previous research for the visual magnitude of RSO's illuminated by natural and/or reflected sunlight. Visual magnitude is calculated by, first, determining the solar phase angle at every point in time. The phase angle is calculated from Equation (72):

$$\phi_{Sun} = \arccos\left(\frac{\vec{r}_{Tar/Obs} \cdot \vec{r}_{Tar/Sun}}{r_{Tar/Obs} r_{Tar/Sun}}\right) \tag{72}$$

where $\vec{r}_{Tar/Obs}$ is the vector position of the target with respect to the observer satellite, and $\vec{r}_{Tar/Sun}$ is the vector position of the target with respect to the Sun. The mirror, or reflector, phase angle is calculated from Equation (73):

$$\phi_{Mirror} = \arccos\left(\frac{\vec{r}_{Tar/Obs} \cdot \vec{r}_{Tar/Reflector}}{r_{Tar/Obs} r_{Tar/Reflector}}\right) \tag{73}$$

where $\vec{r}_{Tar/Obs}$ is the vector position of the target with respect to the observer satellite, and $\vec{r}_{Tar/Reflector}$ is the vector position of the target with respect to the Reflector spacecraft. This derivation assumes that the reflector surface is located separately from the observer craft on a system of its own. When the reflector surface and observer satellite are collocated as one system, the mirror phase angle is zero.

In this analysis, the target is modeled as a sphere; therefore, the phase function, Ψ, becomes:

$$\Psi = \frac{2}{3}\frac{C_d}{\pi}(\sin\phi + (\pi - \phi)\cos\phi) \tag{74}$$

where C_d is the coefficient of diffuse reflection which is a function of the mean wavelength. The visual magnitude, M_v, is then calculated by:

$$M_v = -26.8 - 2.5\log_{10}\left(\frac{A}{r^2_{Tar/sat}}\Psi\right) \tag{75}$$

with A representing the surface area of the Target. Properties of the target used in this analysis are listed in Table 5.

Table 5: Target Optical Properties

Parameter	Value
A	15 m^2
C_d	0.2

The visual magnitude is, counter-intuitively, measured on a logarithmic scale in which lower numbers indicate brighter objects. A target is considered visible when it has a visual magnitude of $M_v \leq 18.5$.

To evaluate the visual magnitude of an RSO illuminated only by a reflector spacecraft Equation (75) is modified with an additional mirror-loss term, Equation (71), inside the log_{10} function:

$$M_v = -26.8 - 2.5 \log_{10} \left(\frac{I}{I_0} \frac{A}{r_{Tar/sat}^2} \Psi_{Mirror} \right) \tag{76}$$

To evaluate the visual magnitude of an RSO illuminated by only the Sun, Equation (77) is used:

$$M_v = -26.8 - 2.5 \log_{10} \left(\frac{A}{r_{Tar/sat}^2} \Psi_{Sun} \right) \tag{77}$$

The Earth and Moon's albedo effects are not considered in this research for illumination purposes. However, they are important to consider as exclusionary regions between the observer and the target. If the target's phase angle between the Sun, Earth, or Moon and the observer is small enough, the target becomes indistinguishable because of the glare. To account this for, planetary exclusion angles are included in this analysis, and the visual magnitude is auto-adjusted to a value of 35. See Table 6 below for the exclusion angles used.

Table 6: Planetary Exclusion Angles

Planetary Body	Exclusion Angle (deg)
Sun	30
Earth	15
Moon	6

3.5 Summary

This chapter presented methodology employed in the space-based mirror CONOPs investigation. Topics included the Circular Restricted Three-Body Problem, meth-

ods of periodic orbit design, methods of linear and nonlinear control for trajectory tracking, and the simulation and evaluation of mirror illumination conditions. These methodologies are used to design scenarios in which the effectiveness of space-based mirrors to illuminate resident space objects is quantified and evaluated. The ability to illuminate a resident space object at or below a visual magnitude threshold for remote sensing is the critical performance factor.

IV. CONOPs Investigation Analysis and Results

This chapter uses computer simulation (MATLAB) and the methodologies presented in Chapter III to develop periodic orbits, create scenarios made up of a target, reflector, and observer spacecraft, evaluate illumination of the target, and control spacecraft to a desired orbit. The overarching goals of this chapter include demonstrating non-collocated versus collocated system performance, providing insight into cislunar proximity orbits inside Lagrange point families, and demonstrating an observer spacecraft's ability to track a desired trajectory within an acceptable error margin.

4.1 Results and Analysis of Non-collocated versus Collocated Reflector and Observer

This section provides the results for the augmented illumination of resident space objects using space-based reflectors. Two scenarios were researched: separate observer and reflector spacecraft (non-collocated) and combined (collocated) observer/reflector spacecraft. In both scenarios, the illumination from natural sunlight and reflected sunlight are presented for comparison. Scenarios were evaluated for at least three full orbital periods, equal to a minimum scenario time of approximately 30 days. Data is provided in tables representing percentage of scenario time that the target is considered visible, i.e. under a visual magnitude of 18.5, and plots showing the sunlight/reflected light visual magnitude trends over entire scenarios. Table 7 below collects the initial conditions used as starting points for investigation of an orbit family.

Table 7: Initial Conditions for Non-collocated and Collocated Scenarios (DU and DU/TU)

Orbit Family	x_0	y_0	z_0	$\dot{x}_0$	$\dot{y}_0$	$\dot{z}_0$
L_1 Lyapunov	0.7689	0	0	0	0.4813	0
L_1 Halo	0.8355	0	0.1424	0	0.2527	0
L_2 Lyapunov	1.2167	0	0	0	-0.4164	0
L_2 Halo	1.0754	0	0.2022	0	-0.1926	0
L_4 Planar	0.6015	$\frac{\sqrt{3}}{2}$	0	0.0685	-0.1069	0
GEO	0.1097	0	0	0	3.0009	0

4.1.1 Non-collocated Reflector

Table 8 summarizes the results simulating a non-collocated observer and reflector, in which 14 GEO, L_1, L_2, and L_4 orbit combinations were evaluated. Each scenario was evaluated for at least three complete orbital periods. The first three columns in Table 8 are the orbit locations of the target, observer, and reflector. The fourth column labeled "Natural" is the percentage of time that the target meets the detection criteria due to the natural illumination from the sun without any need for the reflector. The fifth and final column labeled "Reflector" is the percentage of time that the target meets the detection criteria due to the reflector's illumination. The illumination from sunlight and the reflector are analyzed separately and are not considered to work together.

Table 8: Percentage of Scenario Meeting Visual Magnitude Threshold: Non-collocated Reflector

Target	Observer	Reflector	Natural	Reflector
GEO	100 km NMC	L_1 Lyapunov	88.7	0.0
GEO	100 km NMC	L_1 Halo	88.7	0.0
L_1 Lyapunov	L_1 Lyapunov	L_1 Halo	87.4	2.4
L_1 Lyapunov	L_1 Lyapunov	L_2 Lyapunov	87.5	0.0
L_1 Lyapunov	L_1 Lyapunov	L_2 Halo	87.5	0.0
L_1 Lyapunov	L_1 Lyapunov	L_4 Planar	87.5	0.0
L_1 Halo	L_1 Halo	L_1 Lyapunov	97.4	0.0
L_1 Halo	L_1 Halo	L_2 Lyapunov	97.4	0.0
L_1 Halo	L_1 Halo	L_2 Halo	98.5	0.0
L_1 Halo	L_1 Halo	L_4 Planar	97.4	0.0
L_2 Halo	L_2 Halo	L_1 Lyapunov	91.0	0.0
L_2 Halo	L_2 Halo	L_1 Halo	91.0	0.0
L_2 Halo	L_2 Halo	L_2 Lyapunov	91.0	0.0
L_2 Halo	L_2 Halo	L_4 Planar	91.0	0.0

Table 8 shows only one non-collocated combination of observer and reflector produced an environment that the reflector spacecraft could provide sufficient irradiance for detection. This scenario is when the target and observer are in periodic L_1 Lyapunov orbits, and the reflector is in a periodic L_1 Halo orbit. Figure 15 shows the visual magnitude of the target throughout the scenario. Lower visual magnitudes indicate higher illumination with any value below the red-dotted line indicating detection. The black lines are the visual magnitude caused from natural illumination, whereas the blue lines are those caused from the reflector illumination. In only 2.4% of the scenario did the illumination from the reflector reach the detection criteria.

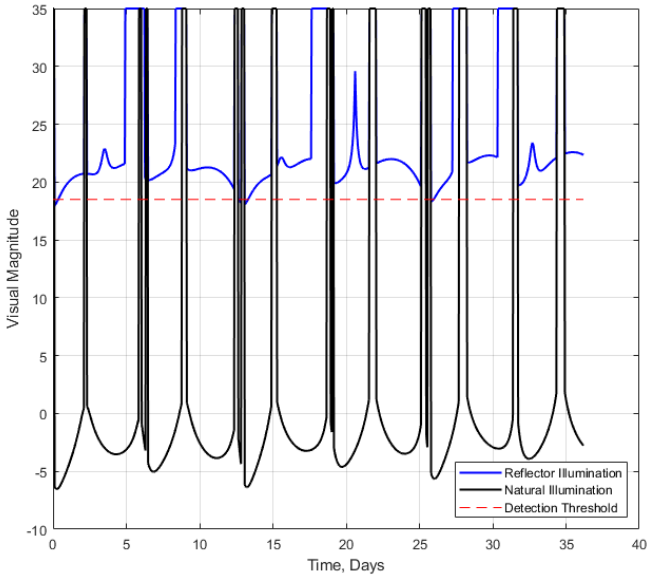

Figure 15: Target and Observer placed in the L_1 Lyapunov family and Reflector placed in the L_1 Halo family

4.1.2 Collocated Reflector

The collocated reflectors incorporate more nuance into the effectiveness of the reflector's illumination. Frequently, natural illumination may cast a shadow on the far side of the target RSO creating a 'dark side' from which the target may be discernible relative to background space based on visual magnitude, but an observer may not be able to image, discern edges, features, etc. For example, the image of Atlantis (Figure 16) below shows how even though the shuttle may be brightly lit and have a low visual magnitude number, features on the left side may be obscured by shadow.

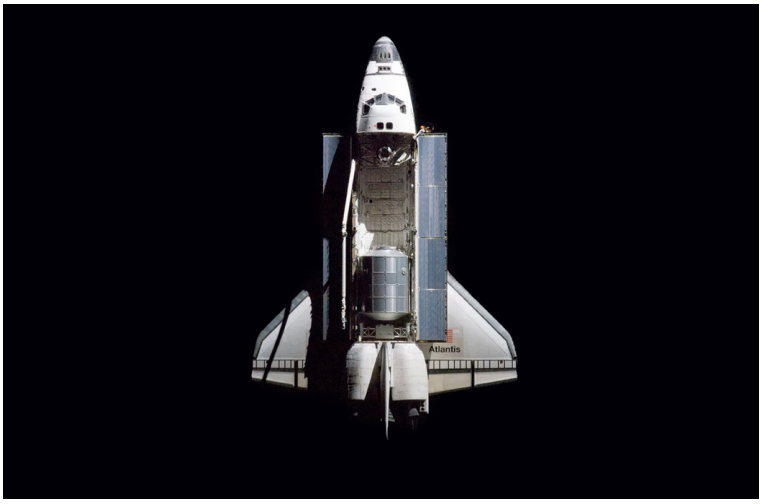

Figure 16: Shadows on the Space Shuttle Atlantis near the Payload Bay Doors, adapted from [5]

The collocated reflectors incorporate an adjustment to the natural sunlight illumination to remove portions of the natural illumination when the observer/reflector is 'behind' the target relative to the sun, corresponding to a sun phase angle of greater than 90 deg. This is depicted in Figure 17. Both the raw and adjusted data for both natural and reflector illumination is included in the present study. The critical metric is "Adjusted Reflector", representing the percentage of each scenario in which the observer/reflector can effectively illuminate the target when off by 90 deg. or more in phase angle from the sun ('dark side').

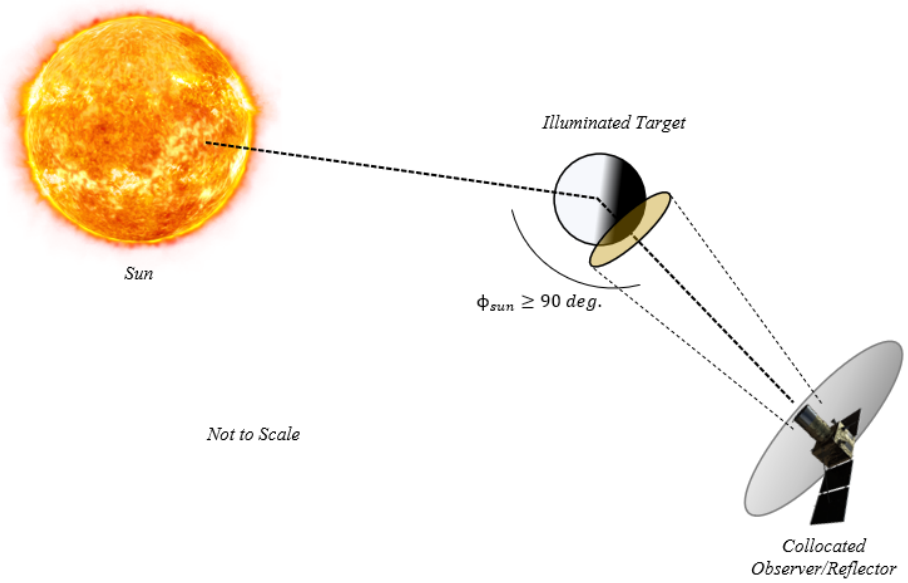

Figure 17: Reflector Illumination on the 'Dark Side' of the Target

Table 9 summarizes the results simulating a collocated observer and reflector, in which five orbits (L_1 and L_2 Lyapunov and Halo and L_4 Planar) were evaluated. The first column in Table 9 shows the orbit locations of the target and observer/reflector. The second column labeled "Natural" is the percentage of time that the target meets the detection criteria due to the natural illumination from the sun without any need for the reflector. The third column labeled "Adjusted Natural" is the percentage of time that the target meets the detection criteria due to natural illumination, but removes any regions where the sun phase angle is greater than 90 deg. as discussed above and demonstrated in Figure 17. The fourth column labeled "Reflector" is the percentage of time that the target meets the detection criteria due to the reflector's illumination. The fifth and final column labeled "Adjusted Reflector" is the critical metric discussed above.

Table 9: Percentage Meeting Visual Magnitude Threshold: Collocated Reflector

Target/Observer/Reflector	Natural	Adjusted Natural	Reflector	Adjusted Reflector
L_1 Lyapunov	87.5	50.8	55.0	36.7
L_1 Halo	97.4	39.4	82.5	57.9
L_2 Lyapunov	82.7	46.7	25.7	18.9
L_2 Halo	91.0	51.1	55.3	32.2
L_4 Planar	78.1	46.1	48.0	32.0

Figures 18, 19, 20, 21, and 22 show the visual magnitude over the five scenarios. Lower visual magnitude values indicate higher illumination with any value below the red-dotted line indicating a detection has occurred. The black lines are the visual magnitude caused from natural illumination, whereas the blue lines are those caused from the reflector illumination. The left plot in each of the figures is the raw illumination, while the right plot is the adjusted illumination to remove portions of natural sunlight illumination when the observer/reflector is "behind" the target relative to the sun creating a "dark side" as discussed above. This corresponds to a sun phase angle of greater than 90 degrees.

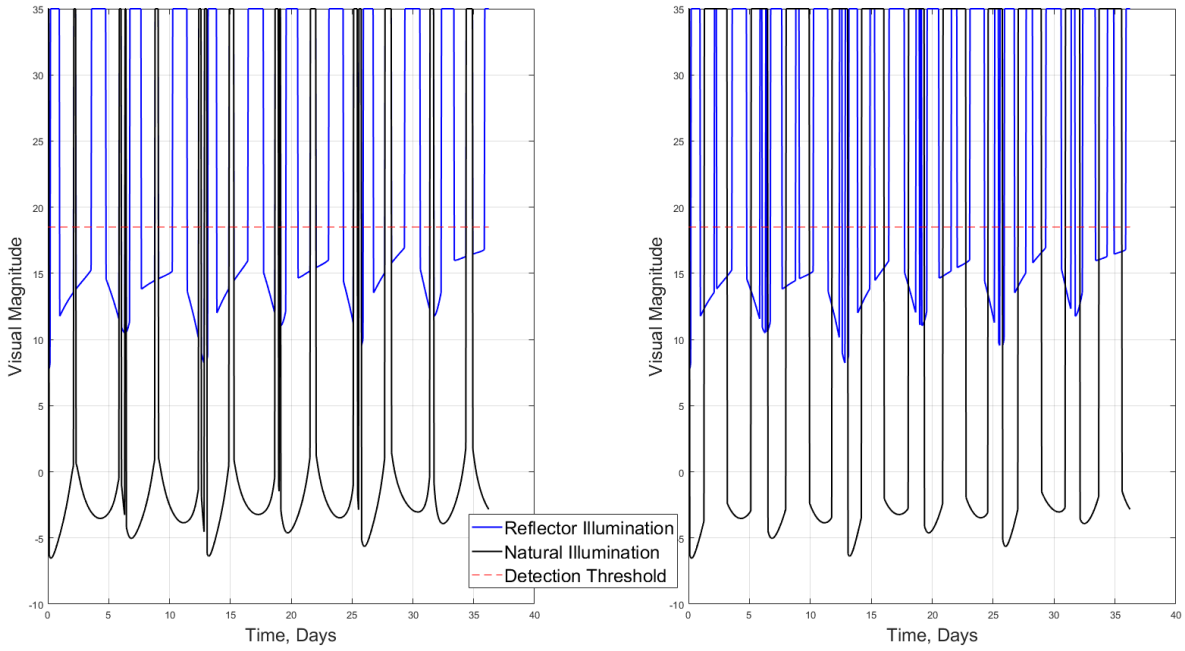

Figure 18: Target and collocated Observer/Reflector placed in the L_1 Lyapunov family

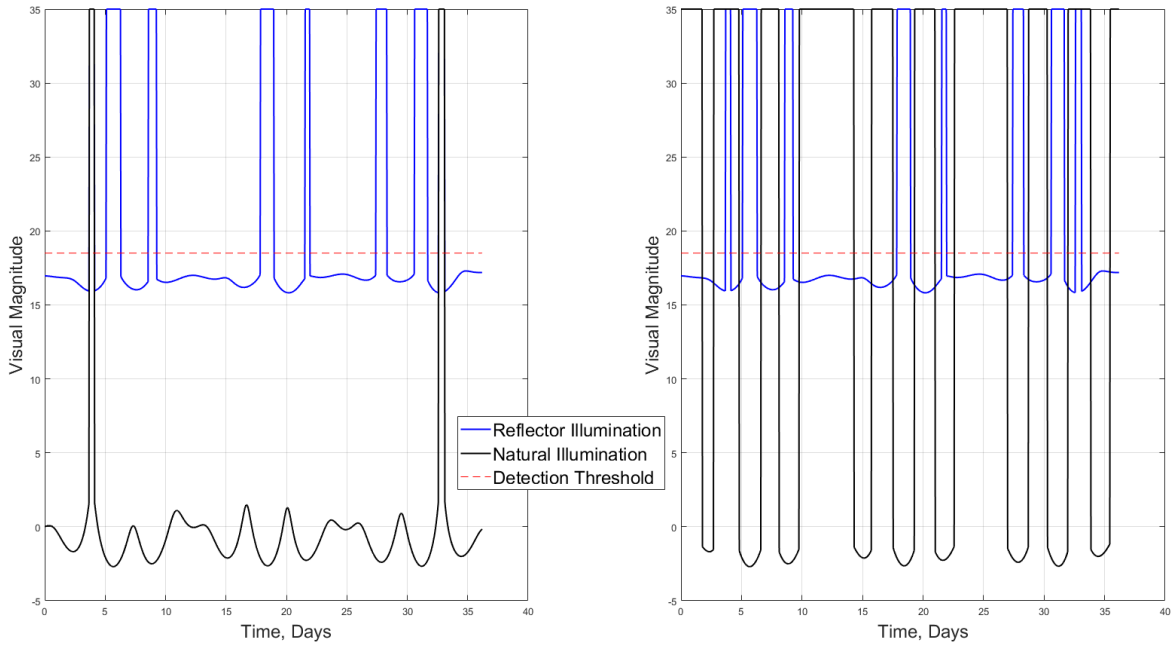

Figure 19: Target and collocated Observer/Reflector placed in the L_1 Halo family

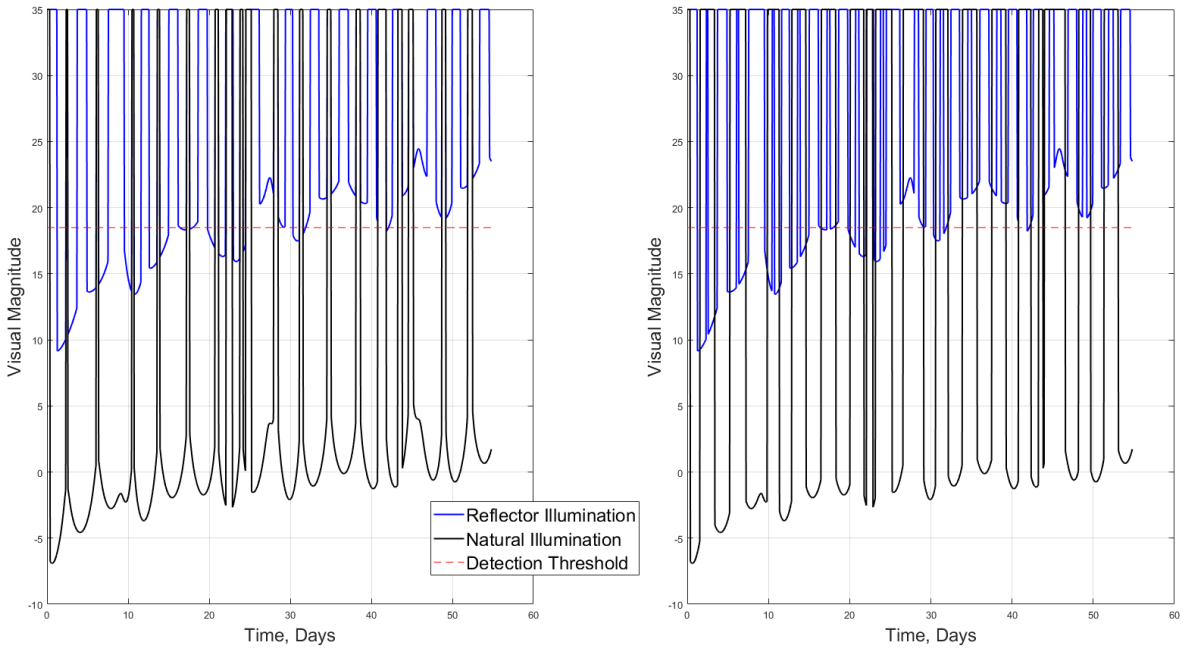

Figure 20: Target and collocated Observer/Reflector placed in the L_2 Lyapunov family

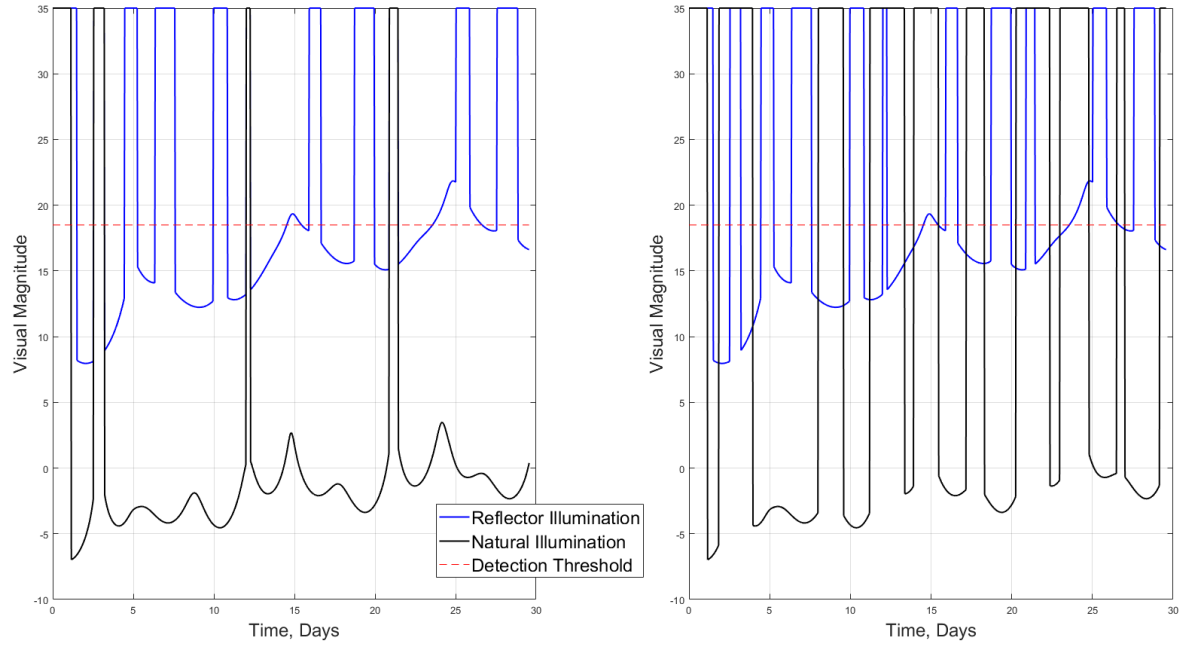

Figure 21: Target and collocated Observer/Reflector placed in the L_2 Halo family

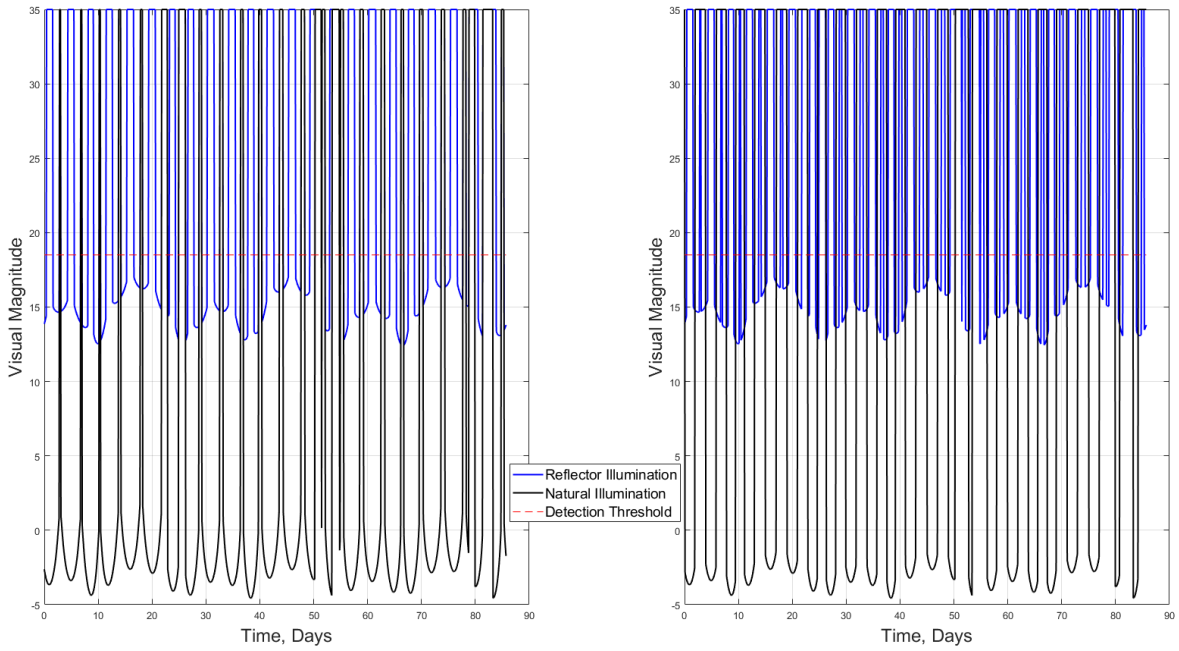

Figure 22: Target and collocated Observer/Reflector placed in the L_4 Planar family

4.1.3 Analysis of Non-collocated vs. Collocated Systems

The difference in detection rates between the non-collocated and collocated reflectors is stark. The non-collocated reflector offered negligible or no improvement in detection rate in any of the 14 scenarios tests, whereas the collocated reflectors offered significant improvement ranging from 18.9% to 57.9% as seen from the "Adjusted Reflector" metric. The large distance in the non-collocated scenarios make the illumination an ineffective prospect. However, the collocated scenarios demonstrate that illumination can greatly improve detection rates when distances are dramatically decreased.

The L_1 collocated reflectors seemed to perform more effectively than their collocated L_2 analogues with detection rates ranging from $36.6 - 57.9\%$ compared to $18.9 - 32.2\%$. The L_1 periodic orbits have a smaller physical size than the L_2 periodic orbits. To orbit at L_2, a trajectory must have significantly more energy than at

L_1. This is quantified by the different Jacobi constants at L_1 versus L_2, discussed in Section 3.1 and depicted in Figure 8. This further confirms that the large distances is a significant contributor to the effectiveness of the reflector illumination.

The visual magnitude for the L_2 families (especially Lyapunov) is noticeably decreasing as the scenario is progressing as seen in Figures 20 and 21. To investigate this trend, the observer/reflector to target relative position over the entire scenario is plotted in Figures 23 and 24. These plots produce interesting shapes that give insight into how the relative states change over the course of multiple orbital periods.

Since the observer/reflector orbit was designed via parameter continuation methods to be in proximity of the target's orbit, the periods do not match. Therefore, the two orbits do not meet what is called the energy matching condition [32]. When an NMC orbit is designed around a GEO target using two-body dynamics (specifically, the Hill-Clohessy-Wiltshire Equations), the energy matching condition is met, and the orbits can continue in a repeating relative trajectory relative to one another for any scenario length. This assumes that perturbative and third-body effects are neglected. Since the energy matching condition is not met in this scenario, the relative position grows throughout the scenario resulting in a reduction in visual magnitude as the distance in relative position grows.

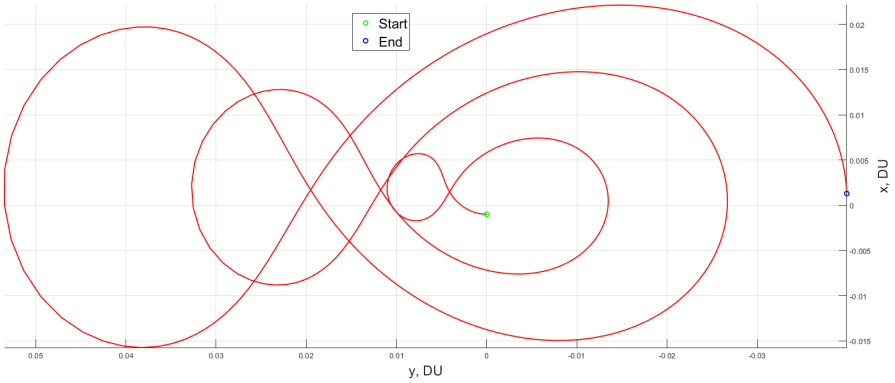

Figure 23: Relative position of Target with respect to Observer/Reflector demonstrating orbit divergence in L_2 Lyapunov families (x-y plane viewed)

Figure 24: Relative position of Target with respect to Observer/Reflector demonstrating orbit divergence in L_2 Halo families(left: y-z plane viewed, right: x-z plane viewed)

The phenomenon of non-energy matching conditions in cislunar proximity orbits is explored further in Figures 25 and 26. The L_2 Lyapunov and Halo scenarios from

Figures 20 and 21 are propagated for ten periods rather than three. Total scenario time extends to approximately 180 and 100 days for the L_2 Lyapunov and Halo orbit scenarios, respectively. These extended scenarios demonstrate that over time, a slight difference in orbital period has a pronounced effect on illumination performance.

Table 10: Percentage Meeting Visual Magnitude Threshold: Extended Scenarios

Target/Observer/Reflector	Natural	Adjusted Natural	Reflector	Adjusted Reflector
L_2 Lyapunov	80.2	44.5	4.1	2.8
L_2 Halo	95.0	50.1	22.8	13.5

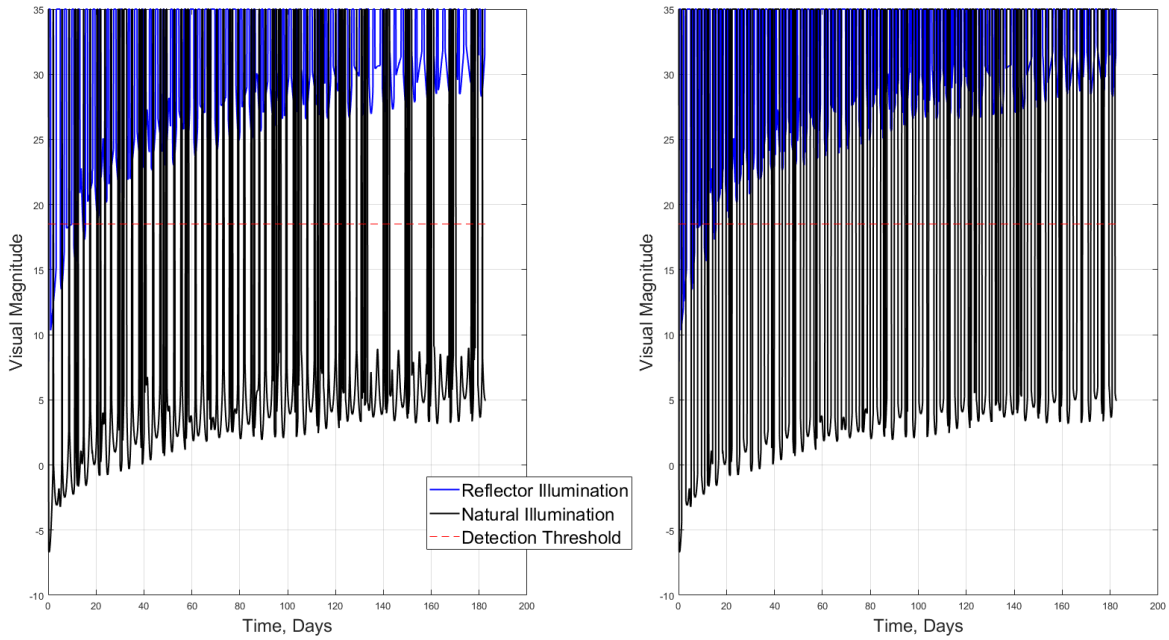

Figure 25: Extended L_2 Lyapunov Scenario

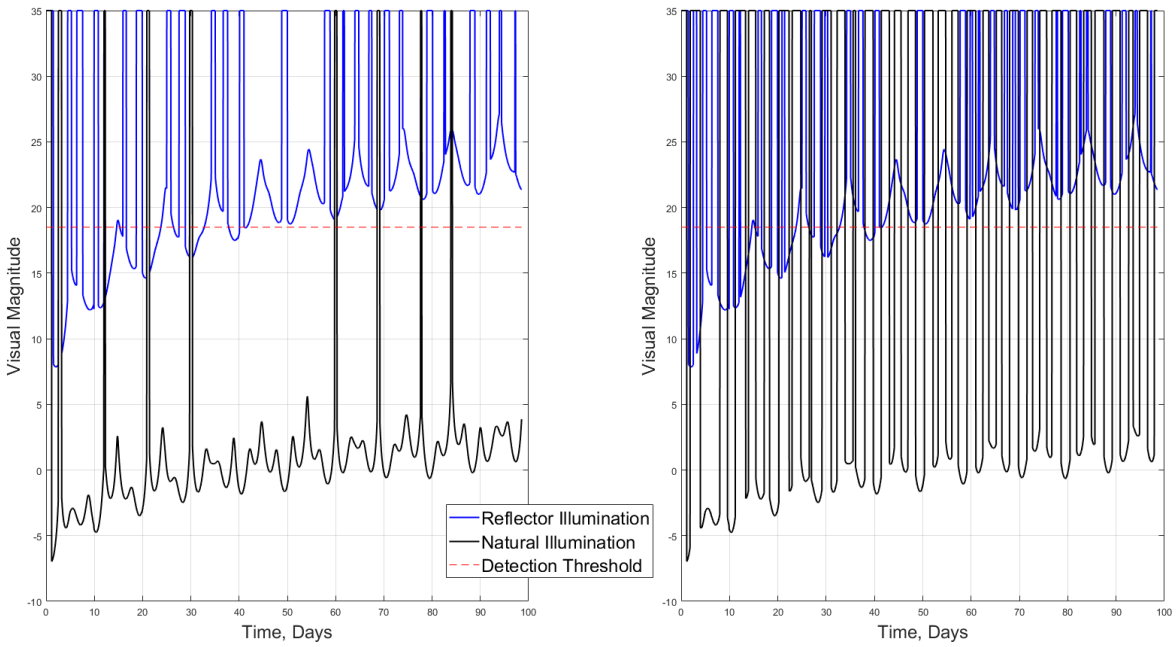

Figure 26: Extended L_2 Halo Scenario

4.2 Results and Analysis of Parameter Continuation

This section demonstrates the impact of orbital spacing on the effectiveness of illumination while a collocated reflector/observer spacecraft is operating in proximity of a target. Proximity is herein defined as a collocated reflector/observer spacecraft operating in the same orbit family as the target that is one or multiple number of parameter steps away. The parameter step used in the following scenarios is 0.5 x 10^{-3} DU $\cong$ 190 km. The scenarios start with a target orbit's initial conditions (Table 11) and use the parameter continuation method described in Section 3.2 to generate a family of nearby orbits within the same family. Each of these in-family reflector/observer orbits is quantified via its ability to illuminate the target as described in Section 3.4. The left side of Figures 27-35 shows the evolution of the reflector/observer orbit as it moves through the family in either direction. The dashed black line in each of these plots is the target orbit, and does not change throughout the scenar-

ios. The right side of Figures 27-35 shows the trend in illumination capability. This is quantified as the percentage of time in each scenario that the reflector/observer can illuminate and discern the target with a visual magnitude $M_v \leq 18.5$. Each data point along the x-axis of these plots contains similar calculations to those reported in Tables 8-10. Only reflector illumination is considered, not the Sun or albedo effect. The data in Figures 27-35 contain two trends: the blue line is the unadjusted visual magnitude data and the black line is the phase angle adjusted visual magnitude data. This data adjustment was discussed in 4.1.2. Table 11 below collects the initial conditions for each orbit family produced. These also represent the target orbit initial state vectors and were adapted from [26].

Table 11: Initial Conditions for Orbit Family Scenarios (DU and DU/TU)

Orbit Family	x_0	y_0	z_0	$\dot{x}_0$	$\dot{y}_0$	$\dot{z}_0$
L_1 Lyapunov	0.8189	0	0	0	0.1750	0
L_1 Halo	0.8260	0	0.0824	0	0.1964	0
L_2 Lyapunov	1.2167	0	0	0	-0.4164	0
L_2 Halo	1.0754	0	0.2022	0	-0.1926	0
L_4 Planar	0.6015	$\frac{\sqrt{3}}{2}$	0	0.0685	-0.1069	0

4.2.1 L_1 Lyapunov Family

The L_1 Lyapunov family displays similar behavior in the positive and negative directions, evident in Figures 27 and 28. However, the negative direction (towards L_1, a smaller orbit) begins with better performance by approx. 10%. Both directions of the family trend downwards in performance due to the non-energy matching condition becoming more impactful as orbital periods drift apart. By the time the reflector/observer is approx. 1000 km from the target orbit in the positive direction and approximately 1400 km in the negative direction, there is $< 10\%$ capability.

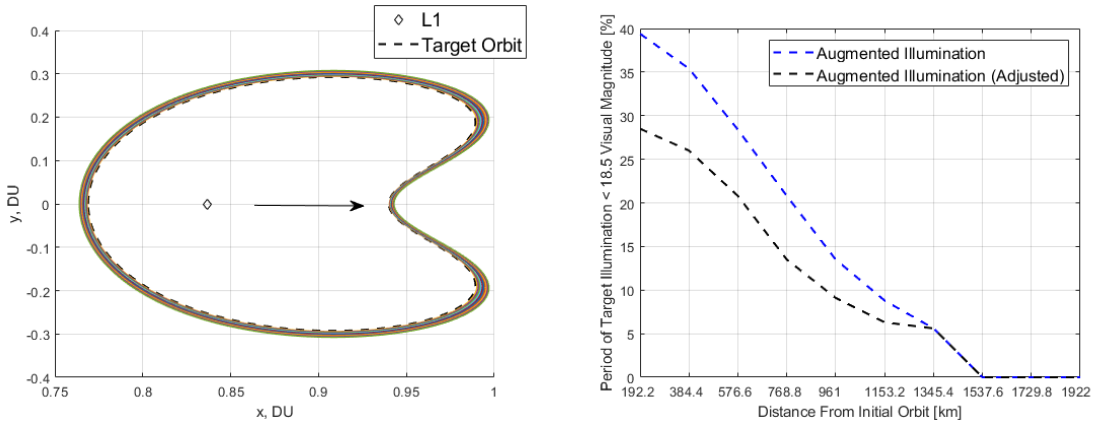

Figure 27: Positive direction through L_1 Lyapunov family

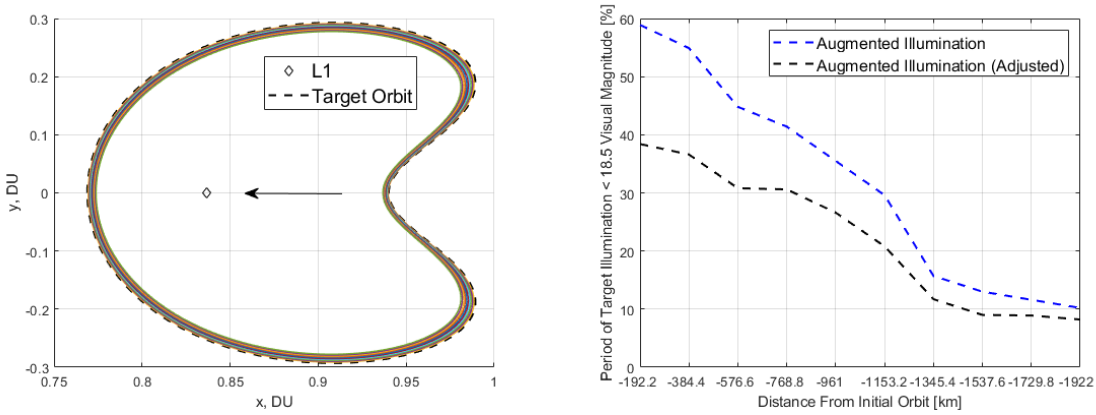

Figure 28: Negative direction through L_1 Lyapunov family

4.2.2 L_1 Halo Family

The L_1 Halo family shows an interesting difference between the positive and negative family directions. The unadjusted illumination trends similarly, dropping off once the reflector/observer is approximately 800-900 km from the target. However, the phase angle adjusted illumination behaves drastically different depending on the direction of family propagation in Figures 29 and 30. Moving in the negative direction (towards L_1), the reflector/observer never has opportunities more than 10% of the scenario time to illuminate the dark side of the target. This is likely due to the

geometry of the Halo orbits, where the Sun vector is located, orbital periods relative to the synodic frame rotation rate, and the starting location of both spacecraft in the scenario. This suggests that flying in proximity of a target in an L_1 Halo orbit, it may be advantageous to occupy a larger orbit inside the family rather than a smaller one.

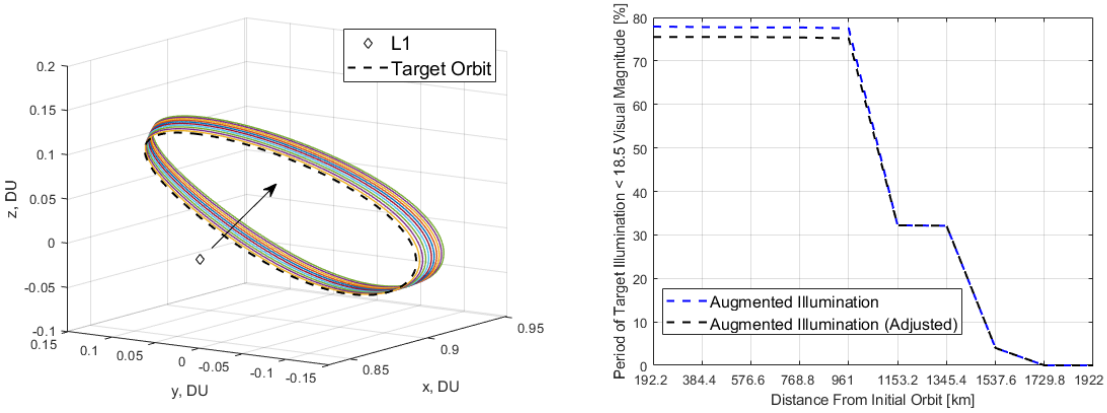

Figure 29: Positive direction through L_1 Halo family

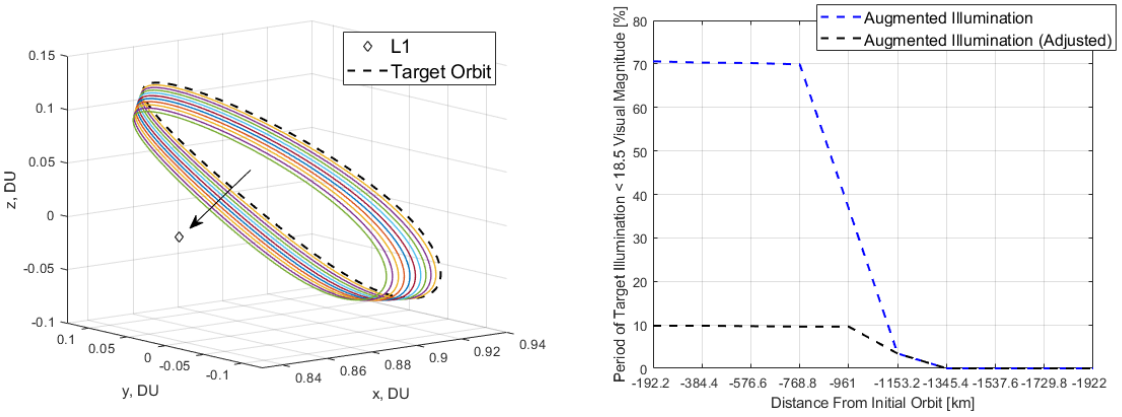

Figure 30: Negative direction through L_1 Halo family

4.2.3 L_2 Lyapunov Family

The L_2 Lyapunov family behaves in a similar fashion to the L_1 Lyapunov family discussed above. Figures 31 and 32 both show the family trend downwards in perfor-

mance due to the non-energy matching condition becoming more impactful as orbital periods drift apart. Around approximately 1300 km, the L_2 Lyapunov family loses nearly all ability to illuminate the target.

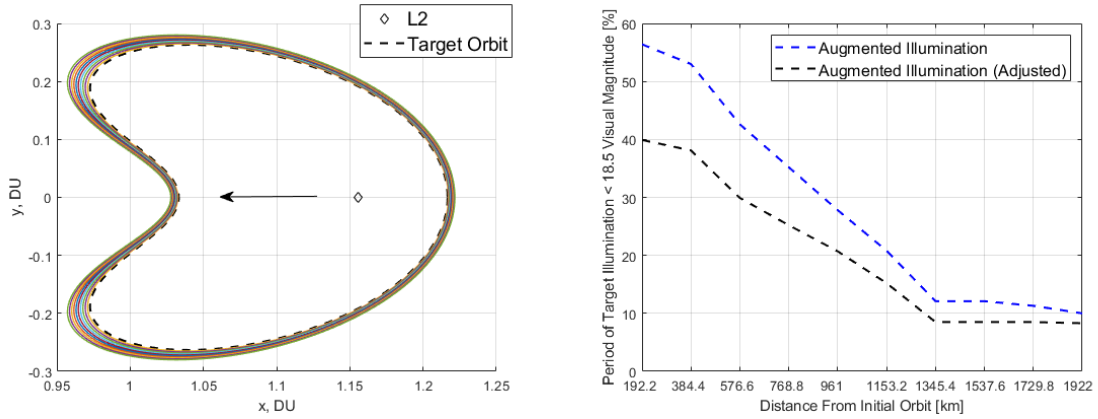

Figure 31: Positive direction through L_2 Lyapunov family

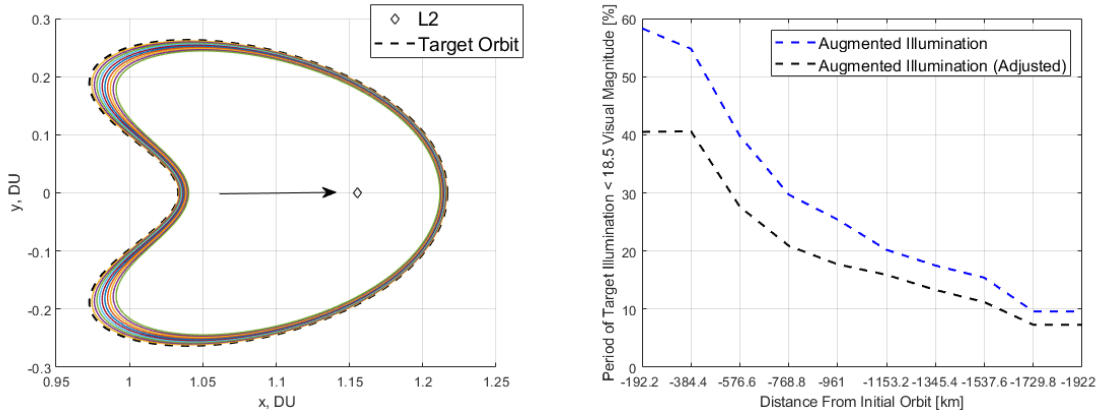

Figure 32: Negative direction through L_2 Lyapunov family

4.2.4 L_2 Halo Family

The L_2 Halo family appears to display the same behavior as the L_1 Halo family, but in the positive direction instead of negative. It is important to note here that "positive" in this case means positive x-direction in the synodic frame. At L_2, this

is towards the Lagrange point rather than away from it, like at L_1. With this consideration, it is clear that L_1 and L_2 Halos seem to behave similarly relative to their respective Lagrange points. It is suspected that differences in the L_2 Halo family could also be due to the exclusion angles applied for the Moon, because L_2 is on the far side.

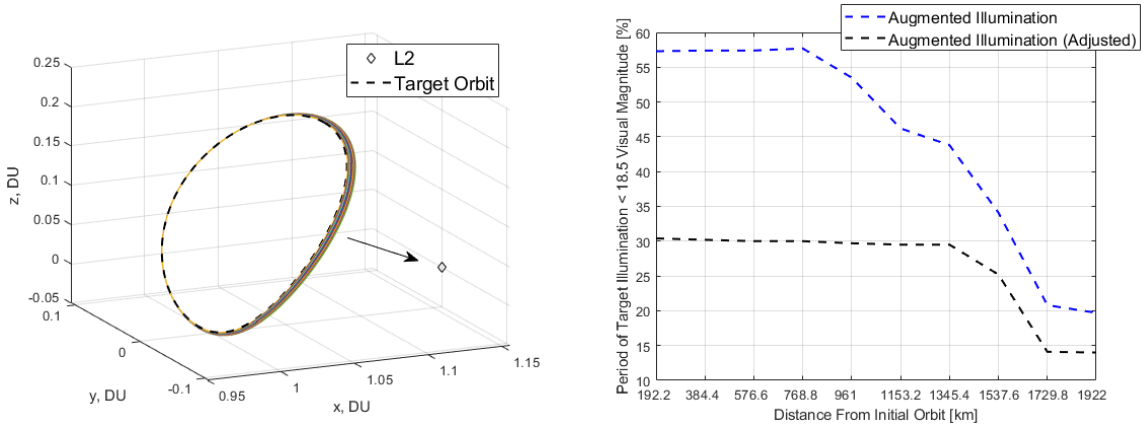

Figure 33: Positive direction through L_2 Halo family

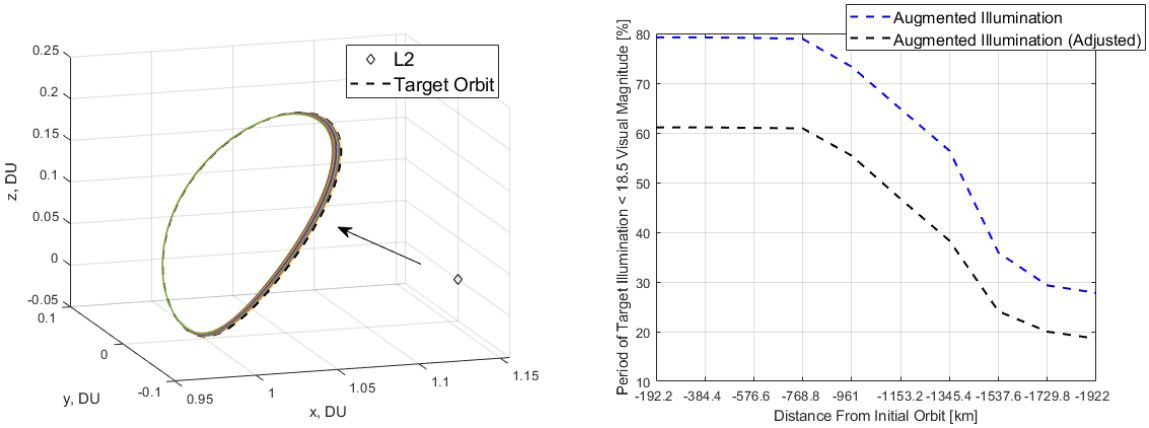

Figure 34: Negative direction through L_2 Halo family

4.2.5 L_4 Planar Family

As discussed in Section 3.2, the L_4 family is propagated using a different parameter continuation method than L_1 and L_2. Because of this, only one direction of

propagation was studied in this research: stepping away from the target orbit in a positive direction. The L_4 Planar family changes shape dramatically with each step through the family. Note that the "distance from initial orbit" in the right plot of Figure 35 is scaled differently than plots for the L_1 and L_2 points. This is because the pseudo-arclength parameter continuation method is used at L_4.

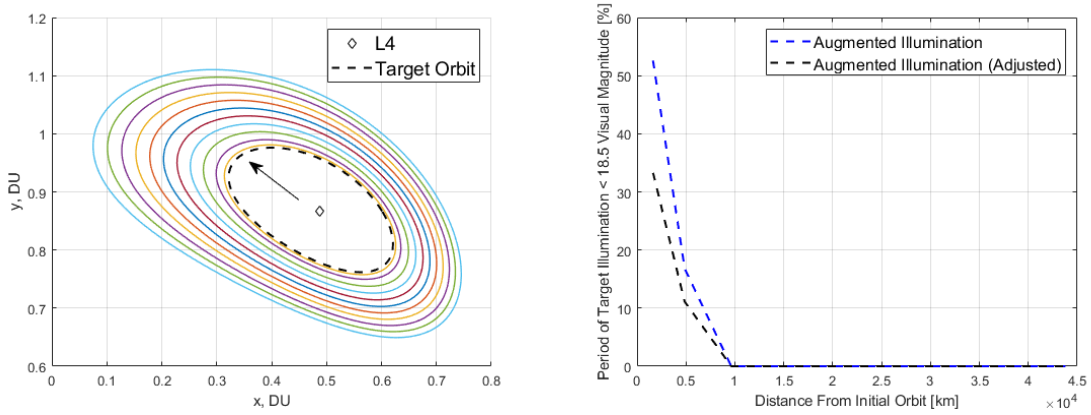

Figure 35: Positive direction through L_4 Planar family

A closer look at the trend in Figure 35 is shown in Figure 36 below. A data point is added at $\approx$ 384 km from the target orbit for comparison previous plots. Upon inspection, it seems there is workable area for illumination that steeply drops off after approximately 2000 km from the target. The L_4 planar family evolves differently than families at L_1 and L_2. Steps through the family impact x-axis initial position but also change $\dot{x}_0$ and $\dot{y}_0$, increasing the energy of the orbits.

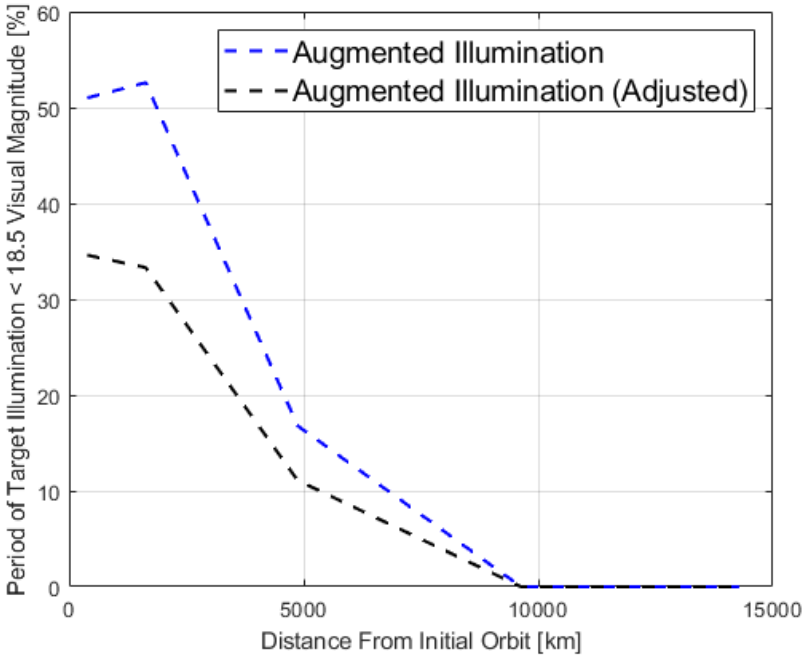

Figure 36: Closeup view of positive direction through L_4 Planar family

4.3 Results and Analysis of LQR and Sliding Mode Control

After designing an LQR controller to track linear orbits in the CR3BP, it was applied to orbits at L_1 and L_2 representing Lyapunov orbits, and a linear orbit at L_4 representing a Planar orbit. The SMC controller was applied to a linear orbit representing an L_1 Lyapunov orbit. The purpose of this section is to demonstrate the capability to track a desired orbit, such that it is realistic to presume the capability to operate in the proximity orbits described in Section 3.2 without endangering the reflector/observer or the target spacecraft. Figures 37, 39, 41, and 43 display the desired orbital track and the actual motion controlled by LQR/SMC. The red dotted lines show the desired linear orbit representing a Lyapunov (L_1 and L_2) or Planar (L_4) orbit and the blue line represents the motion of the LQR/SMC-controlled spacecraft subject to three-body dynamics. The control effort required to perform these tracks

is displayed in Figures 38, 40, 42, and 44 for x-axis (left plot) and y-axis (right plot). Figure 44 has two additional plots depicting location relative to the sliding surface condition in the x- and y-axes.

4.3.1 Linear Quadratic Regulator Control at L_1, L_2, and L_4

LQR control at L_1 was tested for ten orbital periods, beginning with an initial offset of of $0.1\xi_0$ outside the desired orbit. Figure 37 demonstrates the controllers ability to find the desired orbit and track it closely in approximately one-half orbital period. There is a clear immediate spike in the x-axis control effort of Figure 38 to move onto the desired orbit. Following this spike, the controller settles into the periodic nature of the orbit track, evidenced by sinusoidal motion of control effort. This represents direction changes in orbital motion, from + x-direction to - x-direction for example. The effort required to maintain this orbital track agrees with the research of Wie [35] within an order of magnitude. The relationship between time to the desired track and control effort expended is a relationship between the Q and R weighting matrices and their respective α and β tuning parameters. Both α and β were tuned to unity for all control simulations.

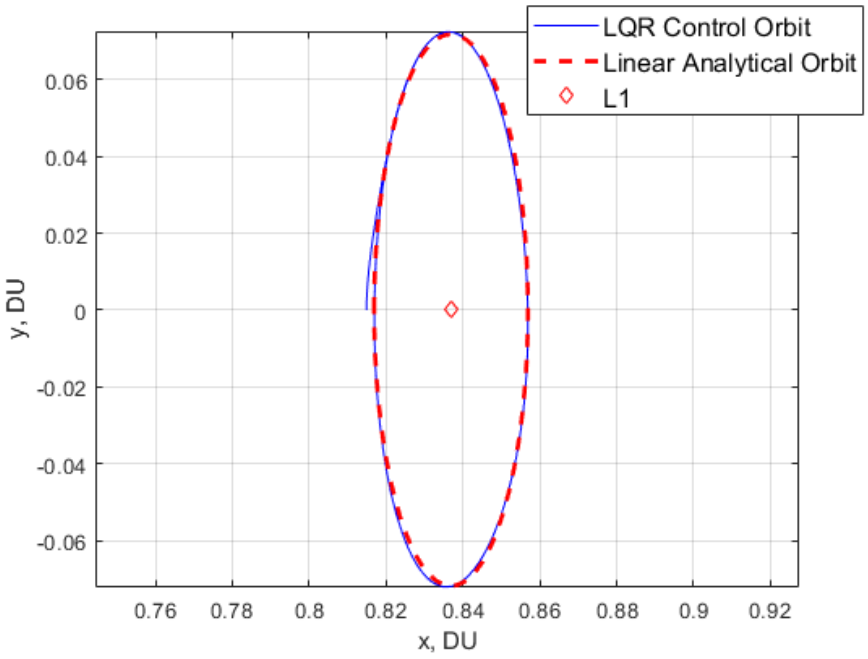

Figure 37: Successfully tracking the L_1 orbit using LQR

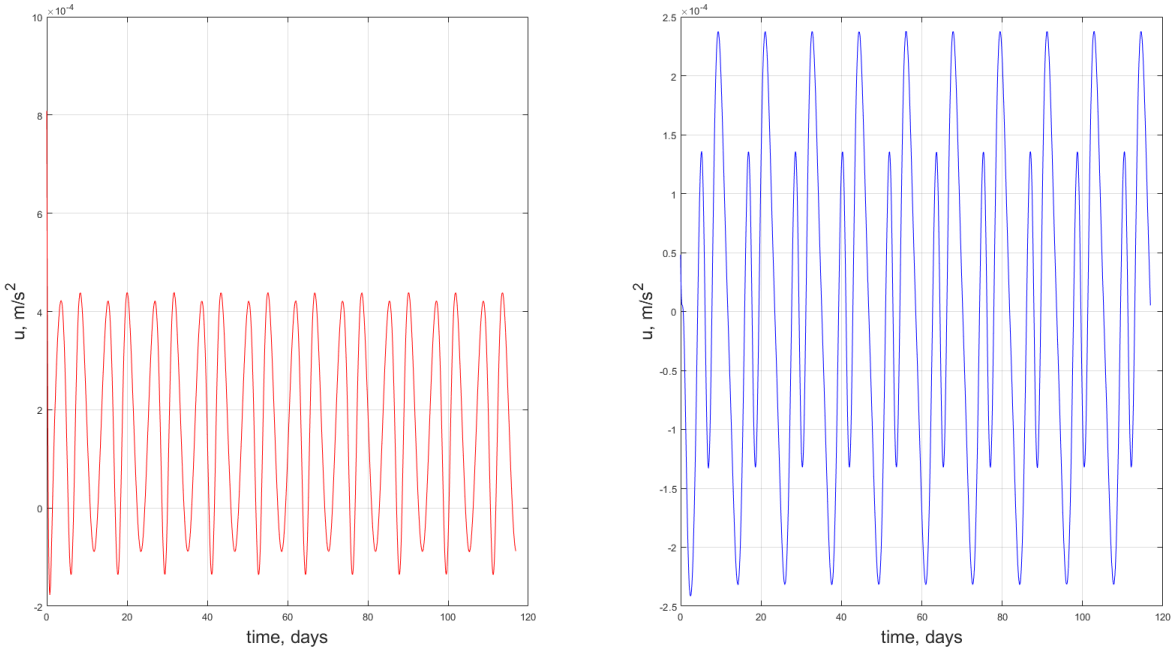

Figure 38: Control effort required to track the L_1 orbit using LQR

Using the LQR to control to a representative L_2 orbit is demonstrated for ten orbital periods in Figures 39 and 40. Although the Lyapunov-type orbit at L_2 in this case is significantly larger than at L_1, the controller behaves similarly, obtaining a good track in approximately one-half orbital period. Once again, the controller settles into a sinusoidal-like motion while tracking the linear orbit.

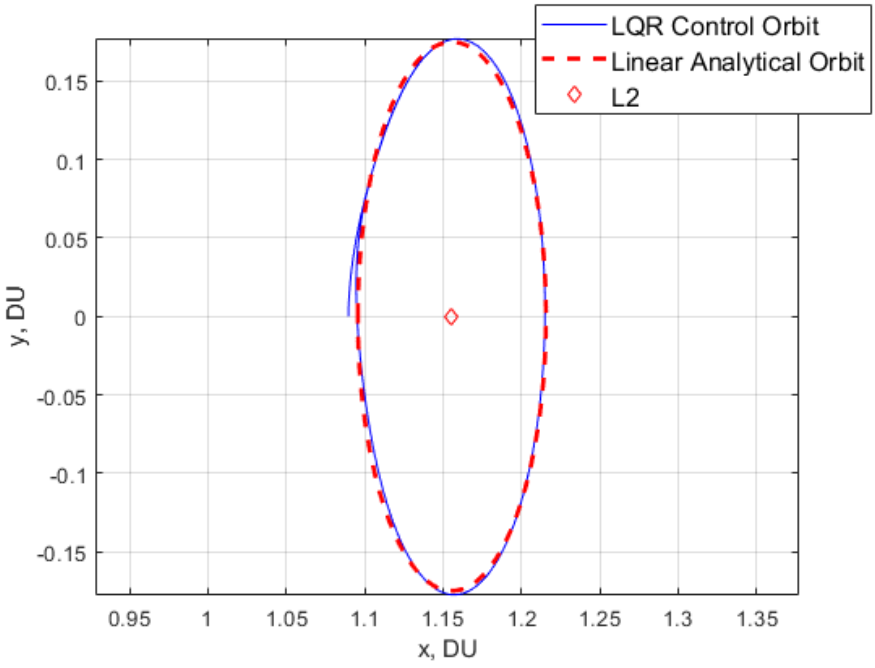

Figure 39: Successfully tracking the L_2 orbit using LQR

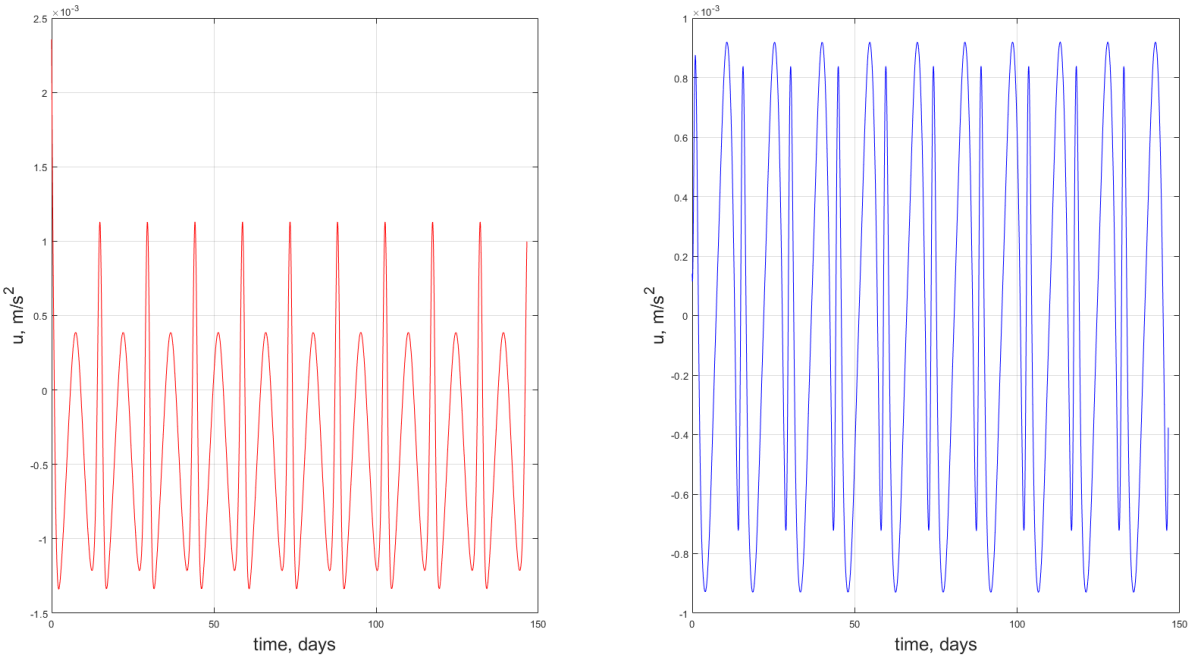

Figure 40: Control effort required to track the L_2 orbit using LQR

The LQR controller performed at a linear L_4 orbit much the same as L_1 and L_2. The controller corrected for the initial offset from the desired track. Both x- and y-axis control effort agree with LQR control documented in literature [35].

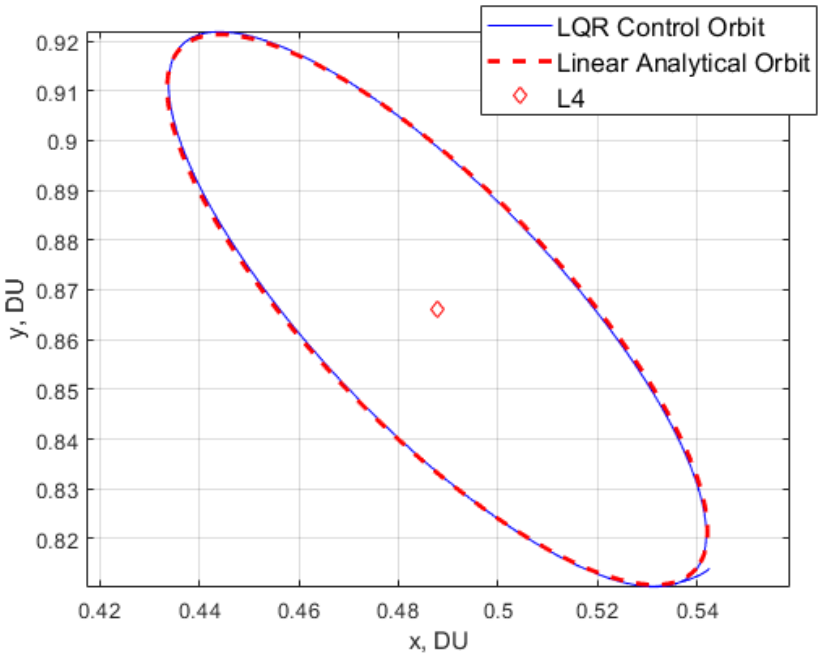

Figure 41: Successfully tracking the L_4 orbit using LQR

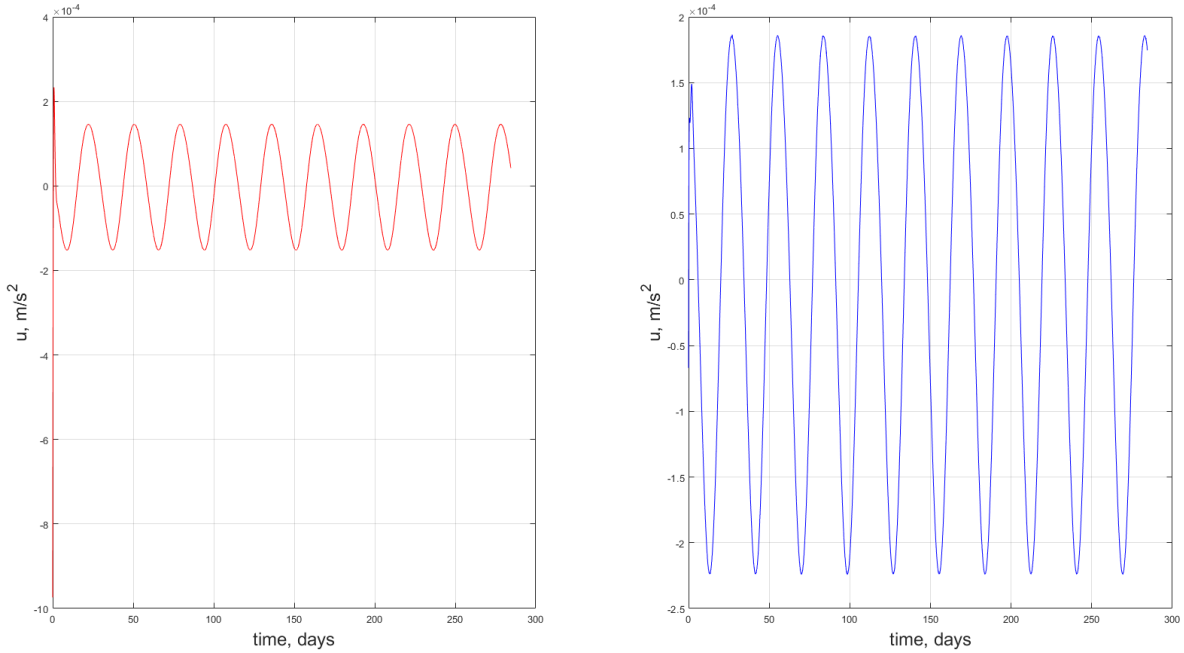

Figure 42: Control effort required to track the L_4 orbit using LQR

4.3.2 Sliding Mode Control at L_1

Figure 43 shows a successful track of the L_1 linear orbit using the sliding mode controller. The controller takes approximately one-quarter of an orbital period to successfully track to the orbit with acceptable error. This is influenced by parameters included in the controller design. When employing SMC control, the controller is operating very close to the sliding surface but cannot maintain contact with it. This ends up looking like a very high-frequency bang-bang control because the controller is constantly adjusting back-and-forth towards the sliding surface. This phenomena is called chattering and can occur in many SMC systems [38]. Fortunately, there are no signs of chattering in the controller designed for L_1 tracking. Counting the peaks/valleys in the lower left plot of Figure 44, there are 20: two for each of the ten orbital periods. This means that the controller is crossing the trajectory twice in the x- and y-directions each orbital period.

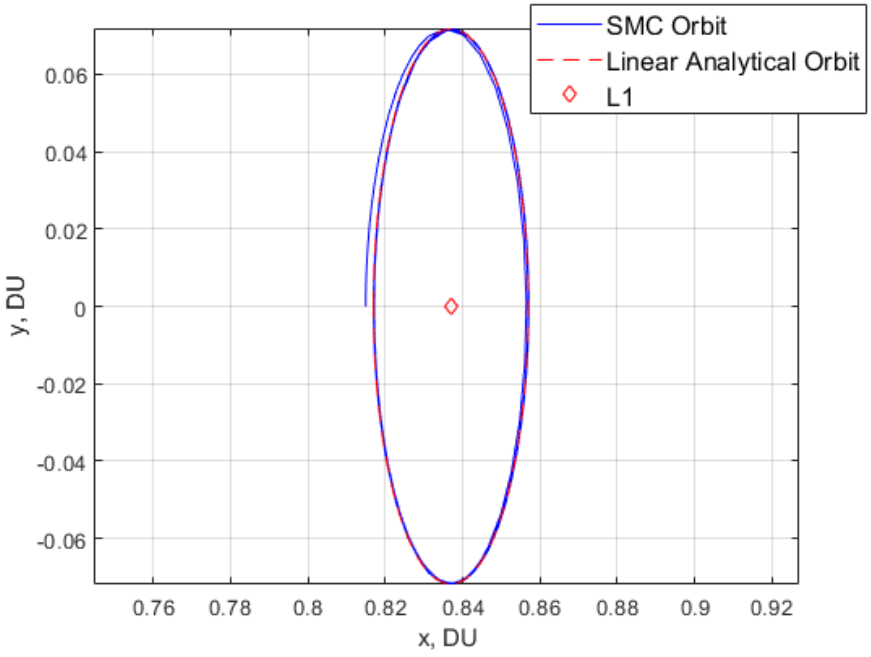

Figure 43: Successfully tracking the L_1 orbit using SMC

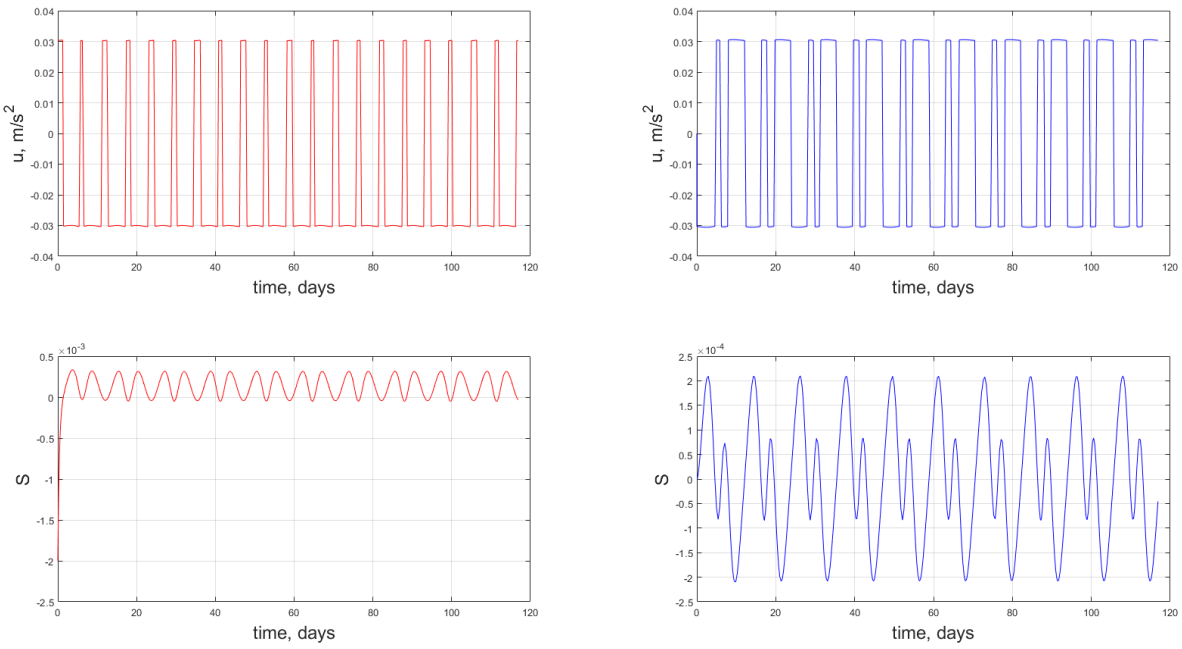

Figure 44: Control effort required to track the L_1 orbit using SMC

4.4 Summary

In this chapter it was shown that illumination of a target using non-collocated space-based mirrors in disparate orbit families is unachievable. The ability to illuminate a target using a collocated reflector/observer spacecraft operating in proximity was then demonstrated. Depending on the Lagrange point and orbit family, distance from a target's trajectory can have varying impacts to illumination performance. Additionally, the ability of LQR and Sliding Mode Controllers to track a desired orbit within acceptable error was proven.

V. Physical Mirror Experimentation and Testing

This chapter examines two critical design factors for a membrane mirror: material survivability and reflectance. Samples of Gold, Silver, and Aluminum were procured from a vendor and experimentally tested. These experiments include destructive survivability testing using a cold gas projectile gun and visible/infrared spectrum laboratory reflectance measurements.

5.1 Survivability Investigation of Membrane Mirrors

This section is focused on experimentally demonstrating the effects of artificial space debris on membrane mirror structures in cislunar space. Any space structure is subject to several critical environmental factors including charging, radiation, heating cycles, and meteoroid and space debris impact. Gossamer structures are especially susceptible to micrometeoroid and space debris impacts due to their thin, non-rigid design and potentially large profile once deployed. The differences between these impact phenomena are described by Pisacane [45]. A meteoroid is a small piece of celestial material orbiting the sun from a comet or asteroid, and a micrometeoroid is a small meteoroid with a mass typically less than one gram. Orbital debris is man-made objects in orbit that are not carrying out a useful function, and is the focus of the physical experimentation described in this section.

Boone [8] performed a theoretical analysis of the short- and long-term motion of artificial space debris generated by a catastrophic spacecraft mishap in the vicinity of the collinear Earth-Moon Lagrange points L_1 and L_2. Boone's research is the foundation for determining relative velocity profiles that inform the experimental testing. His analysis also explored the risks the catastrophic mishap would pose to notional spacecraft elsewhere in cislunar space. Specific locations included in the research are

the Lunar Gateway (part of NASA's planned Artemis missions), a spacecraft near L_1, a spacecraft near L_2, and a spacecraft conducting a low-energy transfer to the Moon from Earth.

Boone's analysis used the National Oceanic and Atmospheric Administration (NOAA) 16 satellite battery explosion as the baseline model for debris profiles. The mass distribution of particles created from the mishap and change in velocity relative to orbital trajectory are the two main parameters in the model. Table 12 below summarizes the relative velocity for the six mishap and spacecraft locations developed. These predictions were used to determine velocity settings for experimental testing.

Table 12: Average relative velocity of projectiles following catastrophic mishap the NOAA 16 spacecraft. Adapted from [8]

Mishap Location	Spacecraft Location	Average Relative Velocity (m/s)
L_1	Lunar Gateway	986.890
L_1	L_2	96.465
L_1	Earth-Moon Transfer	113.535
L_2	Lunar Gateway	1232.766
L_2	L_1	157.272
L_2	Earth-Moon Transfer	272.364

Six membrane mirror samples experiencing an orbital debris impact in cislunar space were simulated using a cold gas gun operated at Range A on Wright-Patterson AFB, OH courtesy of the 704th Test Group. The cold gas gun is routinely used by the Air Force Institute of Technology and Air Force Research Laboratory for ballistic testing [46]. The experimental setup is shown in Figure 45 below, and includes a firing control desk, a single-stage Nitrogen cold gas gun, and the test section. The gun operates by pressurizing a holding tank (Figure 46) to a specific firing pressure

determined through previous calibration and a desired projectile velocity. The stainless steel gas gun barrel is 12 feet long (Figure 47) and is loaded with a 0.5 in. steel ball bearing. Various solenoid valves control operation of the gun and are commanded via the firing control desk. The specimen is mounted in a 3 ft. by 3 ft. by 6 ft. test section (Figure 50) complete with a test stand, a wood- and steel-backed sand trap, lighting, and velocity sensors. Specifics on firing control, gas gun, and test section components, software, and operations is presented in detail by Hankins [46].

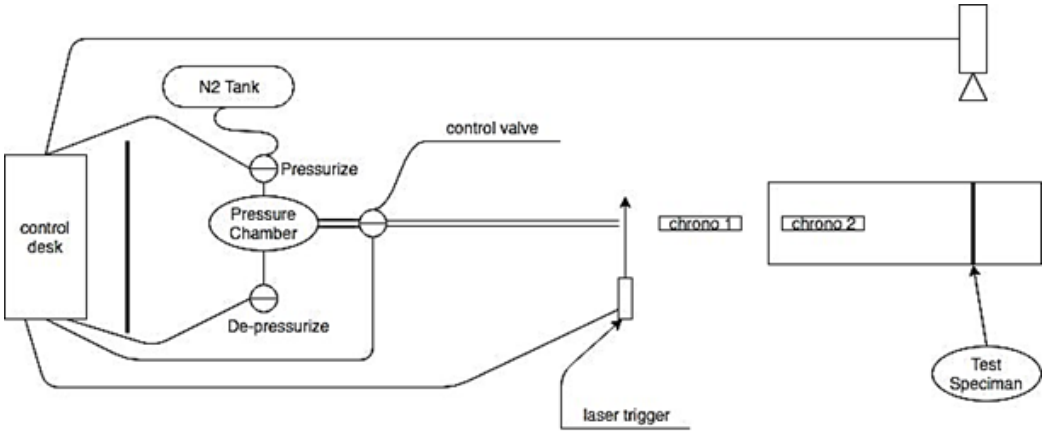

Figure 45: Cold gas gun setup

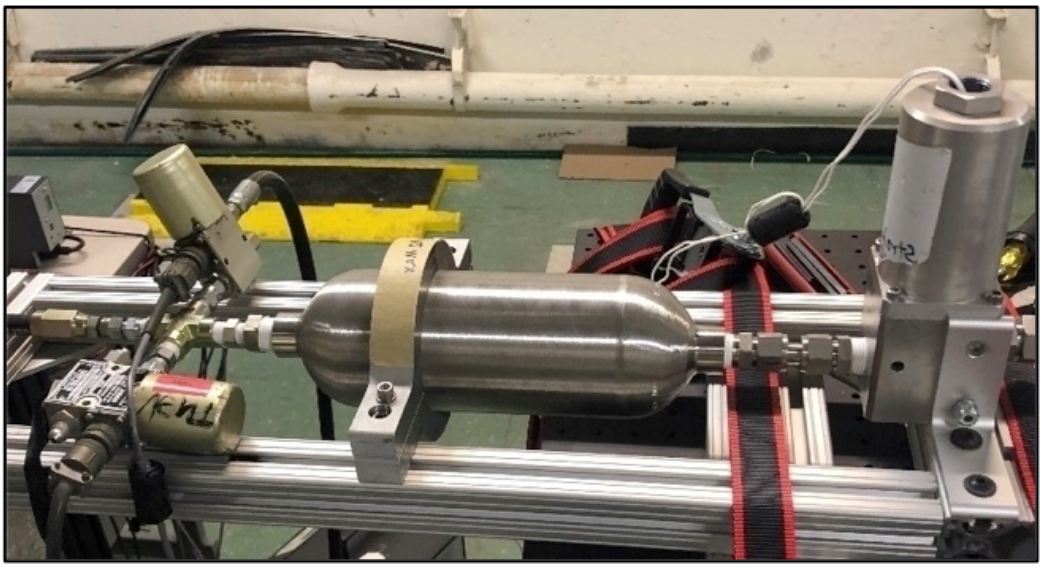

Figure 46: Cold gas gun Nitrogen holding tank

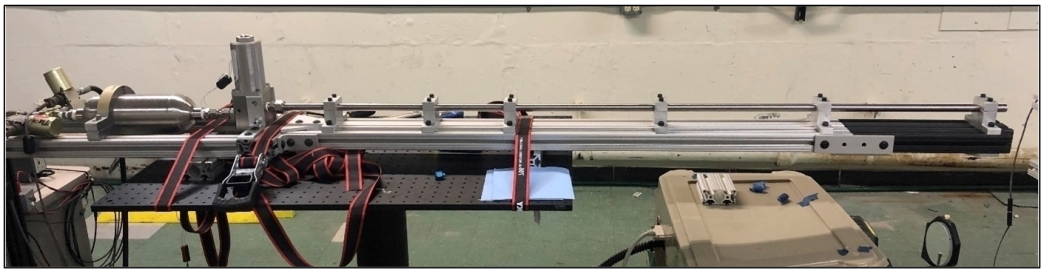

Figure 47: Cold gas gun barrel

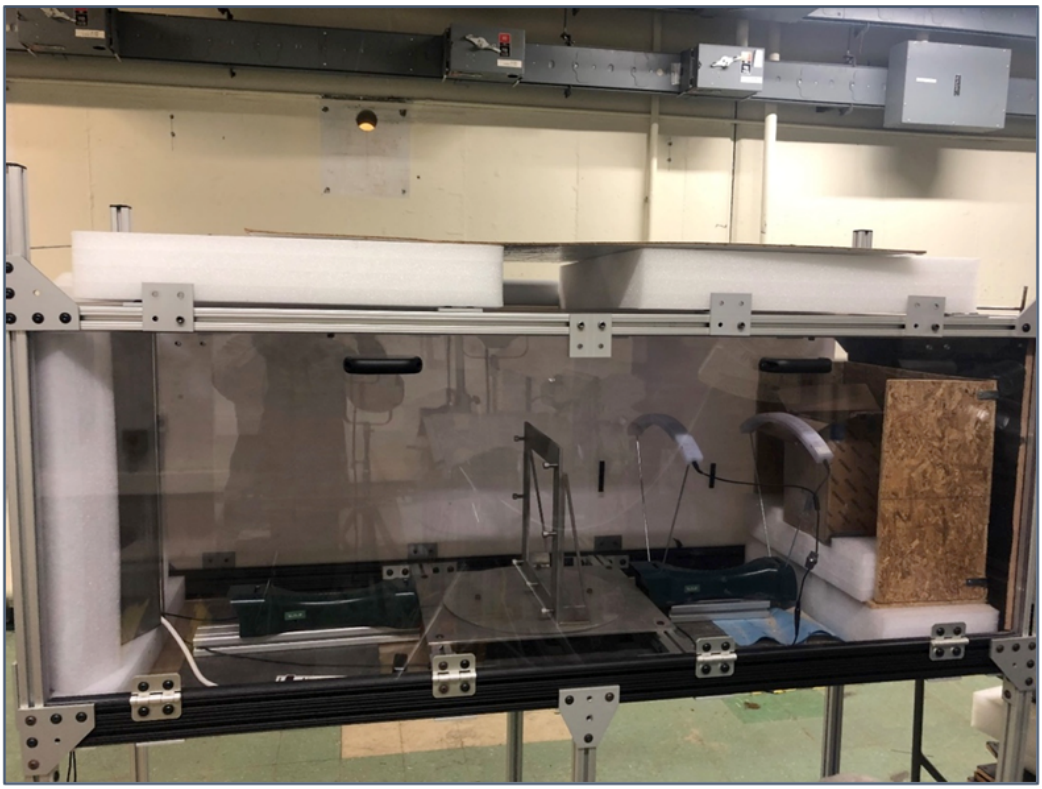

Figure 48: Cold gas gun test section

The only non-baseline component of the cold gas gun is the membrane mirror mounting plate. Typically, an armor plate for testing is bolted directly inside of the test stand. The plate for this experiment was designed to hold the test sample and bolt into the test stand. The plate's mounting ring was 3-D printed to accommodate a mirror test sample six inches in diameter with an opening behind the mirror surface for the projectile to pass through, see Figure 49. The full test setup with a mirror sample in place is shown in Figure 50.

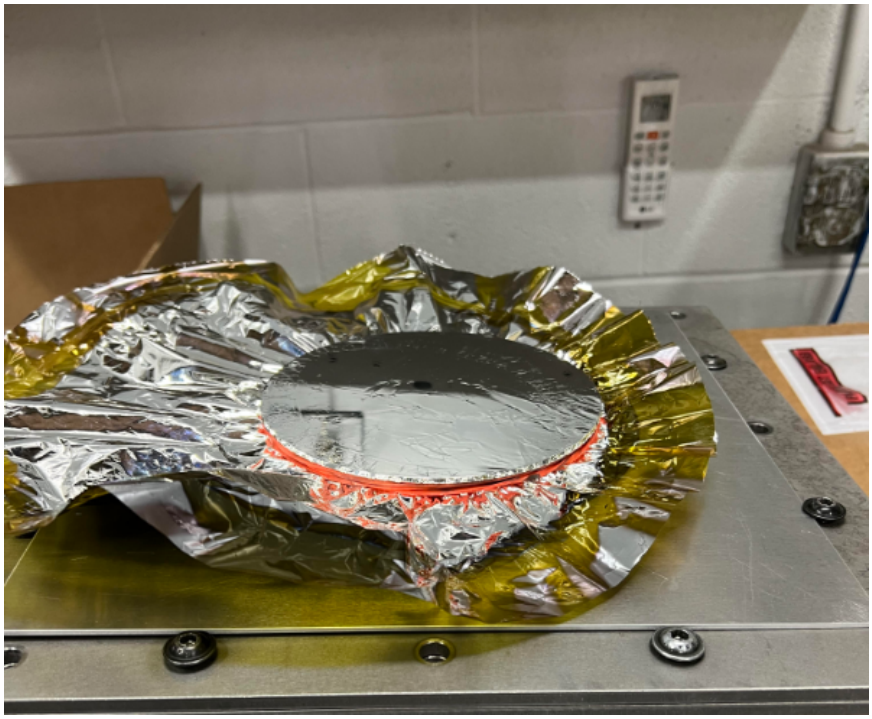

Figure 49: Cold gas gun mirror mounting frame

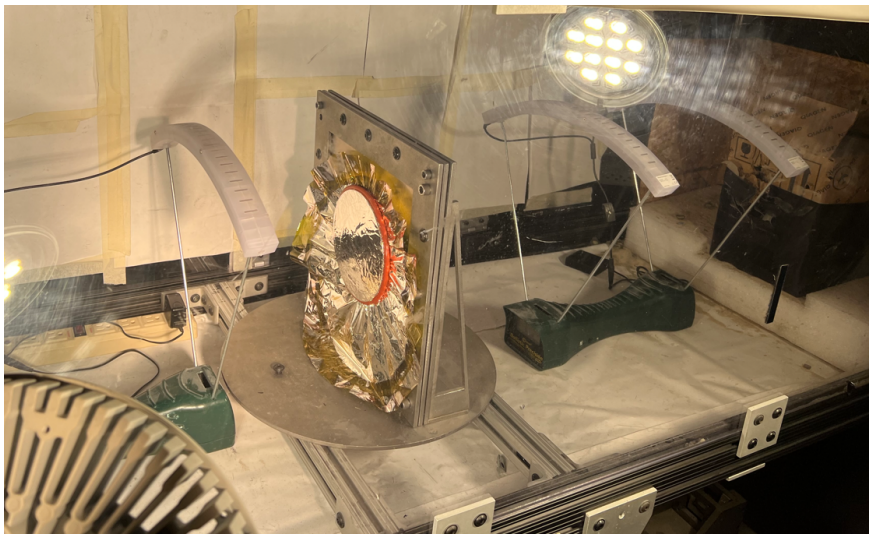

Figure 50: Cold gas gun mirror full setup with mirror

5.2 Analysis and Results of Membrane Mirror Survivability

Table 13 summarizes data from six cold gas gun firings of a 0.5 inch steel ball bearing through membrane mirror samples of various metallic coatings. Columns one and two of the table specify which sample and with what coating the experiment was performed. The calculated velocity of each projectile upon impact with the mirror is located in column three. This value was generated using a high speed camera focused on the test stand and processing software on the computers at the control station. A desired projectile velocity of 350 m/s was selected for these experiments. The decision to use 350 m/s was two-fold. 350 m/s envelopes the lower velocities from Boone's research in Table 12 for L_1, L_2, and Earth-Moon transfer orbits. Additionally, AFIT operators of the cold gas gun found use in firing near the limits of the gun to better build out the upper-end of the pressure-velocity relationship. The damage region in the fourth column is estimated based on photographic evidence taken after firings. The damage scale quantity is dimensionless and denotes hole size in the thin-film membrane relative to the 1.266 cm^2 cross-sectional area of the projectile. This is proportional to the metric κ used in the research of Villarreal et al. [47] to denote a relationship between projectile size and hole size. The final column counts the number of significant tear or corner features present in each hole.

Table 13: Membrane Mirror Survivability Testing

Sample #	Coating	Velocity (m/s)	Damage Region (cm^2)	Damage Scale	Tears
1	Al	339.419	17.094	13.5	1
2	Al	340.161	20.259	16	4
3	Au	344.605	14.517	11.5	3
4	Ag	343.615	15.511	12.3	3
5	Ag	345.596	10.130	8	5
6	Ag	349.792	7.597	6	2

Figures 51-56 show the post-impact membrane mirrors with arrows highlighting significant corner/tear features. While holes in the membrane from debris impacts will obviously degrade illumination performance by decreasing the reflective area, it is sharp corners or tears in the film structure that could potentially be very damaging to the mission. There seems to be no correlation between type of metallic coating and number of corner/tear features, but it is worth noting that every sample displayed at least one feature that could propagate under the right conditions, and four of the six samples displayed at least three of these features. Tears or corners present around the edge of the hole can propagate due to thermal expansion of the membrane, tensioning of the membrane by actuation, or additional impacts. To maintain surface figure and roughness, gossamer structures for both imaging and non-imaging (illumination) are placed under tension by their support structure. If this tension is applied transverse to a tear in the membrane following the formation of a hole, the tear could propagate and be catastrophic to the integrity of the structure. Lior [22] notes that tension placed across the membrane to maintain form could also cycle due to thermal expansion if the structure moves in and out of sunlight or experiences solar radiation pressure and wind. Maneuvering the spacecraft or repositioning the mirror may also introduce

loading in the membrane, especially if maneuvers and attitude control are performed with systems that cannot gently throttle up from, or down to, zero force.

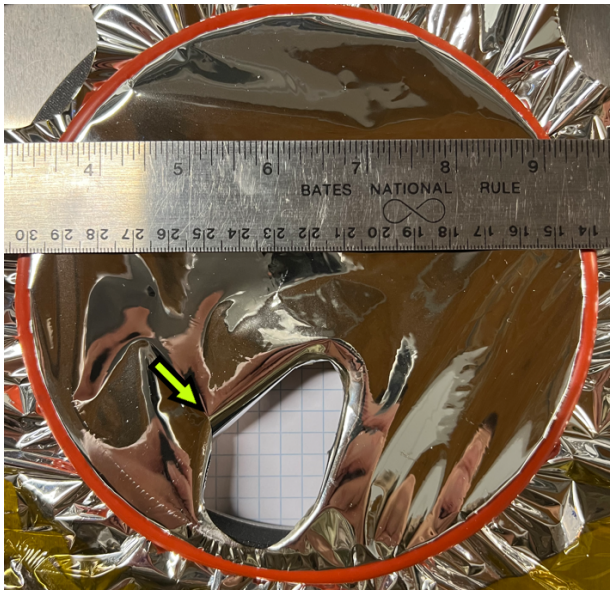

Figure 51: Sample #1: Aluminum coating. One tear feature is noted.

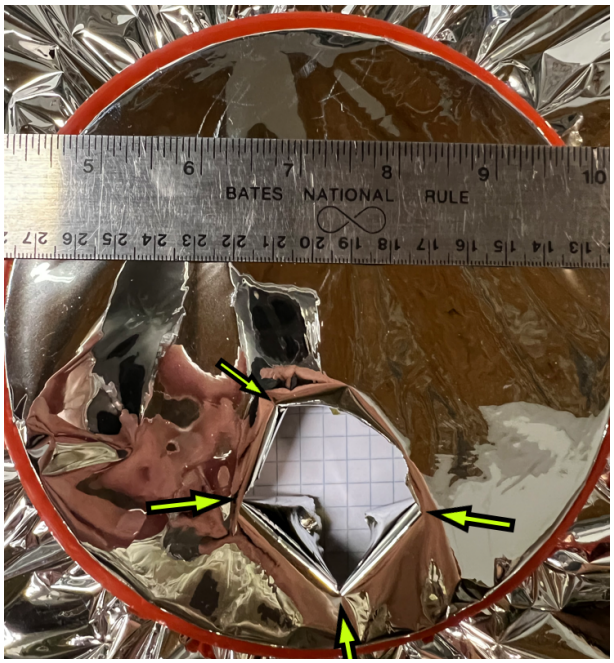

Figure 52: Sample #2: Aluminum coating. Four tear features are noted.

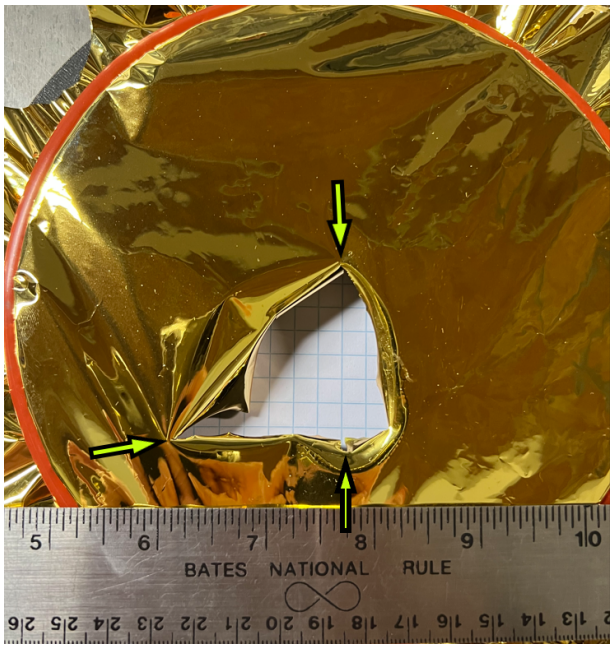

Figure 53: Sample #3: Gold coating. Three tear features are noted.

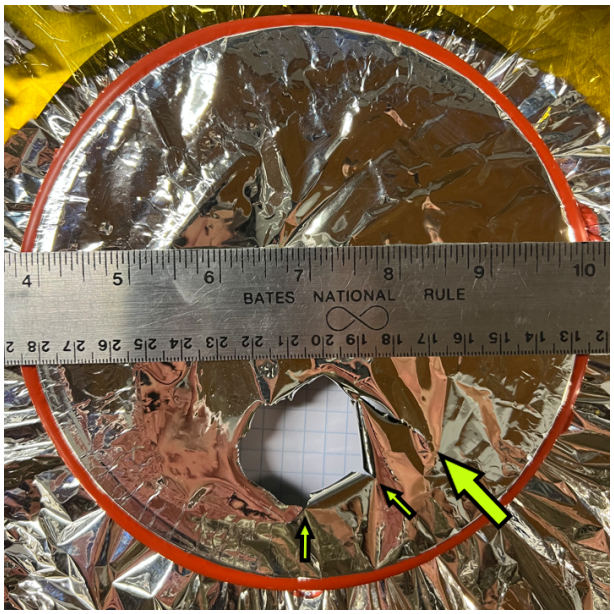

Figure 54: Sample #4: Silver coating. Three tear features are noted.

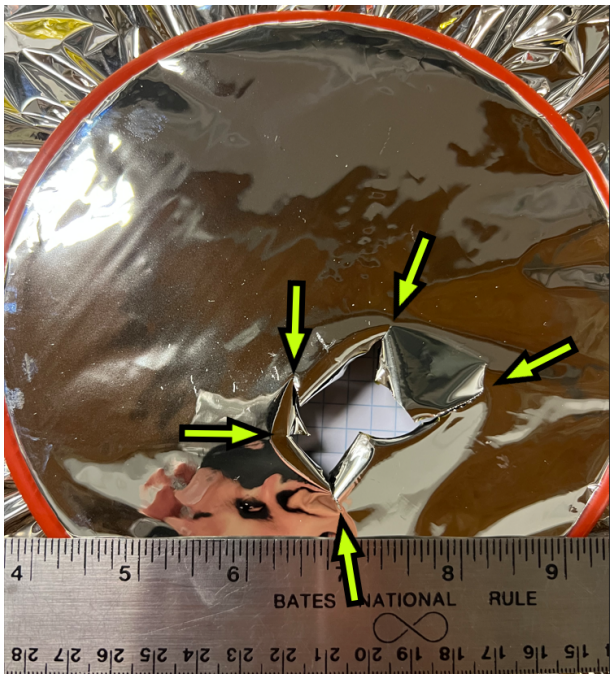

Figure 55: Sample #5: Silver coating. Five tear features are noted.

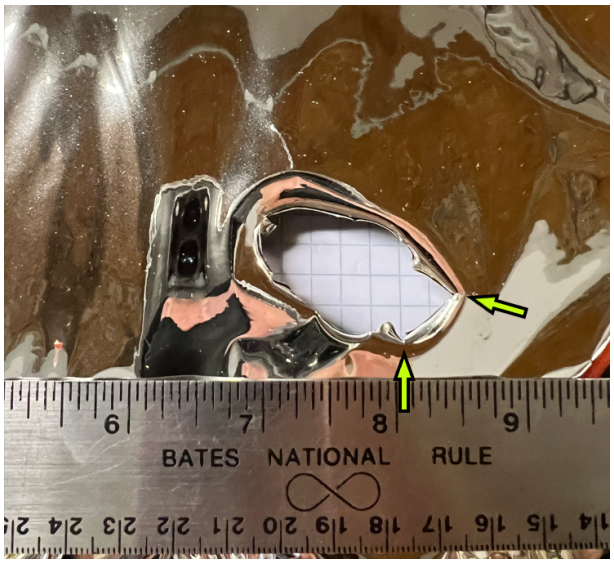

Figure 56: Sample #6: Silver coating. Two tear features are noted.

5.3 Experimental Determination of Reflectance

In this section, experimental reflectance testing of vendor-provided membrane mirror samples is discussed and analyzed. Two tests were performed: Specular Directional Reflectance measurements in the infrared wavelengths and Bidirectional Reflectance Distribution Function measurements in the visible wavelengths.

5.3.1 Specular Directional Reflectance

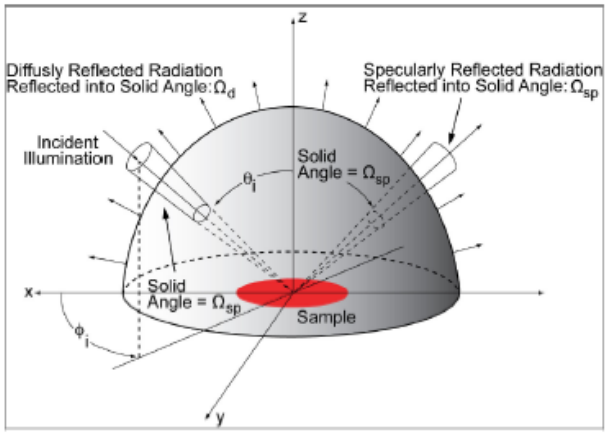

Figure 57: Specular Directional Reflectance test. Adapted from [6]

Specular Directional Reflectance (SDR) describes the ratio of specularly reflected radiation reflected into a solid angle relative to incident illumination. SDR is depicted in Figure 57 above. The SDR measurements were performed using the Surface Optics Corp. SOC-100 Hemispheric Directional Reflectometer at AFIT, see Figure 58. The SOC-100 measures Hemispherical Directional Reflectance (HDR), the ratio of the power reflected by a sample into a narrow solid angle to the incident power when illuminated hemispherically from all incident angles (2π steradians). Diffuse Directional Reflectance (DDR) is all the reflected energy not contained in the narrow solid angle of specular reflection. It is measured in the SOC-100 by blocking the specular reflection from the incident beam with a baffle and measuring the reflected

power (now entirely diffuse). Since energy is conserved, SDR is calculated by taking the difference between the HDR and the DDR [6]. The test was performed at infrared wavelengths of 1-25 μm at incident angles of $\theta = 20, 40, 60, 80°$. Results for each test are produced from the 5-7 μm band of data and are presented in Table 14 below. The 5-7 μm band was chosen because it demonstrated the least amount of noise (see Appendix), but signal-to-noise ratio can still muddy the sensitivity of the SOC-100 system. For example, the Gold 80 deg. data displays HDR and SDR above 100. This is not physically possible and is an artifact of noise.

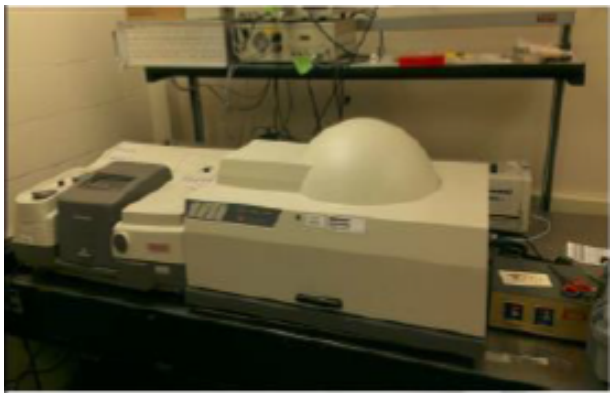

Figure 58: Surface Optics Corp. SOC-100 Hemispheric Directional Reflectometer. Adapted from [6]

Table 14: Membrane Mirror Specular Directional Reflectance Testing

Coating	Angle (deg.)	HDR	DDR	SDR
Au	20	98.6440	0.7832	97.8660
Au	40	99.2880	1.1697	98.1169
Au	60	97.3662	1.2823	96.0905
Au	80	101.7240	1.0658	100.6560
Average				98.1824
Ag	20	99.5089	1.0636	98.4496
Ag	40	98.5210	1.3971	97.1168
Ag	60	98.7354	3.5106	95.2132
Ag	80	95.4667	1.5066	93.9486
Average				96.1821
Al	20	98.3704	1.0079	97.3631
Al	40	97.7408	1.0325	96.7150
Al	60	94.9479	1.4313	96.5229
Al	80	99.3506	1.5212	97.8261
Average				97.1068

The SOC-100 produced average reflectance values of approximately 98%, 96%, and 97% for Gold, Silver, and Aluminum, respectively. As previously mentioned, these tests were performed in the infrared spectrum, not in the visible spectrum. These tests provide data regarding performance of membrane mirror samples near the visible spectrum, but cannot necessarily be extrapolated to the visible spectrum. The capability to perform SDR in the visible spectrum was unavailable. The trends for HDR, DDR, and SDR on each test are presented in the Appendix.

5.3.2 Bidirectional Reflectance Distribution Function

Bidirectional Reflectance Distribution Function (BRDF) is the ratio of the radiance (L_r) reflected from a surface into a unit solid angle in a given direction (θ_r, ϕ_r) to the incident irradiance (E_i) from a given direction (θ_i, ϕ_i) [48]. See Equation (78) and Figure 59 below. The BRDF was used in this research as a method to back out reflectance values following generation of experimental data. This is a complex process, as experimental data must be fit to any number of BRDF models available in the literature. The choice of model depends on what phenomena are of utmost importance to represent. Bishop et al. [49] and Nauyoks et al. [7] contrast some modern BRDF modeling methods, including the difficulty involved in selection. Three BRDF models were applied to experimental data in this research.

$$BRDF(\theta_r, \phi_r, \theta_i, \phi_i) = \frac{dL_r(\theta_r, \phi_r)}{dE_i(\theta_i, \phi_i)} \tag{78}$$

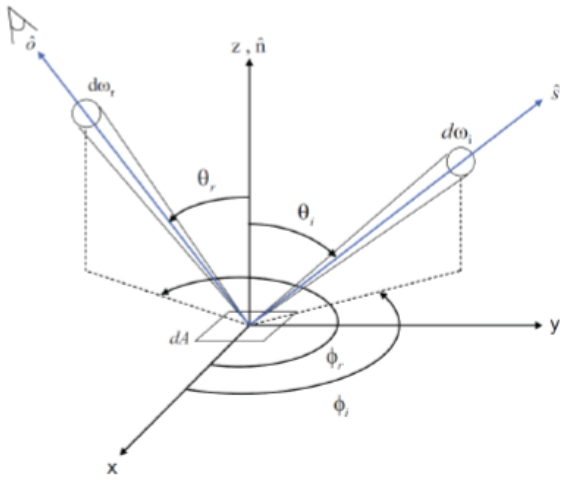

Figure 59: Bidirectional Reflectance Distribution Function test. Adapted from [6]

Measurements for determination of reflectance from the BRDF of each metallic coating were performed using the Complete Angle Scatter Instrument (CASI) at AFIT.

Operation of this instrument is depicted in Figure 60, with angles $\alpha, \beta, \gamma,$ and δ all used to direct incident and reflection direction.

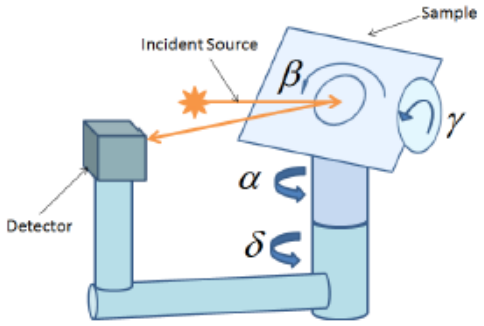

Figure 60: Example schematic of a BRDF experiment. Adapted from [7]

Measurements were taken at 543 nm and $\theta_i = 20, 40,$ and $60°$, which puts specular peaks at $\theta_r = 20, 40,$ and $60°$. The Priest-Germer, Sandford-Robertson, and Wellems models were used to fit experimental data to a BRDF function. Overall, the Wellems model was the best fit for all three coatings. An experimental data summary is included in Table 15 below, and plots of the experimental data are included in the Appendix.

Table 15: Experimental BRDF data

Coating	Angle (deg.)	Reflectance (%)
Au	20	10
Au	40	11
Au	60	7
Ag	20	15
Ag	40	10
Ag	60	8
Al	20	24
Al	40	11
Al	60	7

The data in Table 15 above is useful even though it does not align with reflectance properties obtained by other experimental methods or supported by literature. It is difficult to turn BRDF measurements into total reflectance, the values produced in the infrared spectrum from the SOC-100 device. When a measurement is taken with CASI, it must be integrated approximately 0.5 deg. around the specular peak, but anything outside of this won't get counted towards the reflectance. At 543 nm, vendor specifications provide reflectance values of approximately 75% for Gold, 95% for Silver, and 90% for Aluminum. The fact that Gold has the smallest reflectance in the vendor, SOC-100, and CASI may give indication of consistency. However, the CASI data cannot provide direct experimental verification of vendor specifications or drive any significant conclusion.

5.4 Summary

The detrimental effect of orbital debris impact on membrane mirrors was demonstrated experimentally in this chapter with the use of a cold gas gun test setup. The presence of corner and tear features around the hole is the most troubling artifact following a ballistic impact, however a hole in the mirror surface also decreases usable reflective area. The reflectance measurements discussed in this section were gathered in the infrared (using HDR) and visible (using BRDF) wavelengths. Unavailability of visible spectrum total reflectance measurements from a Hemispherical Directional Reflectance instrument precluded significant conclusions into the validity of vendor specifications. The difficulty in gathering and extrapolating BRDF measurements to quantify total reflectance was demonstrated in this experiment.

VI. Conclusions

This research used simulation tools to examine the feasibility of using space-based reflectors located in periodic L_1, L_2 and L_4 orbits to augment illumination of a target resident space object located in GEO, and periodic L_1, L_2, and L_4 orbits. Viewing the target was an observer spacecraft located in the same orbit family as the target.

The first set of scenarios examined placing non-collocated reflector and observer spacecraft into different orbit families. The observer spacecraft attempted to view the target spacecraft located inside its orbit family. The vast distances of cislunar space and the inverse square relationship of distance to reflected light energy proved to be prohibitive in these cases. The reflected light beam simply travels too far between orbit families before reaching the target to meet the visual magnitude criteria, true even in orbit families around the same Lagrange point. Only one combination of orbits produced a non-zero contribution from the reflector light-source: an L_1 Halo reflector beaming light towards the L_1 Lyapunov orbit family met the visual magnitude detection threshold 2.4% of the time.

The second set of scenarios examined placed a collocated reflector and observer spacecraft near a target spacecraft in the same orbit family. By drastically decreasing the distance a reflected light beam travels to reach the target, all four orbit families examined showed significant contributions from the reflector. Since the sunlight incident on the reflector surface is nearly always reaching the target due to their proximity, a restriction was added to focus on geometries where the reflector/observer can illuminate and detect the back, or dark, side of the target. These placements provided between 18.9% and 57.9% illumination of the target's dark side, with the L_1 families outperforming the L_2 families.

Following the demonstration that a collocated reflector/observer system can successfully illuminate proximity targets near the L_1, L_2, and L_4 Lagrange points, the

impacts of the parameter continuation method inside orbit families was examined. When operating in proximity of the target inside the same orbit family, relative orbit size and orbital period will impact the duration of visible periods. Moving away from a target spacecraft's orbit through a periodic family has a pronounced negative effect on the reflector's ability to illuminate the target. The trends associated with this behavior can differ significantly depending on the orbit family in use. Lyapunov families at L_1 and L_2 show steady downward-trending performance, while Halo families around the same Lagrange points provide finite regions where performance is unimpacted. Due to the nature of L_4 Planar families, a different parameter continuation is used, and illumination becomes near-impossible only partway through the full spectrum of orbits in the family.

The use of a Linear Quadratic Regulator and Sliding Mode Control were demonstrated with L_1, L_2, L_4 and L_1 periodic orbits, respectively. Both controllers exerted control over the trajectory of a spacecraft to follow a desired linear orbit subject to the nonlinear dynamics of the Circular Restricted Three-Body Problem. A reflector/observer spacecraft operating in proximity of a target spacecraft may be located as close as a few hundred kilometers at points in the trajectory. It is important that positive control can be exercised to avoid on-orbit mishaps. In this case, tracking a desired orbit to within ~ 4 km was demonstrated.

Additionally, this research provided experimental insight into the behavior of thin-film membrane structures. This was accomplished through destructive testing via high-speed projectiles and reflectance measurements. Subjected to projectiles mimicking a man-made debris object traversing cislunar space, every sample tested displayed a large region of damage relative to projectile size. All samples demonstrated the presence of tear features that could propagate and cause further damage to the membrane structure. Four of the six samples showed at least three tear features. Vis-

ible and infrared spectrum measurements were performed to determine reflectance of each metallic coating on the samples. The infrared measurements supported vendor and literature data on reflectance, but difficulties inherent in the method (Bidirectional Reflectance Distribution Function) of performing visible spectrum measurements were experienced.

6.1 Significance of Research

This research provided one of the first in-depth analyses of using space-based reflectors to illuminate resident space objects. This understanding will be valuable for understanding how to augment missions such as Space Situational Awareness and Space Traffic Management. Military, civil, and commercial ventures will all use these mission areas and must work collectively to ensure safe use of cislunar space while achieving their objectives. Missions involving rendezvous and proximity operations are critically important in a congested space environment, or in an environment with the unique challenges of cislunar space. Augmented illumination can directly assist in the execution of these operations, as many systems rely on the visible spectrum of light.

This research also provided one of the first experimental tests into debris hazards directly associated with cislunar space. The research test conditions were informed directly from applicable literature on cislunar debris hazards following a catastrophic spacecraft breakup.

6.2 Publications and Scholarly Efforts

The following list of publications and scholarly efforts illustrates the impactful nature of this research on the wider community at the time of this thesis submission.

6.2.1 Conference Papers

- Cook, A. E., Dahlke, J. A., Bettinger, R. A., "Preliminary Study: Employing Space-Based Mirrors for Augmented Illumination of Cislunar Resident Space Objects," 2023 AIAA Science and Technology Forum and Exposition, National Harbor, MD, January 2023.

6.3 Future Research

The analysis conducted in the present research may be expanded with follow-on research. Avenues for future research include:

- Examine the attitude control necessary for illuminating resident space objects via rendezvous and proximity operations using a reflector/observer spacecraft in low and geosynchronous Earth orbits.
- Examine the attitude control necessary for cislunar illumination operations for select rendezvous cases near the collinear Lagrange points.
- Examine mirror folding, packaging, and deployment mechanisms for use with a CubeSat (12U or 27U) or full-size spacecraft bus.

VII. Appendix

7.1 SOC-100 Hemispheric Directional Reflectometer Plots

Figures 61-72 show the experimental data for Silver (Figures 61-64), Gold (Figures 65-68), and Aluminum (Figures 69-72) membrane mirror samples taken with the SOC-100 instrument. In each plot, the blue line represents Hemispherical Directional Reflectance (HDR), the gold line represents Diffuse Directional Reflectance (DDR), and the green line represents Specular Diffuse Reflection (SDR).

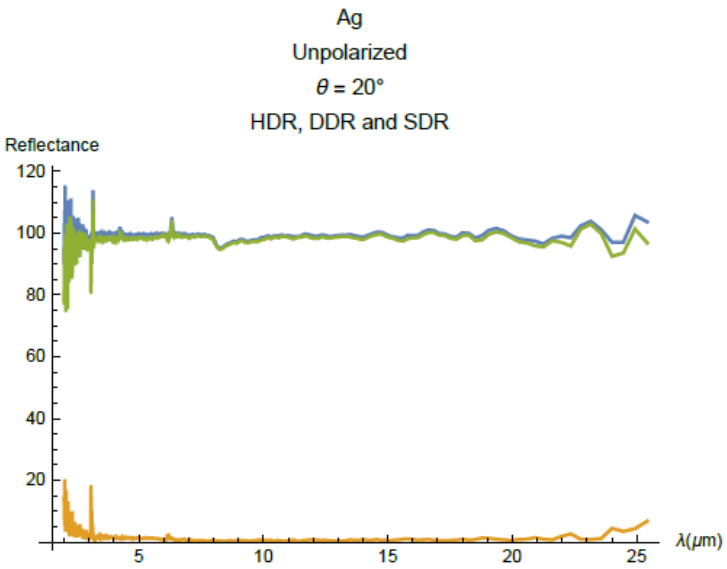

Figure 61: HDR, DDR, and SDR for Silver membrane mirror sample at 20 deg. incidence angle

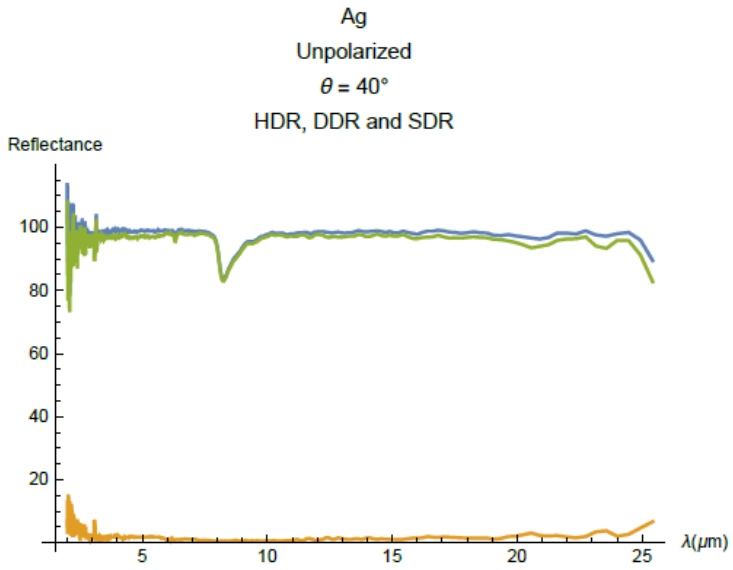

Figure 62: HDR, DDR, and SDR for Silver membrane mirror sample at 40 deg. incidence angle

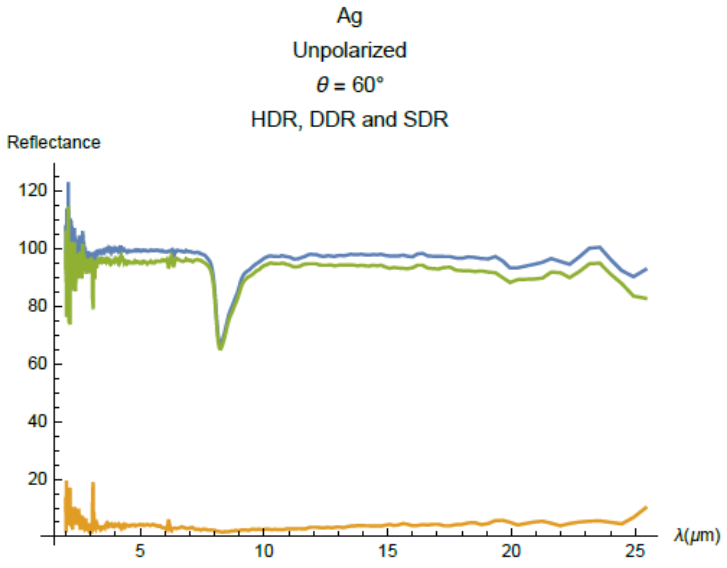

Figure 63: HDR, DDR, and SDR for Silver membrane mirror sample at 60 deg. incidence angle

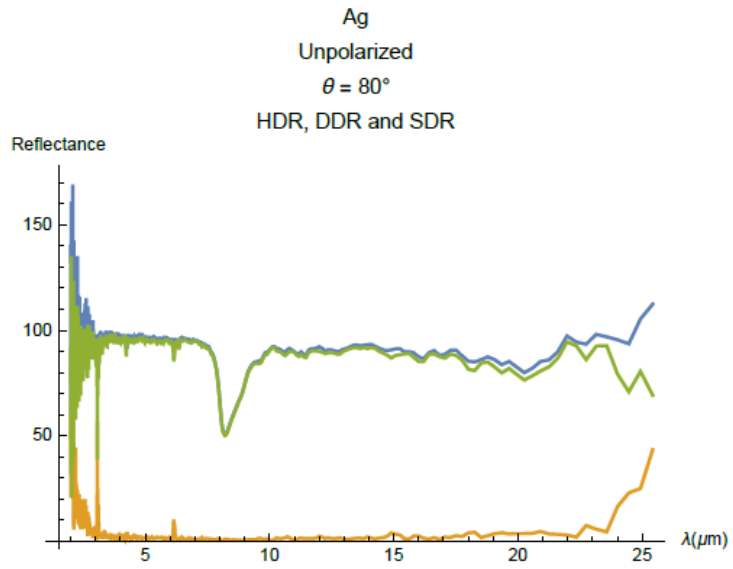

Figure 64: HDR, DDR, and SDR for Silver membrane mirror sample at 80 deg. incidence angle

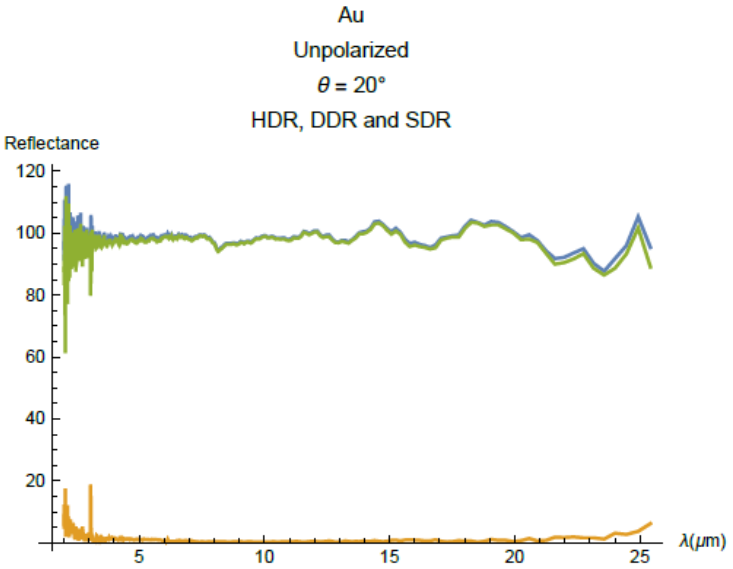

Figure 65: HDR, DDR, and SDR for Gold membrane mirror sample at 20 deg. incidence angle

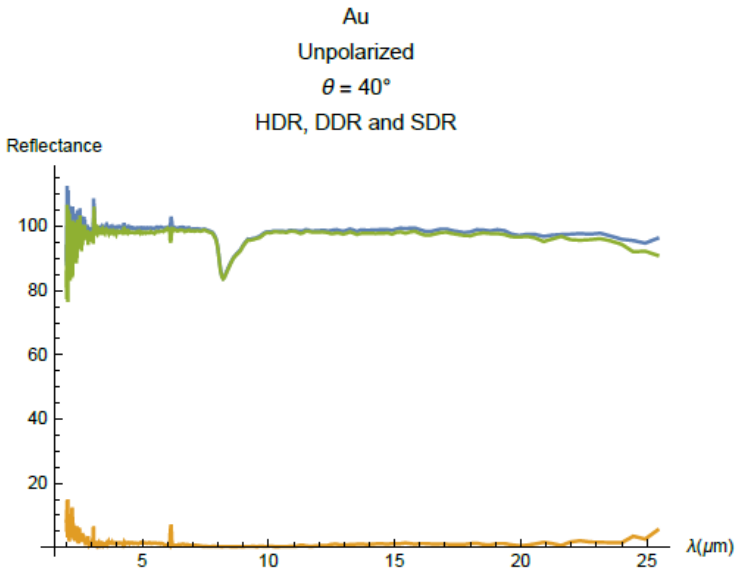

Figure 66: HDR, DDR, and SDR for Gold membrane mirror sample at 40 deg. incidence angle

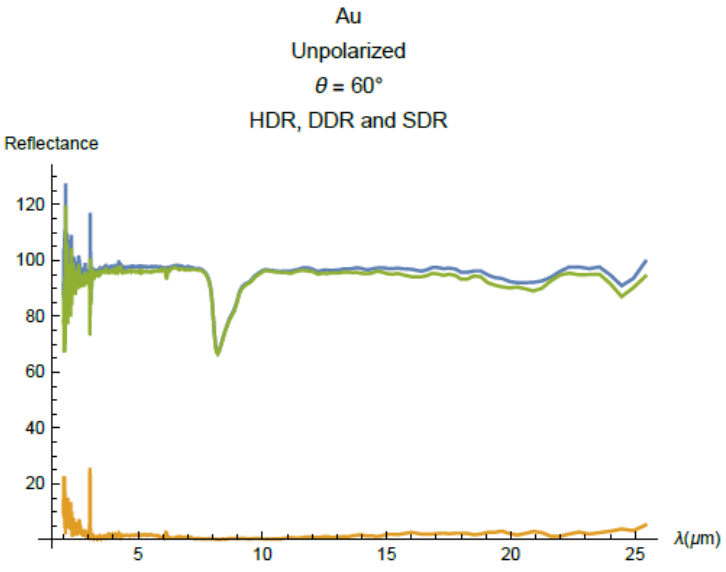

Figure 67: HDR, DDR, and SDR for Gold membrane mirror sample at 60 deg. incidence angle

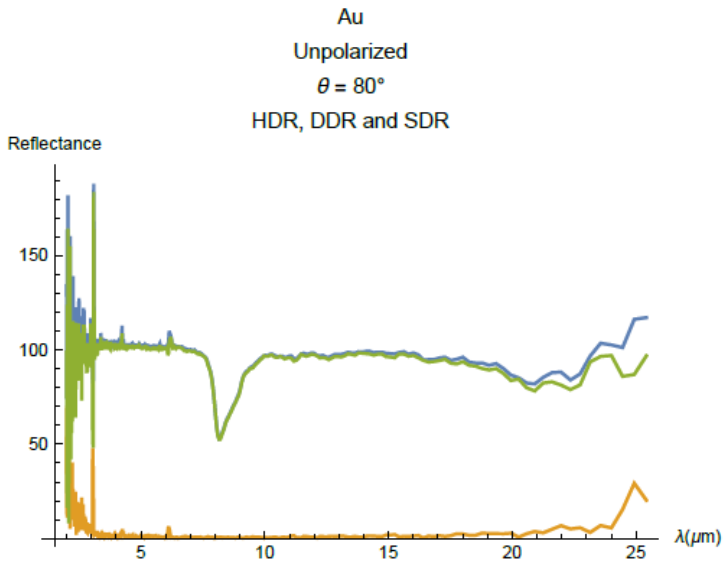

Figure 68: HDR, DDR, and SDR for Gold membrane mirror sample at 80 deg. incidence angle

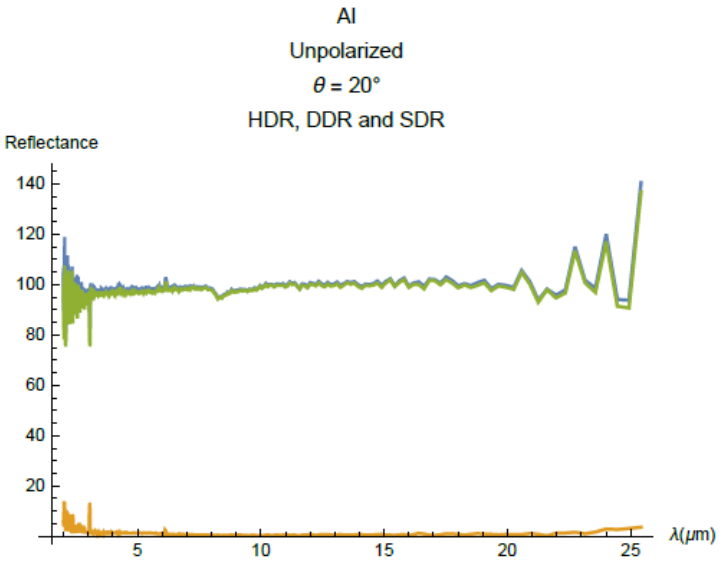

Figure 69: HDR, DDR, and SDR for Aluminum membrane mirror sample at 20 deg. incidence angle

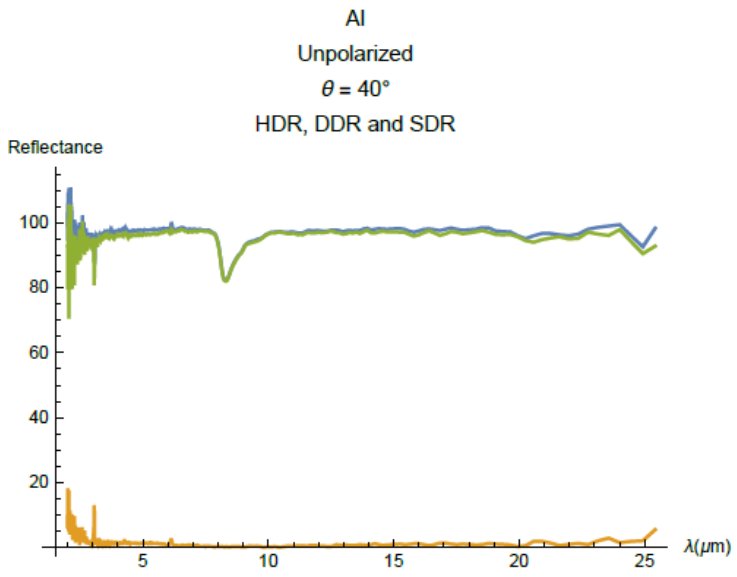

Figure 70: HDR, DDR, and SDR for Aluminum membrane mirror sample at 40 deg. incidence angle

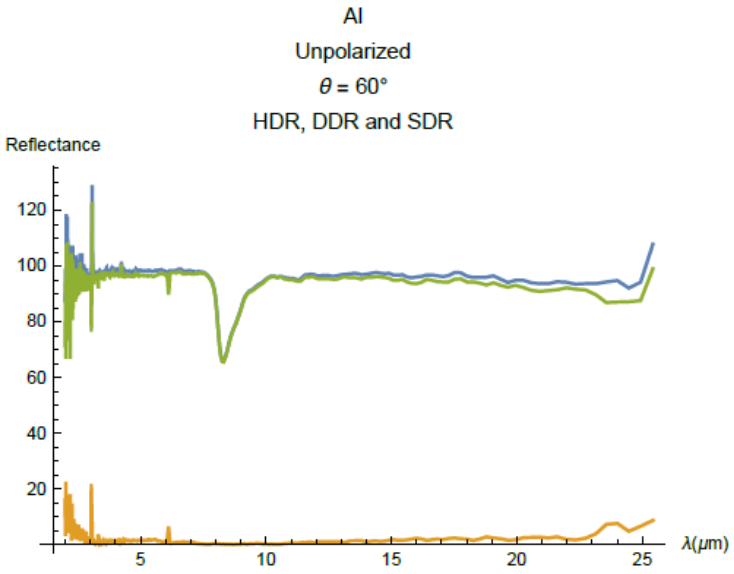

Figure 71: HDR, DDR, and SDR for Aluminum membrane mirror sample at 60 deg. incidence angle

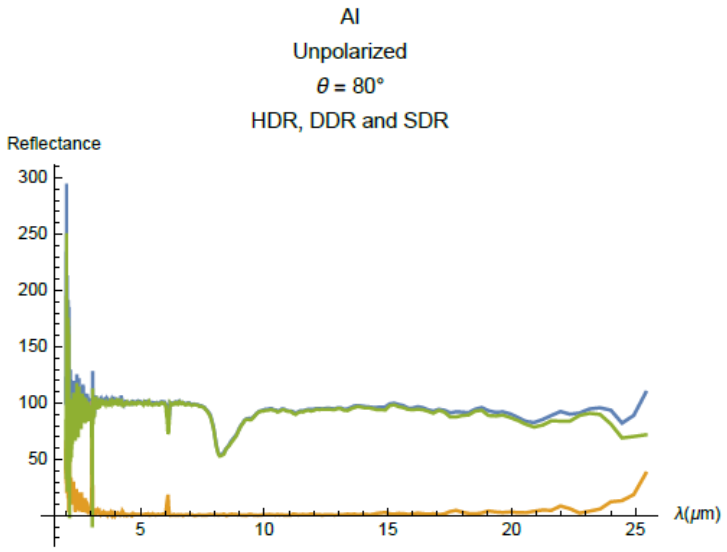

Figure 72: HDR, DDR, and SDR for Aluminum membrane mirror sample at 80 deg. incidence angle

7.2 Complete Angle Scatter Instrument (CASI) Bidirectional Reflectance Distribution Function (BRDF) Results

Figures 73-76 show the experimental data for Silver membrane mirror samples taken using the CASI. Measurements were conducted at incidence angles of 20, 40, and 60 deg. and curve-fit using three BRDF microfacet models [49]: Priest-Germer, Sandford-Robertson, and Wellems. The plot showing specular peaks at 20, 40, and 60 deg. is represented in standard BRDF units of Steradian^{-1}. Curve-fit plots are represented using dimensionless reflectance (0.0-1.0) versus incident angle in radians. Figures 77-80 and 81-84 show equivalent experimental data for Gold and Aluminum samples, respectively.

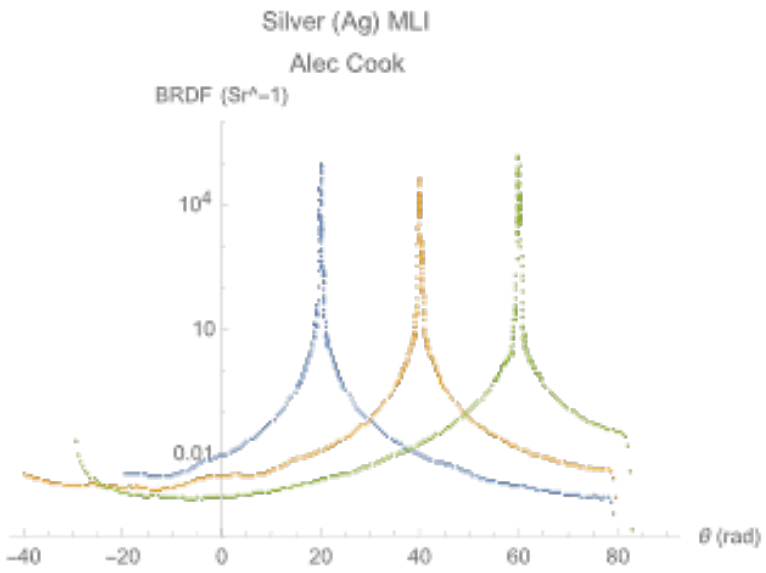

Figure 73: BRDF specular peaks at incidence angles of 20, 40, and 60 deg. for Silver membrane mirror

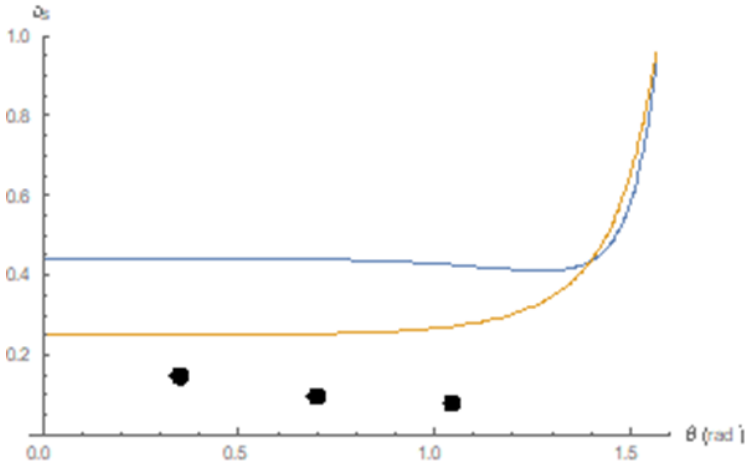

Figure 74: Priest-Germer curve-fit for Silver membrane mirror sample

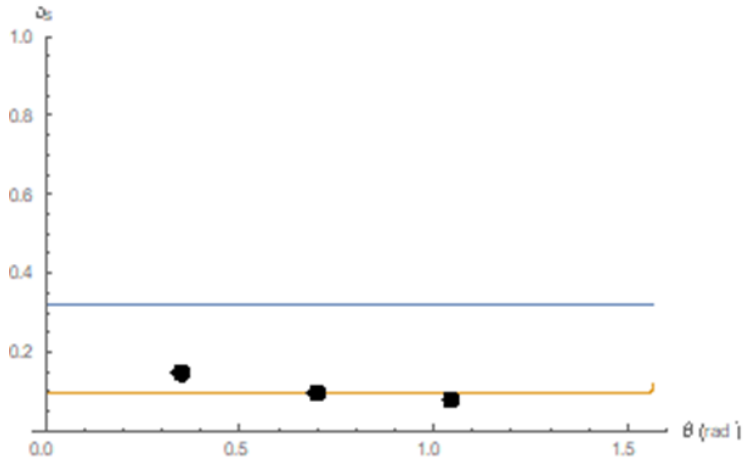

Figure 75: Sandford-Robertson curve-fit for Silver membrane mirror sample

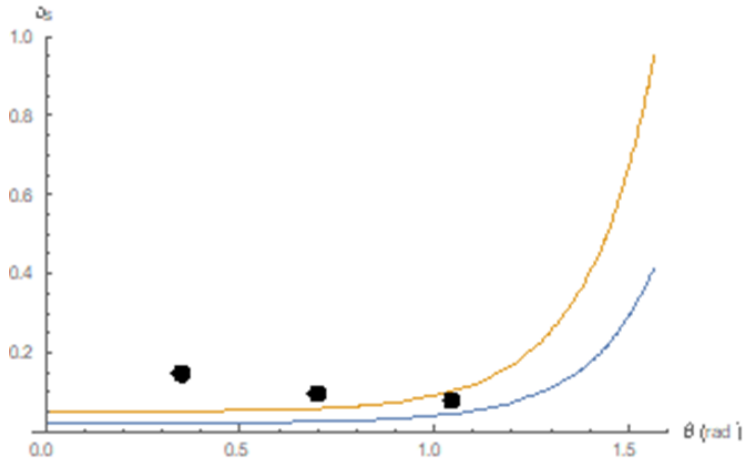

Figure 76: Wellems curve-fit for Silver membrane mirror sample

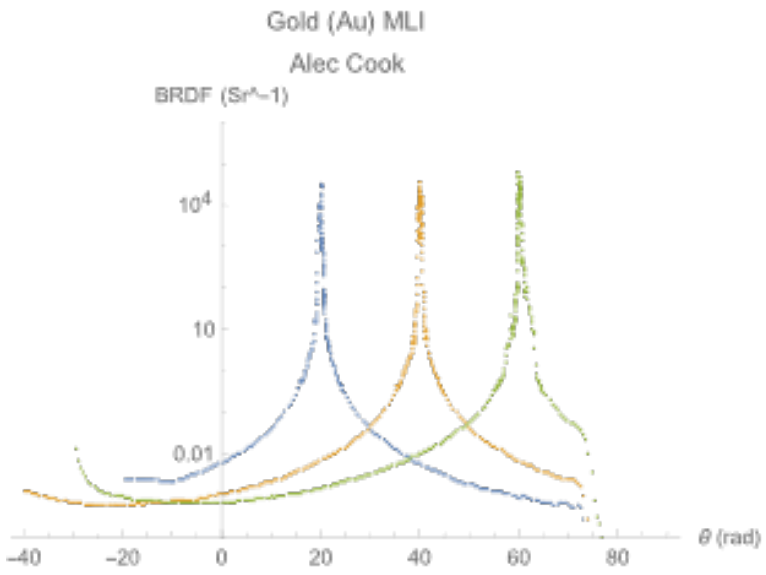

Figure 77: BRDF specular peaks at incidence angles of 20, 40, and 60 deg. for Gold membrane mirror

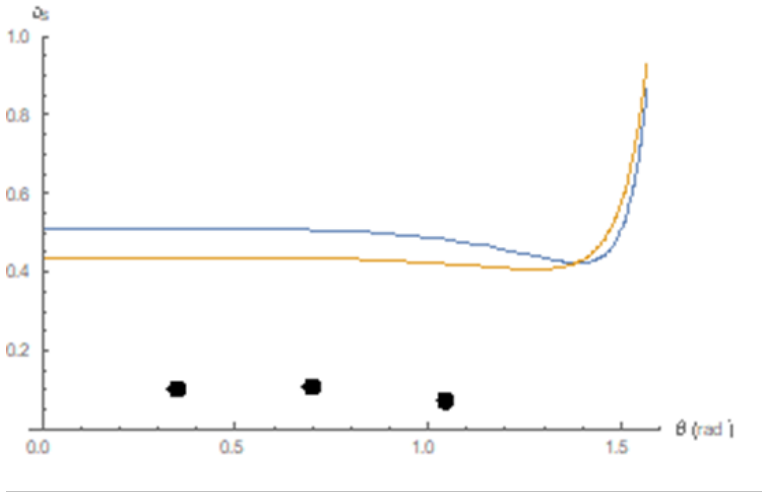

Figure 78: Priest-Germer curve-fit for Gold membrane mirror sample

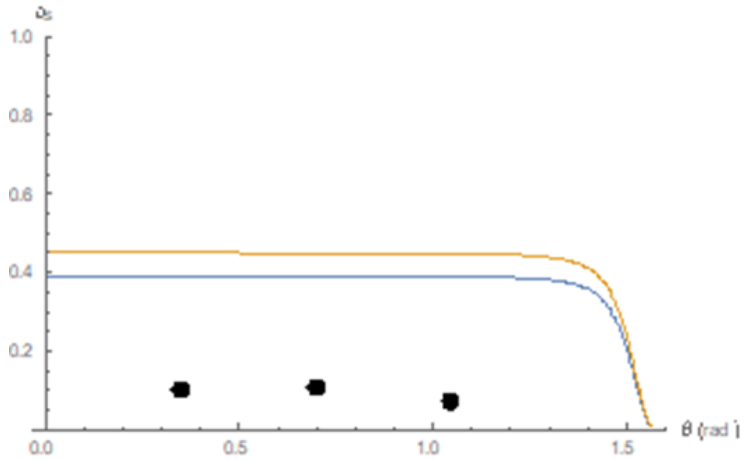

Figure 79: Sandford-Robertson curve-fit for Gold membrane mirror sample

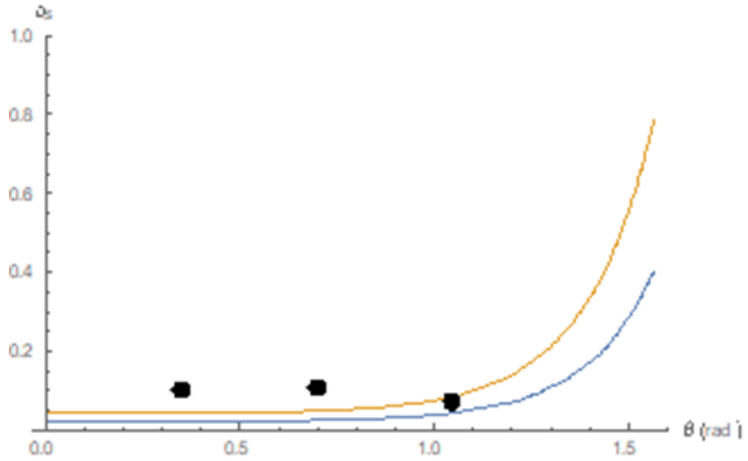

Figure 80: Wellems curve-fit for Gold membrane mirror sample

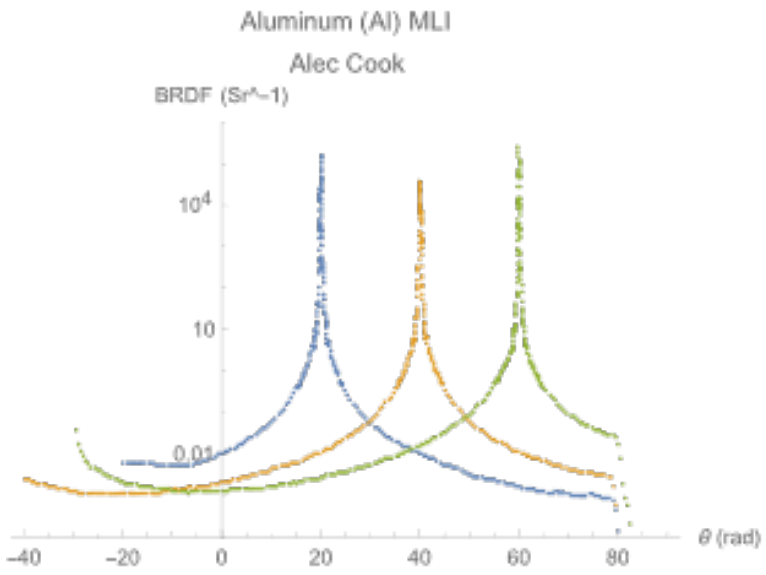

Figure 81: BRDF specular peaks at incidence angles of 20, 40, and 60 deg. for Aluminum membrane mirror

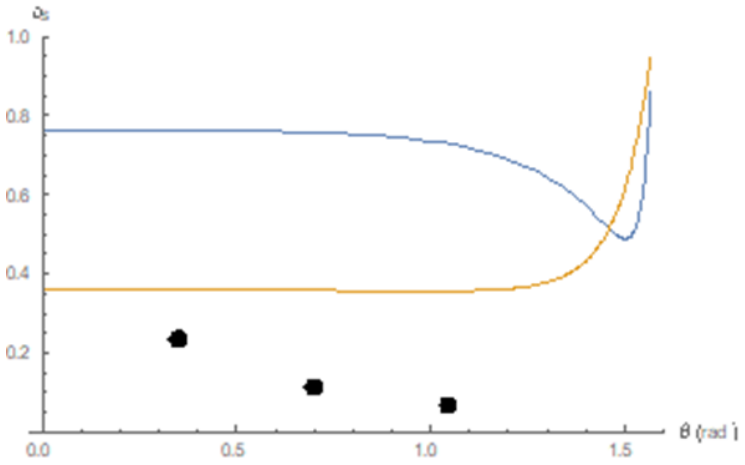

Figure 82: Priest-Germer curve-fit for Aluminum membrane mirror sample

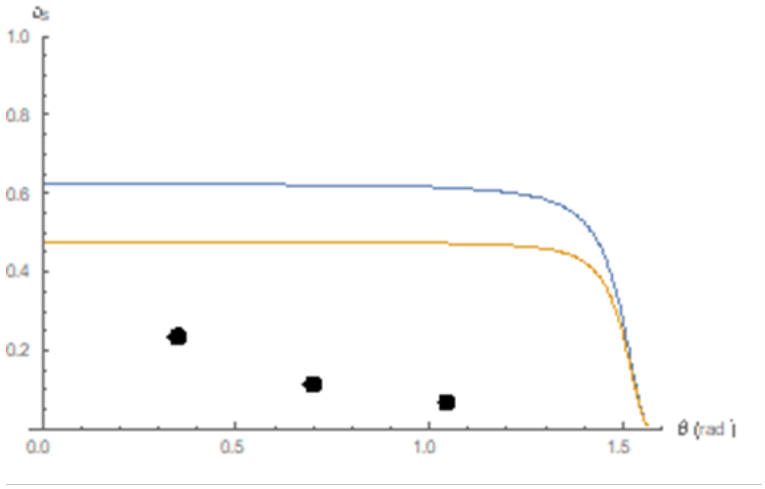

Figure 83: Sandford-Robertson curve-fit for Aluminum membrane mirror sample

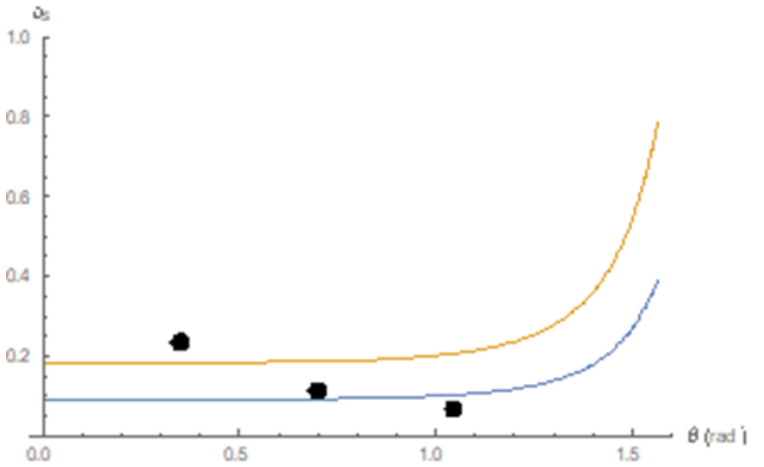

Figure 84: Wellems curve-fit for Aluminum membrane mirror sample

Bibliography

1. Office of Technology Assessment U.S. Congress. Ballistic missile defense technologies, ota-isc-254. September 1985. Library of Congress Catalog Card Number 85-600586.

2. J E Canady and J L Allen. Illumination from space with orbiting solar-reflector spacecraft. 1982.

3. Danny Lewis. How a russian space mirror briefly lit up the night. *Smithsonian Magazine*, January 21, 2016.

4. Eugene Hecht. *Optics*. Pearson, New York City, NY, 5 edition, 2015.

5. Alan Taylor. Welcome home atlantis, July 21, 2011.

6. M. A. Marciniak. Bidirectional reflectance distribution function (brdf), infrared technology. Technical report, Air Force Institute of Technology, 2022.

7. S. E. Nauyoks, S. Freda, and M. A. Marciniak. Dynamic data driven bidirectional reflectance distribution function measurement system. *Reflection, Scattering, and Diffraction from Surfaces IV*, 9205, 2014.

8. Nathan R. Boone. Cislunar debris propagation following a catastrophic spacecraft mishap. Master's thesis, Air Force Institute of Technology, 2021.

9. Christian Oord. Sun gun: Nazis worked on a weapon to destroy their enemies with the power of the sun. *War History Online*, January 28, 2019.

10. Hermann Oberth. *Ways to Spaceflight*. NASA, Munich-Berlin, 1972. Translation of 'Wege zur Raumschiffahrt', R. Oldenbourg Verlag, Munich-Berlin, 1929.

11. Arthur G. Buckingham and Harold M. Watson. Basic concepts of orbiting reflectors. 1968.

12. Kenneth W. Billman, William P. Gilbreath, and Stuart W. Bowen. Orbiting mirrors for terrestrial energy supply. 1978.

13. Krafft A. Ehricke. Space light: Space industrial enhancement of the solar option. 1979.

14. Vladimir Syromyatnikov. Space regatta consortium.

15. Warren E. Leary. Russians to test space mirror as giant night light for earth. *New York Times*, pages 41, 47, January 12, 1993.

16. Daniel W. E. Green. Iauc 7104: Space-mirror experiment; rx j0812.4-3114; p/1998 u3. *Central Bureau for Astronomical Telegrams*, Circular No. 7104, February 3, 1999.

17. Carl Koppeschaar. Russian are going to kill the night, February 1, 1999.

18. Lewis M. Fraas, Geoffrey A. Landis, and Arthur Palisoc. Mirror satellites in polar orbit beaming sunlight to terrestrial solar fields at dawn and dusk. 2013.

19. Onur Celik and Colin R. McInnes. An analytical model for solar energy reflected from space with selected applications. 2022.

20. B. J. de Blonk, J. D. Moore, B. G. Patrick, and E. M. Flint. Membrane mirrors in space telescopes. In *Recent Advances in Gossamer Spacecraft*. AIAA, Reston, VA, 2006.

21. J Yellowhair. *Field Guide to Solar Optics*. SPIE, Bellingham, Washington, 1 edition, 2020.

22. Noam Lior. Mirrors in the sky: Status, sustainability, and some supporting materials experiments. *Renewable and Sustainable Energy Reviews*, 18, 2013.

23. Daniel M Dombrowski. Investigation of mirror satellite concept to augment natural lighting conditions on orbit. Master's thesis, Air Force Institute of Technology, 2021.

24. Victor Szebehely. *Theory of Orbits*. Academic Press, New York/London, 1967.

25. Hanspeter Schaub and John L. Junkins. *Analytical Mechanics of Space Systems*. AIAA Education Series. AIAA, New York, 4 edition, 2018.

26. Daniel J. Grebow. Generating periodic orbits in the circular restricted three-body problem with applications to lunar south pole coverage. Master's thesis, Purdue University, 2006.

27. Wayne R. Schlei. An application of visual analytics to spacecraft trajectory design. Master's thesis, Purdue University, 2011.

28. V. V. Markellos and A. A. Halioulias. Numerical Determination of Asymmetric Periodic Solutions. , 46(1):183–193, January 1977.

29. Jacob A. Dahlke. Pseudo-arclength continuation/families of orbits and evolving poincare maps. Technical report, Air Force Institute of Technology, 2022.

30. European Space Agency. Types of orbits, March 30, 2020.

31. Jacob A. Dahlke. Optimal trajectory generation in a dynamic multi-body environment using a pseudospectral method. Master's thesis, Air Force Institute of Technology, 2018.

32. Terry Alfriend, Srinivas Vadali, Pini Gurfil, Jonathan How, and Louis Breger. *Spacecraft Formation Flying*. Elsevier, Kidlington, Oxford, UK and Burlington, MA, USA, 1 edition, 2010.

33. David Vallado. Fundamentals of astrodynamics and applications - astrodynamics software, Retrieved August 29, 2022.

34. Thomas A. Pavlak. Mission design applications in the earth-moon system: Transfer trajectories and stationkeeping. Master's thesis, Purdue University, 2010.

35. Bong Wie. *Space Vehicle Dynamics and Control*. AIAA Education Series. AIAA, New York, 2 edition, 2008.

36. Jia Luo and C. Edward Lan. Determination of weighting matrices of a linear quadratic regulator. *Journal of Guidance and Control*, 18(6):1462–1463, 1995.

37. James R. Wertz and Wiley J. Larson. *Space Mission Analysis and Design*. Microcosm Press, El Segundo, CA, 3 edition, 1999.

38. Jean-Jacques E. Slotine and Weiping Li. *Applied Nonlinear Control*. Prentice-Hall, New York, 1 edition, 1991.

39. W E Krag. Visible magnitude of typical satellites in synchronous orbits. 1974.

40. James R. Shell. Optimizing orbital debris monitoring with optical telescopes. 2010.

41. Jacob K. Vendl and Marcus J. Holzinger. Cislunar periodic orbit analysis for persistent space object detection capability. 2021.

42. Michael R. Thompson, Nathan P. Re, Cameron Meek, and Bradley Cheetham. Cislunar orbit determination and tracking via simulated space-based measurements. 2021.

43. Adam P. Wilmer, Robert A. Bettinger, and Bryan D. Little. Preliminary viability assessment of cislunar periodic orbits for space domain awareness. 2021.

44. Adam P. Wilmer, Robert A. Bettinger, and Bryan D. Little. Cislunar periodic orbit constellation assessment for space domain awareness of l1 and l2 halo orbits. 2021.

45. Vincent L. Pisacane. *The Space Environment and its Effects on Space Systems*. AIAA, Reston, VA, 1 edition, 2008.

46. Clayton C. Hankins. The effect of shot dependency on composite materials subject to ballistic testing. Master's thesis, Air Force Institute of Technology, 2021.

47. Michaela N. Villarreal, Jonathan W. Arenberg, and Lauren Halvonik Harris. A predictive model for micrometeoroid damage to gossamer structures, 2022.

48. F. E. Nicodemus, J. C. Richmond, J. J. Hsia, I. W. Ginsberg, and T. Limperis. Geometrical considerations and nomenclature for reflectance. Technical report, Institute for Basic Standards, National Bureau of Standards, Washington, D.C.

49. M. W. Bishop, S. D. Butler, and M. A. Marciniak. Robust method of determining microfacet brdf parameters in the presence of noise via recursive optimization. *Optical Engineering*, 60, September 2021.